

Costa Rica Institute of Technology
Mechatronics Engineering Academic Area



**DESIGN OF THE DIAMAGNETIC LOOP, MIRNOV COILS
AND ROGOWSKI COIL FOR THE MEDUSA-CR
SPHERICAL TOKAMAK**

Graduation Project Report to Opt for

the Title of Mechatronics Engineer

Author: Juan Ignacio Monge Colepicolo

I hereby declare that the present Graduation Project has been carried out entirely by my person, using and applying literature referring to the subject and introducing my own knowledge.

Cases in which I used bibliography, I proceeded to indicate the sources by the respective bibliographic citations. Consequently, I assume full responsibility for the work presented here and for all the content of the corresponding final report.

Juan Ignacio Monge Colepico

Cartago, February 15, 2019

Céd: 1-1552-0101

Instituto Tecnológico de Costa Rica
Área Académica de Ingeniería en Mecatrónica
Proyecto de Graduación
Tribunal Evaluador

Proyecto de Graduación defendido ante el presente Tribunal Evaluador como requisito para optar por el título de Ingeniero en Mecatrónica con el grado académico de Licenciatura, del Instituto Tecnológico de Costa Rica.

Miembros del Tribunal

Ing. Arnoldo Ramírez Jiménez
Profesor Lector

MSc. Ignacio del Valle Granados
Profesor Lector

MSc. Jaime Mora Meléndez
Profesor Asesor

Los miembros de este Tribunal dan fe de que el presente trabajo de graduación ha sido aprobado y cumple con las normas establecidas por el Área Académica de Ingeniería en Mecatrónica.

14 de febrero, 2019

Instituto Tecnológico de Costa Rica
Área Académica de Ingeniería en Mecatrónica
Proyecto de Graduación
Tribunal Evaluador
Acta de Evaluación

Proyecto de Graduación defendido ante el presente Tribunal Evaluador como requisito para optar por el título de Ingeniero en Mecatrónica con el grado académico de Licenciatura, del Instituto Tecnológico de Costa Rica.

Estudiante: Juan Ignacio Monge Colepicolo

Nombre del Proyecto: *DESIGN OF THE DIAMAGNETIC LOOP, MIRNOV COILS
AND ROGOWSKI COIL FOR THE MEDUSA-CR SPHERICAL TOKAMAK*

Miembros del Tribunal

Ing. Arnoldo Ramírez Jiménez
Profesor Lector

MSc. Ignacio del Valle Granados
Profesor Lector

MSc. Jaime Mora Meléndez
Profesor Asesor

Los miembros de este Tribunal dan fe de que el presente trabajo de graduación ha sido aprobado y cumple con las normas establecidas por el Área Académica de Ingeniería en Mecatrónica.

Nota final del Proyecto de Graduación: _____

14 de febrero, 2019

Resumen

El tokamak esférico MEDUSA-CR ($I_p = 20 \text{ kA} - 40 \text{ kA}$, $B_T = 0.5 \text{ T}$, $R = 0.14 \text{ m}$) está bajo reconstrucción en el Laboratorio de Plasma de Costa Rica para Energía y Aplicaciones de Fusión. Una cámara de vacío externa y un sistema de bombeo de gas se elaboraron previamente para esta máquina. Ahora, un nuevo conjunto de diagnósticos magnéticos es diseñado para implementarse en MEDUSA-CR con el propósito de adquirir información relacionada a la posición, la corriente y el campo magnético toroidal del plasma.

Los diagnósticos magnéticos previos instalados en MEDUSA-CR incluían un conjunto de 12 bobinas Mirnov y una bobina Rogowski, pero no se construyó ningún diamagnetic loop. Este proyecto se centra en el diseño de mecatrónica del nuevo conjunto de bobinas Mirnov, bobina Rogowski y diamagnetic loop para MEDUSA-CR. Una estructura mecánica completa, basada en las restricciones mecánicas de este tokamak, se desarrolla para los diagnósticos utilizando acero inoxidable 316L, grafito y nitruro de boro. Por otro lado, el sistema electrónico se diseña y el protocolo del sistema de adquisición de datos se elige en función de las propiedades del plasma a medir. Todos los sistemas están diseñados para operar en las condiciones requeridas por el reactor y el laboratorio.

Además, se construyó, calibró e instaló un juego de bobinas de Mirnov en el GOLEM tokamak en la República Checa. En este proyecto se describe de manera completa de los procesos de construcción y calibración, así como los resultados de la implementación. La información obtenida por las bobinas Mirnov construidas del GOLEM tokamak se integra electrónicamente y analiza numéricamente para establecer el primer paso hacia futuros procesos de medición en MEDUSA-CR.

Palabras clave: MEDUSA-CR, esférico, tokamak, bobinas de Mirnov, bobina de Rogowski, diamagnetic loop, mecatrónico, sistema de adquisición de datos.

Abstract

MEDUSA-CR spherical tokamak ($I_p = 20 \text{ kA} - 40 \text{ kA}$, $B_T = 0.5 \text{ T}$, $R = 0.14 \text{ m}$) is under recommission at the Costa Rica Plasma Laboratory for Fusion Energy and Applications. An external vacuum vessel and a gas pumping system were elaborated previously for this machine. Now, a new set of magnetic diagnostics is designed to be implemented in MEDUSA-CR with the purpose of acquiring information related to the position, the current and the toroidal magnetic field of plasma.

Previous magnetic diagnostics installed in MEDUSA-CR included a set of 12 Mirnov coils and a Rogowski coil, but not a diamagnetic loop system. This project is focused on the mechatronics design of the new set of Mirnov coils, Rogowski coil and diamagnetic loop for MEDUSA-CR. A complete mechanical structure, based on this tokamak mechanical constraints, is developed for the diagnostics using 316L stainless steel, graphite and boron-nitride. On the other hand, the electronic system is designed and the data acquisition system protocol is chosen based on the measuring plasma properties. All systems are opted to operate under conditions required by the reactor and the laboratory.

Furthermore, a Mirnov set was constructed, calibrated and installed at GOLEM tokamak in Czech Republic. A complete description of the construction and calibration processes, as well as the implementation results, are described in this project. Information obtained by the constructed Mirnov coils from GOLEM tokamak is numerically integrated and analyzed to set a cornerstone for future measurements in MEDUSA-CR program.

Keywords: MEDUSA-CR, spherical, tokamak, Mirnov coils, Rogowski coil, diamagnetic loop, mechatronics, data acquisition system.

To my family

Acknowledgements

I would like to express my gratitude to my advisor, Ing. Jaime Mora Meléndez, MSc. for his guidance, patience and communication during this process. Furthermore, I am thankful to Dr. Ivan Vargas Blanco, Phd. for facilitating the collaboration with the international research team at the Czech Technical University to develop this project. My thanks also go to Ing. Vojtech Svoboda, Csc., Pravesh Dhyani, Phd., Tomas Markovic, MSc. and André Torres, MSc. for guidance, supervision and friendship during my time in Prague. My infinite gratitude goes to my family, specially to my father, for giving me courage and motivation throughout my entire journey at university.

Juan Ignacio Monge Colepicolo

Cartago, February 15, 2019

Contents

List of Figures	iii
Table Index	vi
Symbols and Abbreviations	vii
1 INTRODUCTION	1
1.1 Project Environment	1
1.2 Problem Definition	4
1.2.1 Generalities	4
1.2.2 Problem Synthesis	5
1.3 Objectives	5
1.3.1 General Objective	5
1.3.2 Specific Objectives	5
2 Theoretical Framework	7
2.1 Fusion Energy	7
2.1.1 Criteria for Plasmas	7
2.1.2 Controlled Fusion	8
2.1.3 Magnetic Confinement	10
2.2 Magnetic Diagnostics	16
2.2.1 Principles of Inductive Sensors	16
2.2.2 Diamagnetic Loops	19
2.2.3 Rogowski Coils	20
2.2.4 Mirnov Coils	22
2.2.5 Hall Probes	24
2.3 General Parameters of MEDUSA-CR Spherical Tokamak	25
3 The Magnetic Diagnostics	28
3.1 Mirnov Coils System	28
3.1.1 Mechanical Design	28
3.1.2 Electronic Design	33
3.2 Diamagnetic Loop System	36
3.2.1 Mechanical Design	36
3.2.2 Electronic Design	38

3.3	Rogowski Coil System	40
3.3.1	Mechanical Design	40
3.3.2	Electronic Design	43
3.4	Diagnostics Fixing Structure	45
3.5	Signal Conditioning	49
3.5.1	Coils Construction	49
3.5.2	Coils Calibration	58
3.5.3	Signal Integration	63
3.6	Data Acquisition System	68
4	Results and Analysis	70
4.1	Mechanical Design	70
4.2	Coils Construction	74
4.3	Calibration	75
4.4	Integration	77
5	Conclusions and Recommendations	79
5.1	Conclusions	79
5.2	Recommendations	80
	Bibliography	81
A	Matlab Programs	83
A.1	Mirnov Coils Parameter Calculation	83
A.2	Diamagnetic Loop Parameter Calculation	84
A.3	Rogowski Coil Parameter Calculation	85
A.4	Mirnov Coils Calibration	87
A.5	Mirnov Coil No.11 Signal Integration	89
A.6	Mechanical Blueprints of the Magnetic Diagnostics	91

List of Figures

1.1	Proposed designs for the MEDUSA-CR tokamak vacuum vessel. [11, 12]	2
1.2	GOLEM and COMPASS tokamaks located in Czech Republic. [3, 4]	3
2.1	Power generation from a tokamak. [13]	9
2.2	Toroidal magnetic field on a tokamak. [13]	10
2.3	Poloidal magnetic field on a tokamak. [13]	11
2.4	Basic principles of a working tokamak. [14]	11
2.5	Flux surfaces plot of the MEDUSA-CR. [19]	14
2.6	Plasma elongation of $\kappa = 2$ generated with a spherical tokamak of ratio $A = 1.5$. [23]	15
2.7	Inductive sensor with ferromagnetic core (D is coil diameter, D_i is core diameter, l is coil length and l_c is core length). [30]	17
2.8	Principle of a working magnetic coil and its integrating circuit, where V is equivalent to U_{sig} and V_0 is equivalent to U_{out} . [20]	20
2.9	Principle of a working Rogowski coil. [20]	21
2.10	Integral geometry for integration in equation 2.41 in a Rogowski coil. [20]	21
2.11	Plasma position measurements using Mirnov coils. [20]	23
2.12	Schematic illustration of a Hall probe operating principle. [24]	24
2.13	Top view diagram of MEDUSA-CR vacuum vessel in millimeters.	26
2.14	Side view diagram of MEDUSA-CR vacuum vessel in millimeters.	27
3.1	MEDUSA-CR toroidal and central coils assembly.	28
3.2	MEDUSA-CR toroidal field coil dimensions diagram in millimeters.	29
3.3	Mirnov coils structural assembly for the MEDUSA-CR tokamak.	29
3.4	D-shape Mirnov coils support dimensions diagram in millimeters.	30
3.5	Views of the Mirnov coil and graphite shield assembly in millimeters.	31
3.6	Mirnov coils position diagram in millimeters.	31
3.7	Cylindrical fixation for the Mirnov coils D-shape support system.	32
3.8	Dimensions diagram for the designed boron-nitride Mirnov coils.	34
3.9	Parts diagram of the diamagnetic loop support system.	36
3.10	Dimensions diagram for the diamagnetic loop main support in millimeters.	37
3.11	Dimensions diagram for the diamagnetic loop L-shaped bracket in millimeters.	37
3.12	Dimensions diagram for the cylindrical fixation in millimeters.	38

3.13	Parts diagram of the Rogowski coil support system.	41
3.14	Dimensions diagram in millimeters for the main support ring of the Rogowski coils system.	42
3.15	Dimensions diagram in millimeters for the L-shaped holder of the Rogowski coils system.	42
3.16	Dimensions diagram in millimeters for the pressing brackets of the Rogowski coils system.	43
3.17	Fixing Structure diagram from the Mirnov coils system.	45
3.18	Central bar diagram in millimeters of the Fixing Structure.	46
3.19	L-shaped bearings diagram in millimeters of the Fixing Structure.	47
3.20	Pressing holders diagram in millimeters of the Fixing Structure.	47
3.21	Coils system mounted on the toroidal field coils from MEDUSA-CR.	48
3.22	Magnetic diagnostics position without the MEDUSA-CR toroidal field coils.	48
3.23	Dimensions diagram in millimeters for the set of 16 Mirnov coils installed in GOLEM tokamak [22].	49
3.24	Position diagram for the set of 16 Mirnov coils installed in GOLEM tokamak [22].	51
3.25	Side view of the manual drill used in the winding process of the Mirnov coils.	51
3.26	Front view of the manual drill used in the winding process of the Mirnov coils.	52
3.27	Mechanical support for coils fixation.	52
3.28	Coil and drill system for winding process.	53
3.29	Constructed coil with twisted end.	53
3.30	Set of 16 Mirnov coils constructed at IPP.	54
3.31	Set of 16 Mirnov coils installed in the assembly ring.	54
3.32	Coils welding with the assembly feedthrough.	55
3.33	Complete assembly with 16 Mirnov coils installed.	55
3.34	Winding drill with turns counter used for the Rogowski coil construction.	56
3.35	Free-rotation bearing fixed at the second end of the thicker cable.	56
3.36	Half wound Rogowski coil using a $d = 0.25$ mm copper wire.	57
3.37	Rogowski coil with electric tape wrapping.	57
3.38	Welded ends of the Rogowski coil.	58
3.39	Calibration coil connected to a LC circuit.	59
3.40	Magnetic field simulation of the calibration coil [29].	59
3.41	Connection diagram of the calibration coil with the LC circuit [29].	59
3.42	Mirnov coil position inside the calibration coil.	60
3.43	Oscilloscope input signals for 11000 nF nominal capacitance.	61
3.44	Amplified signals obtained form oscilloscope data.	62
3.45	Amplified signals with phase correction.	62
3.46	Linear relationship between the Mirnov coil signal U_{sig} and calibration coil current.	63
3.47	Passive integration circuit [10].	63
3.48	Active integration circuit [10].	64

3.49	Physical integration circuit installed in GOLEM for 6 temperature probes.	64
3.50	Plasma shot No. 29293 in GOLEM tokamak [2].	65
3.51	Raw data from Mirnov coil No. 11, Type B.	66
3.52	Integrated data from Mirnov coil No. 11, Type B.	66
3.53	Data Acquisition diagram for MEDUSA-CR.	68
4.1	Mechanical displacement simulation for the lower pressing holder of the Fixing Structure, in 316L stainless steel.	71
4.2	Mechanical displacement simulation for the upper pressing holder of the Fixing Structure, in 316L stainless steel.	71
4.3	Mechanical displacement simulation for the L-shaped bearings of the Fixing Structure, in 316L stainless steel.	72
4.4	Mechanical displacement simulation for the central bar of the Fixing Structure, in 316L stainless steel.	72
4.5	U_{sig} vs. Current graph from the calibration of coil No. 1 with 11000 nF. .	75
4.6	U_{sig} vs. Current graph from the calibration of coil No. 5 with 11000 nF. .	76
4.7	U_{sig} vs. Current graph from the calibration of coil No. 13 with 11000 nF. .	76
4.8	U_{sig} vs. Current graph from the calibration of coil No. 15 with 11000 nF. .	77
4.9	Signal integration comparison for coil 15 during shot No. 29293.	78

Table Index

2.1	Capacitive energy available in MEDUSA-CR bank of capacitors. [19]	25
2.2	Design and operation parameters for MEDUSA-CR spherical tokamak. [19]	26
3.1	Coils design parameters.	33
3.2	Parameters of chosen copper wire with $d = 0.1$ mm. [6].	34
3.3	Expected results for the Mirnov coils parameters. See section A.1.	35
3.4	Diamagnetic loop coil design parameters.	39
3.5	Parameters of chosen copper wire with $d = 0.25$ mm. [6].	39
3.6	Expected parameters for the diamagnetic loop coil. See section A.2.	39
3.7	Expected parameters for the diamagnetic loop coil with a $d = 0.1$ mm wire.	40
3.8	Parameters of the chosen 16-AWG Kapton TM insulated wire [25].	44
3.9	Rogowski core design parameters.	44
3.10	Expected results for the Rogowski coil parameters. See section A.3.	45
3.11	Type B coils parameters.	50
3.12	Coils type arrangement.	50
3.13	Calibration coil parameters.	58
3.14	Frequency configuration with different capacitance values.	60
4.1	Material properties for 316L stainless steel, used in the Fixing Structure [26].	70
4.2	Total mass of the magnetic diagnostics, excluding the Diagnostics Fixing Structure.	70
4.3	Input mesh parameters for stress analysis.	71
4.4	Results for the finite elements analysis of the Fixing Structure.	73
4.5	Convergence results for the finite elements analysis of the Fixing Structure.	73
4.6	Expected results for the Mirnov coils Type B parameters.	74
4.7	Measured parameters for Mirnov coils after construction.	74
4.8	Measured parameters for Rogowski coil after construction.	75
4.9	Linear relationships from coils Type A calibration.	77

Symbols and Abbreviations

Abbreviations

°	degree (angles)
°C	degree Celsius (temperature)
μH	microhenry (inductance)
μs	microsecond (time)
Ω	Ohm (resistance)
A	Ampere (current)
AWG	American Wire Gauge (wire diameter reference)
cm	centimeter (distance)
cm ²	square centimeter (area)
eV	electronvolt (energy)
F	Farad (capacitance)
H	Henry (inductance)
Hz	Hertz (frequency)
in.	inch (distance)
K	Kelvin (temperature)
kA	kiloampere (current)
keV	kiloelectronvolt (energy)
kHz	kilohertz (frequency)
m	meter (distance)
m ²	square meter (area)
m ³	cubic meter (volume)
mF	millifarad (capacitance)
mH	millihenry (inductance)
MHz	megahertz (frequency)
mm	millimeter (distance)
MPa	megapascal (pressure)
ms	millisecond (time)
mT	millitesla (magnetic field)
Pa	Pascal (pressure)
s	second (time)
T	Tesla (magnetic field)
Torr	Torr (pressure)
V	Volt (voltage)

Chapter 1

INTRODUCTION

1.1 Project Environment

Costa Rica Plasma Laboratory for Fusion Energy and Applications was founded by Dr. Ivan Vargas Blanco and established at the Costa Rica Institute of Technology (ITCR) main campus in Cartago. This milestone was possible through an agreement with the Center for Energy, Environmental and Technological Research of Spain (CIEMAT).

After its foundation, the laboratory opened path to a national legislation created to promote research in plasma physics. The Institutional Council of the ITCR on its ordinary session No. 2647, Article 16, carried on February 4, 2010, declares the research in plasma physics as a matter of public and institutional interest. Additionally, the National Ministry of Science and Technology of Costa Rica published in La Gaceta, Edition No. 93, decree No. 36569 states that “public and private entities are urged to contribute, to the extent of their possibilities and within the current legal regulations, with contribution of economic, logistical and technical resources for conducting research in this area”.

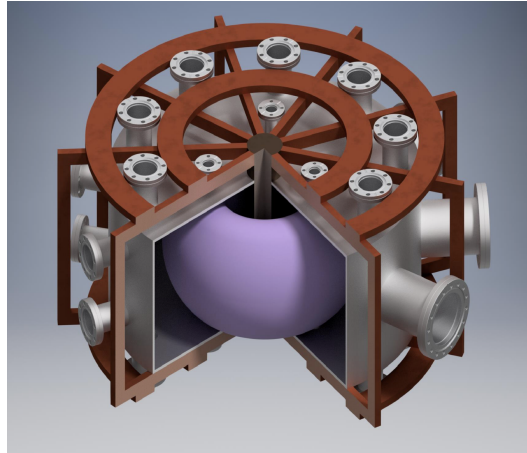
The laboratory currently has research programs in industrial plasmas and nuclear fusion. In this last area, Costa Rica is positioned as a pioneer in Latin America by having two types of fusion reactors for plasma confinement: the MEDUSA-CR Spherical Tokamak and the SCR-1 Stellarator.

Based on the *Used Equipment Sales Agreement* [21], MEDUSA-CR spherical tokamak, named after **Madison EDUcation Small Aspect** ratio tokamak, was purchased in 2013 from the University of Wisconsin-Madison for a total cost of one US dollar. Since then, a research group conformed by engineers and physicists has been working in recommissioning MEDUSA-CR back into operation.

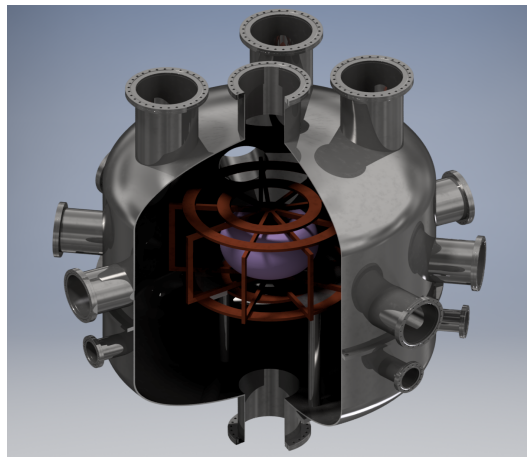
Design and operating parameters for the Medusa-CR are described as follows: plasma major radius $R < 0.14$ m, plasma minor radius $a < 0.10$ m, toroidal field at the geometric center of the vessel $B_T < 0.5$ T, plasma current $I_p < 40$ kA, central electron temperature $T_e(0) < 140$ eV, discharge duration $t_p < 3$ ms, and OH flux swing of 10 mV-s (single

swing) [19].

During the next years, three main topics were addressed in the first recommission stage of MEDUSA-CR: The electric current regulator of the coils, the injection system and the vacuum system [11]. In 2017, two new designs were proposed in substitution of MEDUSA-CR original glass vacuum vessel: (1) A LS 304 stainless steel vacuum vessel surrounded by the magnetic coils and (2) A LS 304 stainless steel vacuum vessel surrounding the magnetic coils [12]. The external vacuum vessel design was later chosen in order to avoid non-desired stray fields. See figure 1.1.



(a) Internal vacuum vessel design.



(b) External vacuum vessel design.

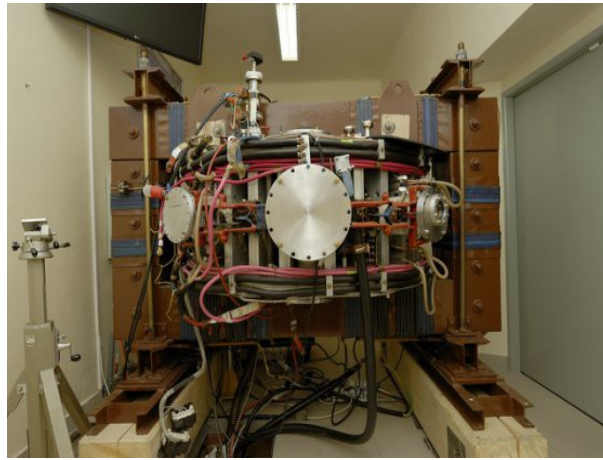
Figure 1.1: Proposed designs for the MEDUSA-CR tokamak vacuum vessel. [11, 12]

As interest for internal confinement fusion has grown, worldwide collaboration is necessary to overcome problems of reactor design and fusion technology. This project is developed in cooperation with GOLEM and COMPASS tokamaks fig. 1.2, both located in the city of Prague, Czech Republic.

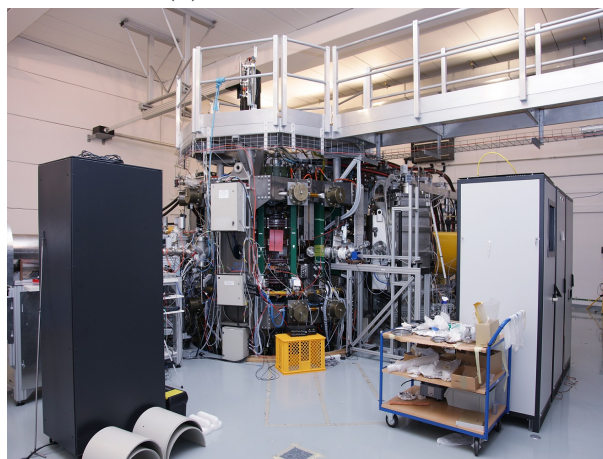
GOLEM tokamak has a minor radius of 0.1 m and a mayor radius of 0.6 m. This device, being one of the oldest operating tokamaks, was developed in early 1960's and operated

under the name of TM-1-MH until it was transferred to the Institute of Plasma Physics of the Czech Academy of Sciences (IPP CAS) in Prague in 1976. There it functioned under the name of CASTOR until 2007 when it was donated to the Czech Technical University and renamed as GOLEM. At the present, its main designation is educational purposes under the Fusenet Association [22].

On the other hand, COMPASS tokamak, having a major radius 0.6 m and height of the vessel of 0.7 m, is considered a small-sized tokamak capable of producing high plasma confinement. It was designed and operated in the 1990's at the UKAEA Culham in Great Britain and transferred in 2002 due to start of MAST tokamak operations. In present, besides COMPASS, there are only two operational tokamaks in Europe with ITER-like configuration capable of producing a regime with the High plasma confinement: The Joint European Torus (JET), presently the biggest experimental device of its type, and the ASDEX-U [4].



(a) GOLEM Tokamak.



(b) COMPASS Tokamak.

Figure 1.2: GOLEM and COMPASS tokamaks located in Czech Republic. [3, 4]

1.2 Problem Definition

1.2.1 Generalities

Costa Rica Plasma Laboratory for Fusion Energy and Applications is currently recommissioning its MEDUSA-CR Spherical Tokamak. Although an external vacuum vessel and a gas injection system control have been designed and implemented, there are no magnetic diagnostics operating in this confining machine.

Although more than fifty different diagnostics methods have been developed during the past few decades, a priority on MEDUSA-CR first engineering stage is to obtain plasma current density, total current, position, shape, conductivity, total energy content and information on Magnetohydrodynamics (MHD) instabilities [12]. Plasma diagnostics, designed to measure properties of plasma, involves knowledge of almost all fields of physics, from electromagnetism to nuclear physics, and up-to-date progress in engineering and technology (materials, electronics, mathematical methods of data treatment) [14].

The complete procedure of creating a diagnostic set is complicated and includes a joint cooperation between scientists and engineers to integer scientific requirements and technical capabilities. Literature [14] describes that the entire process is exhaustive and includes several stages:

1. Definition of the plasma parameters and properties to be measured;
2. Elaboration of the measurement requirements (spatial and temporal resolution, dynamic range, accuracy, etc.);
3. Selection of the most suitable diagnostic methods;
4. Allocation of diagnostic equipment inside and around the machine (so called integration);
5. Development of the diagnostics themselves — design and construction;
6. Testing and calibration of the apparatus in the laboratory or on existing machines;
7. Installation on the machine and commissioning;
8. Further development and upgrading.

This project is based on the design of the magnetic diagnostics to be implemented in the MEDUSA-CR tokamak. However, subsequent stages of the entire process listed above must be taken into consideration. As nobody knows in advance what new phenomena will be produced on this machine, planing of diagnostic construction must contemplate system upgrading to meet possible new scientific and technical challenges [14].

Without these diagnostics, mathematical analysis which depict the real behavior of plasma inside the reactor cannot be developed. The creation of these models for a spherical confinement geometry will then provide a complete mapping of plasma based on its magnetic properties and will enable a description of its current density and flux distribution.

Specifically, this project is focused on the following properties to be measured with the diamagnetic loop, Mirnov Coils and Rogowski Coil for the MEDUSA-CR:

- Poloidal magnetic flux (Diamagnetic Loop).
- Poloidal magnetic field (Mirnov Coil).
- Toroidal magnetic field (Mirnov Coil).
- Local magnetic fields parallel to the vessel (Rogowski Coil).

1.2.2 Problem Synthesis

Costa Rica Plasma Laboratory for Fusion Energy and Applications needs to completely develop the diamagnetic loop, Rogowski coil and Mirnov coils for its MEDUSA-CR Spherical Tokamak. For all the magnetic diagnostics listed above, it is necessary to design the mechanical structure and the signal conditioning circuit, and to select the data acquisition system for obtaining the expected magnetic measurement results.

1.3 Objectives

1.3.1 General Objective

Design the Mirnov coils, Rogowski coil and diamagnetic loop for the MEDUSA-CR Spherical Tokamak installed at the Costa Rica Plasma Laboratory for Fusion Energy and Applications, including the mechatronics solution, for future measurements of plasma position, MHD behaviours, plasma current and magnetic flux.

1.3.2 Specific Objectives

1. Elaborate the mechatronics system, including the mechanical elements, the electric diagrams and the software programming for the magnetic diagnostics.
2. Create a digital prototype, by generating a CAD simulation and a study of finite elements, of the mechanical system working under vacuum and high temperature conditions.
3. Select the data acquisition system specifications, based on sampling frequency, ATCA protocol and instrumentation requirements, for MEDUSA-CR tokamak.

4. Determine the construction and calibration methods for the Mirnov electronic system, by listing the used instruments, the data analysis procedure and the coils experimental parameters.

Chapter 2

Theoretical Framework

2.1 Fusion Energy

2.1.1 Criteria for Plasmas

Let plasma be defined as a *quasi-neutral* gas of charged and neutral particles which exhibits a *collective behavior* [5]. Since molecules in plasma are neutral, there is no net electromagnetic forces on it and the force of gravity is null. In this case, molecules move freely until they collide with other molecules, and these collisions describe the motion of particles. In cases in which an external macroscopic force is applied in any neutral gas, such as from loudspeakers, sound waves are transmitted to other individual atoms by collisions. However, this is not the case in a plasma, which has *charged particles*. As these particles ($N_D \gg 1$) are forced to move around, they can locally concentrate positive or negative charges, which can generate electric fields. Furthermore, motion of particles also generates currents, and hence magnetic fields. These fields affect the motion of other charged particles far away [5].

Plasma quasi-neutrality is based on its ability, and fundamental characteristic, to shield electric potentials that are applied to it. In lecture [27], author considers an artificially immersed charge in a plasma with thermodynamic equilibrium and at a constant temperature, independent of position. The equilibrium implies that plasma is changing in a minor rate compared to the particle collision rate, and that there is no significant change in temperature over distances compared to a collision path. Now, let the particle distribution function to be a heat “bath” at a specific temperature and a particle with kinetic and potential energy as follows:

$$W_r = \frac{mv^2}{2} + q\phi \quad (2.1)$$

Where q is a charge of a particle, considering $-e$ for an electron and $+Ze$ for an ion of charge Z , and thus the Boltzmann factor becomes:

$$\exp \left[-\left(\frac{mv^2}{2} + q\phi \right) / T \right] \quad (2.2)$$

The relative probability of the particle now depends entirely on position, through ϕ . If then, the distribution function is integrated over velocity, lecture [27] concludes that the spatial dependence that remains comes only from the Boltzmann factor:

$$n \propto \exp \left[-\left(\frac{q\phi}{T} \right) \right] \quad (2.3)$$

This implies that electrons are attracted to the positive charge in plasma, and therefore shield the electric field from the charge, preventing the field from penetrating into plasma. By the same reason, the ions have the opposite tendency. The distance over which the field from such a charge is shielded out is known as the Debye length. Author [5] defines the Debye length as the following:

$$\lambda_D \equiv \left(\frac{\epsilon_0 K T_e}{n e^2} \right)^{\frac{1}{2}} \quad (2.4)$$

Therefore, plasma is formally defined when this Debye length is much smaller than the plasma size, or $\lambda_D \ll L$.

A third condition must be also satisfied for an ionized gas to be called a plasma. If ω is the frequency of typical plasma oscillations, and τ is the mean time between this collision with natural atoms, then it is required that $\omega\tau > 1$ for gas to behave as a plasma rather than a natural gas [5].

Conditions that must be satisfied by a plasma are therefore:

1. $\omega\tau > 1$;
2. $\lambda_D \ll L$;
3. $N_D \gg 1$;

2.1.2 Controlled Fusion

Sun has been illuminating earth for billions of years, and it represents the brightest example of fusion. Fusion, as a form of nuclear energy, involves processes that occur at the opposite end of the spectrum of atomic masses than fission. In contrast to nuclear fission, where heavy nuclei like uranium (as U^{235}) are fragmented and release energy, fusion involves lighter elements and brings them together so that they may fuse to form heavier elements. This resulting elements have slightly less mass than the fusing elements and this mass difference results in the release of energy [14].

As an example, when a deuterium and tritium nuclei are fused, being the two heavier isotopes of hydrogen with mass numbers 2 and 3 respectively, they form a helium nucleus, a neutron and the mass difference is released as 17.6 MeV of energy. This reaction is represented as follows:



This process is possible when the nuclei are heated to very high thermonuclear temperatures, involving enough kinetic energy of the thermal particles to nuclei overcome the electrostatic repulsion and get close enough to fuse. For the case of deuterium and tritium, shown in equation 2.5, the process requires the nuclei to be heated to a temperature of the order of ~ 10 keV, or ~ 100 million $^{\circ}$ C. The resulting process is known as thermonuclear fusion [14].

Energy released by this reaction, may be trapped and used for electricity production. This energy is larger than that obtained from chemical reactions because the binding energy that holds a nucleus together is far greater than the energy that binds atoms and molecules together through electronic linkages. For example, the ionization energy of a hydrogen atom is 13.6 eV, being less than one millionth of the 17.6 MeV released in the D-T reaction mentioned above in 2.5.

Using tokamaks as power plants involves a combination of physics and engineering. In these cases, plasma is surrounded by a blanket that has three main roles: Firstly, it absorbs the energy from neutrons and transforms it into heat which is then carried away by a coolant to provide most of the reactor power output. Secondly, by absorbing neutrons, the blanket shield the magnetic fields of the coils and other outer components, and lastly, the blanket allows the necessary breeding of tritium to fuel the reactor. The heating leaving plasma is then extracted using gaseous or liquid coolant and transformed to electricity using the conventional methods. See figure 2.1.

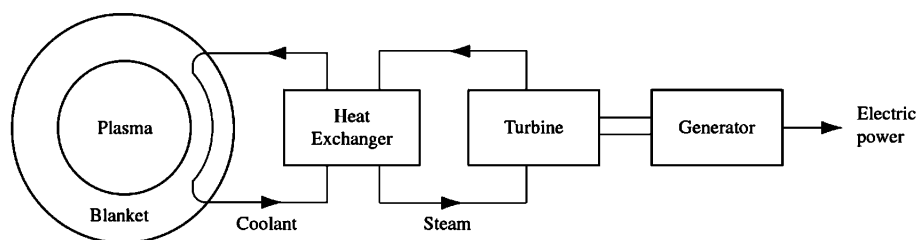


Figure 2.1: Power generation from a tokamak. [13]

Furthermore, lecture [17] cites three main advantages for developing fusion power: fuel reserves, environmental impact, and safety. However, mastering the unexpectedly difficult scientific and technological problems is still a disadvantage of fusion energy.

2.1.3 Magnetic Confinement

Achieving fusion on Earth is a technological challenge. Fusion plasma has to be created with reactants of sufficiently high temperature and density, and maintain it confined for a sufficiently long time away from any surrounding material walls. However, two main approaches for achieving this have been developed: magnetic confinement and inertial confinement. Magnetic confinement fusion is the more developed of the two approaches, and is currently the most promising path to developing future fusion reactors, especially as it can confine the plasma in a steady state for long duration [14].

On the other hand, inertial confinement fusion (ICF), works primarily by a pulse method. In these devices, thermonuclear fusion is achieved through micro-explosions of reactant targets induced by high power laser or particle beams at a high repetition rate.

Tokamaks, constitute the most successful approach of magnetic confinement. These devices utilize the electromagnetic properties of charged plasma particles to trap them away from material walls; the configuration is known a magnetic bottle.

In a tokamak, plasma is formed in the shape of a torus, through a specifically designed magnetic field configuration. Such configuration is obtained by the way in which the coils are formed. The toroidal magnetic field B_ϕ on a tokamak is formed by turning around a set of ring-like coils in the form of a torus. See figure 2.2.

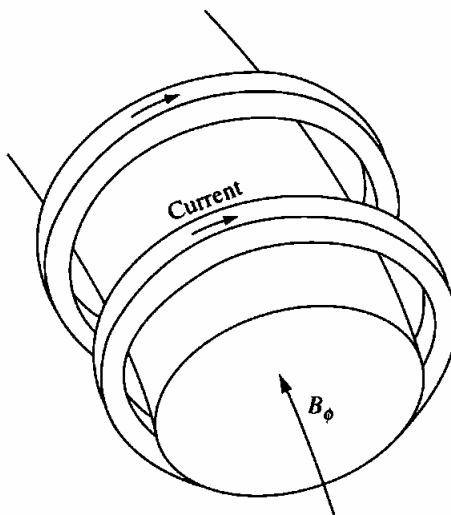


Figure 2.2: Toroidal magnetic field on a tokamak. [13]

Poloidal magnetic field B_p , on the other hand, is obtained by passing a toroidal current in plasma itself with coils turning around the cross-section of the torus. See figure 2.3.

As it is shown in figure 2.4, the combination of the toroidal field B_ϕ and the poloidal field B_p gives rise to magnetic field lines with a helical trajectory around the torus [13].

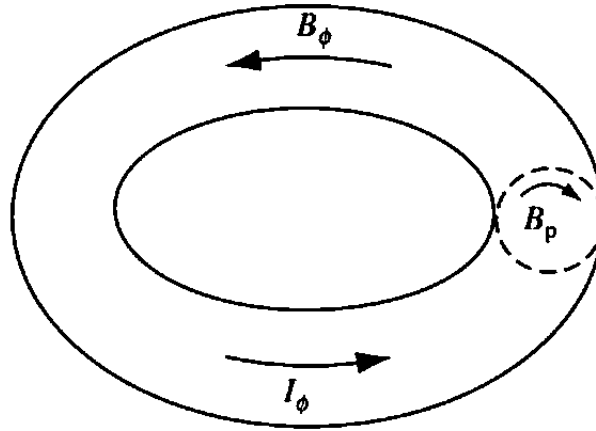


Figure 2.3: Poloidal magnetic field on a tokamak. [13]

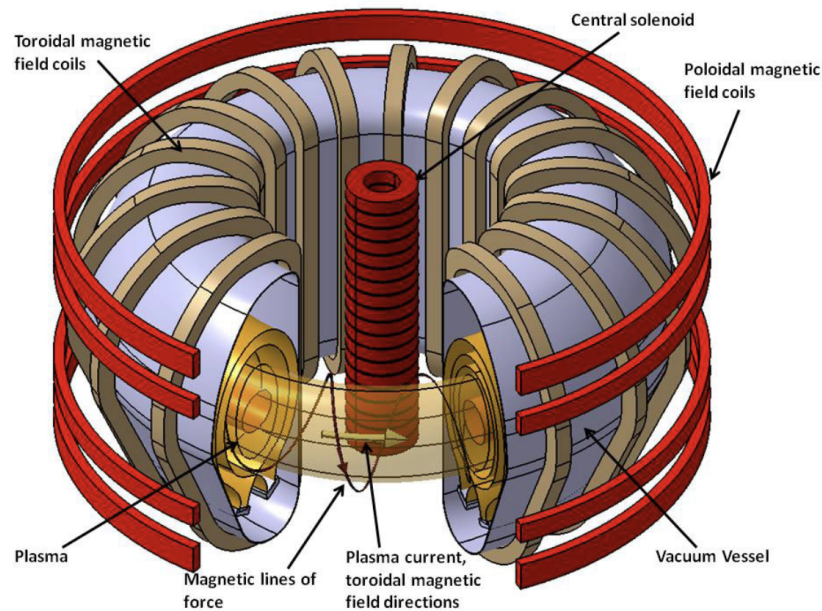


Figure 2.4: Basic principles of a working tokamak. [14]

Plasma pressure is the product of particle density and temperature.

$$p = nk_B T \quad (2.6)$$

Author [13] explains that as reactivity of plasma increases with particle density and temperature, the plasma pressure inside a tokamak must be sufficiently high. Plasma pressure is determined by stability considerations and increases with the strength of the magnetic

field. However, the magnitude of the toroidal magnetic field has a technological constraint. Copper coils, additionally, create the requirement of cooling and magnetic forces that limits the magnetic field that can be produced. So, with present technology the maximum magnetic field generated by coils is limited to around 16 T.

Spherical Tokamaks

Let magnetic pressure be defined by:

$$p_{mag} = \frac{B^2}{2\mu_0} \quad (2.7)$$

The spherical torus is based on the concept of very small aspect ratio confinement obtained by retaining only the indispensable components, such as the toroidal field coils. The development of the spherical tokamaks is motivated by accomplishing high beta β (which is the ratio between the plasma pressure 2.6 and the magnetic pressure 2.7), good confinement, stable operation in a compact configuration and cost reduction. In comparison with other confinement concepts, a spherical torus experiment is expected to be similar in compactness, low field, and high beta, but better in its empirical confinement time [23].

Spherical tokamaks (ST) behave differently than conventional tokamaks. Most of the differences are related to large toroidal field gradient across the ST plasma. Let the vacuum toroidal field of a tokamak be proportional to $\frac{1}{R}$, so the ratio between inboard magnetic field to the outboard magnetic field is then given by:

$$g(A) = \frac{B_\phi(R+a)}{B_\phi(R-a)} = \frac{A+1}{A-1} \quad (2.8)$$

Where g is the ratio of fields and A is the aspect ratio. So, let a tokamak with a ratio (A) of 5 have a g of 1.5. With the same analysis, and using 2.8, if A is reduced continuously, then g begins to increase. For example, when $A = 2$ then $g = 3$, $A = 1.5$ then $g = 5$, and so on. This large gradient of toroidal field produces new effects that are not noticeable in conventional tokamaks, for example high edge magnetic shear and a large trapped particle fraction [18].

Equations of magnetohydrodynamics (MHD) are used to describe the equilibrium state of plasma. MHD mathematical description treats plasma as a conductive fluid, so for plasma equilibrium three equations are of particular importance:

First, the divergence of the magnetic field condition:

$$\nabla \cdot \mathbf{B} = 0 \quad (2.9)$$

where \mathbf{B} is the magnetic field.

Second, the Ampere's law:

$$\nabla \times \mathbf{B} = \mu_0 \mathbf{J} + \frac{1}{c^2} \frac{\partial \mathbf{E}}{\partial t} \quad (2.10)$$

Where \mathbf{J} is the current density of plasma.

Third, conservation of plasma momentum:

$$\rho \left[\frac{\partial \mathbf{v}}{\partial t} + (\mathbf{v} \cdot \nabla) \mathbf{v} \right] = \mathbf{J} \times \mathbf{B} - \nabla p \quad (2.11)$$

Where p is plasma pressure, given in equation 2.6, \mathbf{v} is the flow velocity and ρ is the total mass density.

Eliminating time-varying terms from equations 2.9, 2.10 and 2.11 it is possible to obtain the following terms that are helpful for describing the plasma equilibrium:

$$\nabla \cdot \mathbf{B} = 0 \quad (2.12)$$

$$\nabla \times \mathbf{B} = \mu_0 \mathbf{J} \quad (2.13)$$

$$\mathbf{J} \times \mathbf{B} = \nabla p \quad (2.14)$$

Then, solving the previous equations in cylindrical-toroidal geometry (R, ϕ, Z) , where $\frac{\partial}{\partial \phi} = 0$ to guarantee the toroidal asymmetry, it results in:

$$\mathbf{B} = B_\phi \hat{e}_\phi + \mathbf{B}_p \quad (2.15)$$

$$\mathbf{B}_p = \frac{1}{2\pi R} \nabla \psi \times \hat{e}_\phi \quad (2.16)$$

As it is seen in equation 2.16 a stream function $(\psi(R, Z))$ is introduced to to make it simpler. The stream function is equivalent to the plasma poloidal flux:

$$\psi = \int \mathbf{B}_p \cdot d\mathbf{A} \quad (2.17)$$

So, the equilibrium solution is achieved after solving $\psi(R, Z)$. With some simplifications afterwards, the Grad-Shafranov equation is obtained:

$$\Delta^\circ \psi = -\mu_0 R^2 \frac{dp}{d\psi} - F \frac{dF}{d\psi} \quad (2.18)$$

Where $F(\psi) = RB_\phi$, $p(\psi)$ is plasma pressure, shown in 2.6, and $\Delta^\circ = R\frac{\partial}{\partial R}\left(\frac{1}{R}\frac{\partial}{\partial R}\right) + \frac{\partial^2}{\partial Z^2}$.

Solving the Grad-Shafranov equation 2.18 is not a simple task. However, there are different methods for solving this equation. For example, author in [15] uses the EFIT code to reconstruct the equilibrium of real plasmas, specified by 2.18. The solution obtained is the value of the flux in a defined space of interest. Results are then arranged into flux contours which are known as flux surfaces. An example of flux surfaces is shown in figure 2.5.

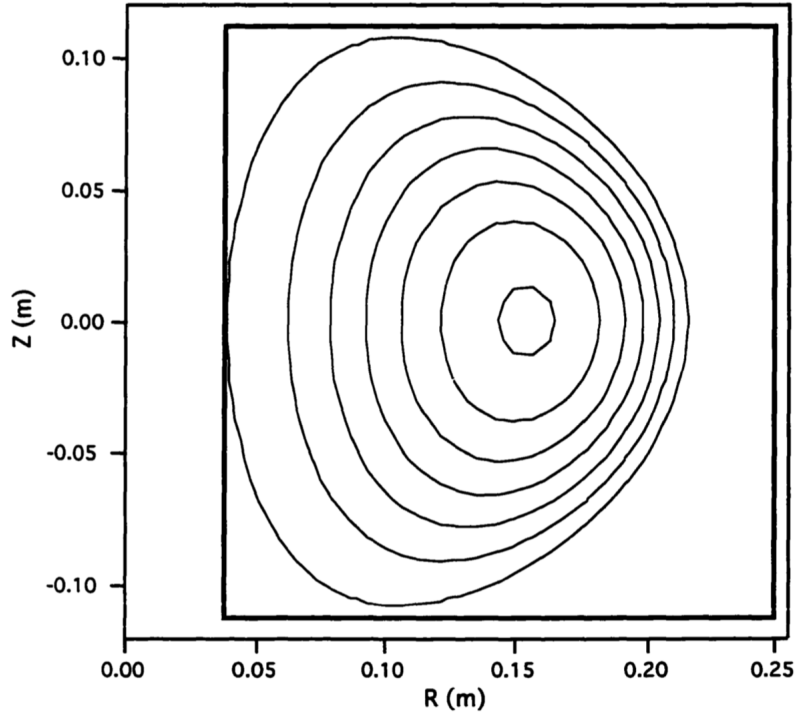


Figure 2.5: Flux surfaces plot of the MEDUSA-CR. [19]

When the magnetic contour is calculated, other quantities of interest can also be determined. Some of these quantities are the safety factor q , the plasma elongation κ , the ratio of the magnetic pressure and plasma pressure β , the magnetic shear S and the normalized internal inductance l_i . Some of the unique characteristics present in spherical tokamaks are based on the MHD equilibrium and the properties listed above.

The first important characteristic is the presence of natural elongation in spherical tokamak plasmas. MHD calculations shown in lecture [23] demonstrate that an elongation of $\kappa = 2$ is obtained naturally in a spherical tokamak with a ratio of $A = 1.5$ when a dipole vertical field is applied. In case of figure 2.6, that dipole is produced by introducing only two ring coils. Moreover, plasma natural elongation can be increased if shaping fields are additionally applied via coils located on top and above plasma. In contrast, for conventional tokamaks, with an $A > 2$ ratio, to produce a natural elongation above two, $\kappa > 2$, it is required to be applied strong current shaping coils. Drastically reducing coils

in a compact configuration leads to increased savings in the cost of the reactor magnet systems.

Plasma current and beta β are other singularities of spherical tokamaks. Plasma safety factor q is the ratio between the number of times that a particular magnetic line travels toroidally compare to the number of times that same line travels poloidally, see equation 2.19.

$$q = \frac{r\beta_\phi}{R\beta_\theta} \quad (2.19)$$

Where R is plasma major radius and r is plasma minor radius. So, a plasma that has a safety factor greater than 1, $q > 1$, is considered stable. In a spherical tokamak, the poloidal field becomes equals to and larger than the toroidal field in the outboard region, while the fields continue to be comparable in the inboard region. While introducing only a small amount of toroidal rotation, this gives highly pitched field lines at the outboard region and moderately pitched field lines at the inboard region. The net result is a strongly enhanced total toroidal rotation, and a higher q for a given plasma current. In comparison with a conventional tokamak, spherical tori permit a larger pitch to the field line for a given q , and hence a higher current.

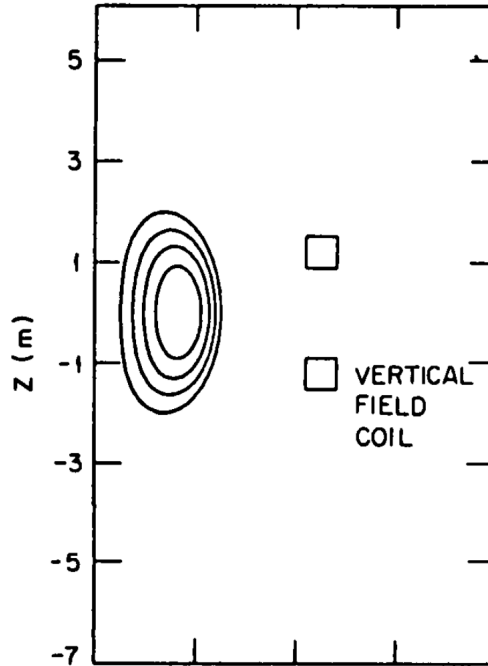


Figure 2.6: Plasma elongation of $\kappa = 2$ generated with a spherical tokamak of ratio $A = 1.5$. [23]

The presence of a strong paramagnetism is an indicator of the spherical torus characteristics. In spherical tokamaks, plasma equilibrium is force-free, that is, plasma is highly paramagnetic with the plasma current density, T , and nearly parallel to the magnetic

field. Furthermore, author [23] explains that paramagnetism contributes to increasing the plasma current for a given q by increasing the toroidal field in the plasma core and, thus, decreases with increasing plasma pressure, shown in equation 2.6.

2.2 Magnetic Diagnostics

2.2.1 Principles of Inductive Sensors

Induction coils sensors are one of the oldest and most used types of magnetic sensors. Their measurements are based on the Faraday's law of induction [30]:

$$U_{sig} = -n \cdot \frac{d\Phi}{dt} = -n \cdot A \cdot \frac{dB}{dt} = -\mu_0 \cdot n \cdot A \cdot \frac{dH}{dt} \quad (2.20)$$

Where μ_0 is the vacuum permeability constant and Φ is the magnetic flux passing through a coil with an area A and a number of turns n .

Since these sensors are easy to manufacture [22], made by wide-available materials and constructed at low cost, they are the most common type of sensors used in tokamaks to measure magnetic fields.

There are two main types of inductive sensors: Air coils and ferromagnetic core coils. However, low sensitivity of an air coil sensor and problems with its miniaturization can be overcome by the a ferromagnetic core, which acts as a flux concentrator inside the coil.

Equation 2.20 can be rewritten as follows for a coil with a ferromagnetic core:

$$U_{sig} = -\mu_0 \cdot \mu_r \cdot n \cdot A \cdot \frac{dH}{dt} \quad (2.21)$$

Where μ_r is the core relative permeability. As μ_r increases, the sensor sensitivity also increases. It is important to take into account that the core resultant permeability, μ_c can be lower than the material permeability. This is caused by demagnetizing field effect defined by the demagnetizing factor N , which is dependent to the core's geometry as follows [30]:

$$\mu_c = \frac{\mu_r}{1 + N \cdot (\mu_r - 1)} \quad (2.22)$$

In the case that the permeability μ_r is high, which is normally the case, then μ_c depends mainly in N .

The demagnetizing factor N is the calculated by the following relationship:

$$N \cong \frac{D_c^2}{l_c^2} \cdot (\ln \frac{2l_c}{D_c} - 1) \quad (2.23)$$

So, to reduce the demagnetizing factor and increase the the resultant permeability μ_c , the core needs to be long l_c and to have a small diameter D_c .

Although the use of a ferromagnetic core, see figure 2.7, enhances the sensor sensitivity, it introduces some nonlinear factors which depend on temperature, frequency, flux density, etc. This new variables alter the distribution of magnetic fields which can have undesirable consequences.

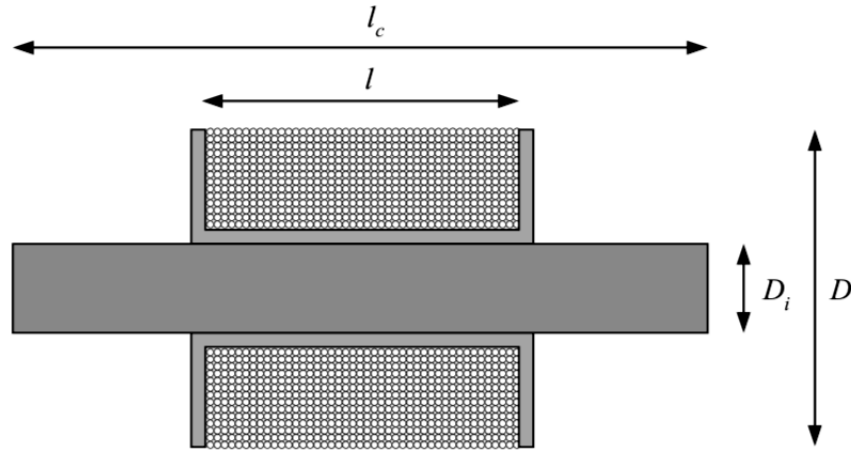


Figure 2.7: Inductive sensor with ferromagnetic core (D is coil diameter, D_i is core diameter, l is coil length and l_c is core length). [30]

Let the effective area of a multilayer coil be calculated with the following relationship:

$$A_{eff} = \frac{\pi}{4} \cdot \frac{1}{D - D_i} \cdot \int_{D_i}^D (y^2) dy \quad (2.24)$$

And based on the assumption that the diameter of the coil D is equivalent to the mean value $D_m = (D + D_i)/2$, then equation 2.24 can be simplified to the following:

$$A_{eff} = \frac{\pi}{8} \cdot (D + D_i)^2 \quad (2.25)$$

Also, if the coil is thin and $N_l d \ll D$, A_{eff} can be calculated in the following way:

$$A_{eff} = N_l \frac{\pi D^2 l}{4d} \quad (2.26)$$

Where N_l is the number of layers in the coil and d is the wire diameter.

Additionally, if it is assumed that the flux density of the magnetic field can be measured as sine wave [30] $b = B_m \cdot \sin(\omega \cdot t)$ then equation 2.20 can be rewritten as:

$$U_{sig} = 0.5 \cdot \pi^2 \cdot f \cdot n \cdot D^2 \cdot B \quad (2.27)$$

If instead of determining the flux density B , it is necessary to calculate the magnetic field strength H , then equation 2.27 can be replaced by:

$$U_{sig} = \frac{10^{-7}}{2} \cdot \pi^3 \cdot f \cdot n \cdot (D + D_i)^2 \cdot H \quad (2.28)$$

The number of turns in each coil depends on the wire diameter, d , the recommended packing factor $k \approx 0.85$ [30] and the coil dimensions:

$$n = \frac{l \cdot (D - D_i)}{2 \cdot k \cdot d^2} \quad (2.29)$$

Furthermore, to calculate the relationship between U_{sig} and the number of layers on the coil N_l , the following relationship is used:

$$U_{sig} = N_l \frac{\pi^2 D^3 K}{2d} f \dot{B}_0 \quad (2.30)$$

Where B_0 is the magnetic field and K is given by the following relationship:

$$K = \frac{l}{D} \quad (2.31)$$

It is important to take into account that various publications [31] suggest that the optimal relationship is when $K \sim 0.866$.

The sensitivity can be calculated with the following relationship:

$$S = \frac{10^{-7}}{4} \cdot \frac{\pi^3 \cdot f \cdot l}{kd^2} \cdot (D - D_i) \cdot (D + D_i)^2 \quad (2.32)$$

Let the thermal noise, VT , and coil resistance, R , be defined by the following equations:

$$VT = 2\sqrt{k_B \cdot T \cdot \Delta f \cdot R} \quad (2.33)$$

$$R = N_l \rho \frac{4Dl}{d^3} \quad (2.34)$$

Where T is temperature, N_l is the number of layers on the coil, ρ is material resistivity, Δf is frequency bandwidth and k_B is the Boltzmann factor $k_B = 1.38 \times 10^{-23} \text{ W s } K^{-1}$.

As it can be seen in equation 2.32, the sensitivity increases proportionally to D^3 , so the best way to obtain a maximal sensitivity and resolution is to increase the coil diameter D .

Additionally, author [22] cites that the following relationships are valid to calculate inductance L for thin wire coils:

$$L = N_l \mu_0 \frac{\pi D^2 l}{4d^2} \quad (2.35)$$

2.2.2 Diamagnetic Loops

Let Faraday's Law for a closed contour C and surrounded surface S be defined as:

$$\oint_C \mathbf{E} \cdot d\mathbf{l} = - \int_S \dot{\mathbf{B}} \cdot d\mathbf{s} \quad (2.36)$$

Additionally, the magnetic flux Φ is given by the following expression:

$$\Phi(t) = \int_S \mathbf{B} \cdot d\mathbf{s} \quad (2.37)$$

In an uniform magnetic field that varies with time $B(t)$, the voltage induced in the coil is given by the following relationship:

$$U_{sig} = \int_{coil} \mathbf{E} \cdot d\mathbf{l} + \int_{ends} \mathbf{E} \cdot d\mathbf{l} = - \int_S \dot{\mathbf{B}} \cdot d\mathbf{s} = n A_{eff} \dot{B} \quad (2.38)$$

Where n is the number of turns in the coil, A_{eff} is the effective area of the coil and \dot{B} is time derivative magnetic field. However, as it is of more interest calculating B rather than \dot{B} , then equation 2.38 can be transformed into equation 2.39 using an analog integrating circuit, such as one shown in figure 2.8.

$$U_{out} = \frac{n A_{eff} B}{RC} \quad (2.39)$$

Diamagnetic loops are used on tokamaks to measure the average magnetic flux Φ by detecting the poloidal magnetic flux ψ and the toroidal magnetic flux χ on an effective area S . From the point of view of equation 2.39 the effect of the wire is to transform the inductive electric field into an electrostatic field which gives rise to the voltage V across the the coil ends.

There is a major consideration related to stray fields that must be considered in the design of a diamagnetic loop. Author in [20] mentions that if a current flows in the coil, generated by the impedance of additional measurement equipment, then there may be a stray finite electric field within the coil due to equipment resistivity. So, to avoid these

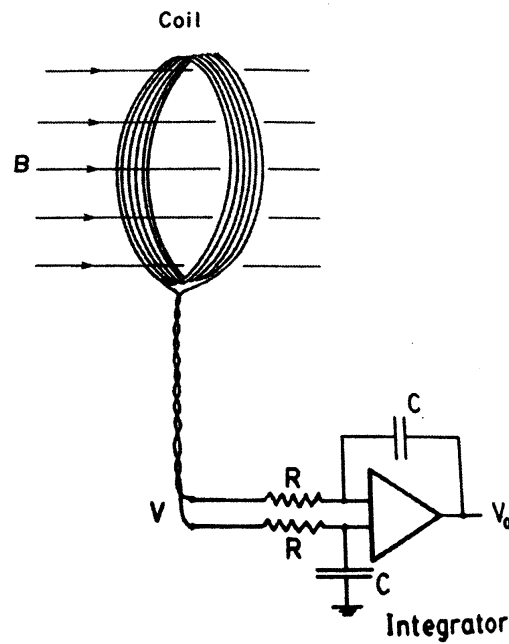


Figure 2.8: Principle of a working magnetic coil and its integrating circuit, where V is equivalent to U_{sig} and V_0 is equivalent to U_{out} . [20]

non-desirable stray field, it is recommended to include an optocoupler between the raw signal and the data acquisition system.

2.2.3 Rogowski Coils

A Rogowski coil is a solenoidal coil whose ends are brought around together to form a torus [20]. Figure 2.9 shows a cross sectional area A with constant turns per unit length n . So, the total flux that is present in each coil is presented as the following relationship:

$$\Phi = n \oint_l \int_A dAB \cdot d\mathbf{l} \quad (2.40)$$

Where $d\mathbf{l}$ is the line element parallel to the solenoidal axis. It has to be highlighted that is important to have the return wire back and down the coil, such as illustrated in figure 2.10. Otherwise, a term generated from the flux passing through the torus center has to be included in equation 2.40.

Now, changing the integration order in equation 2.40, the Ampere law is described as follow:

$$\oint_l \mathbf{B} \cdot d\mathbf{l} = \mu I \quad (2.41)$$

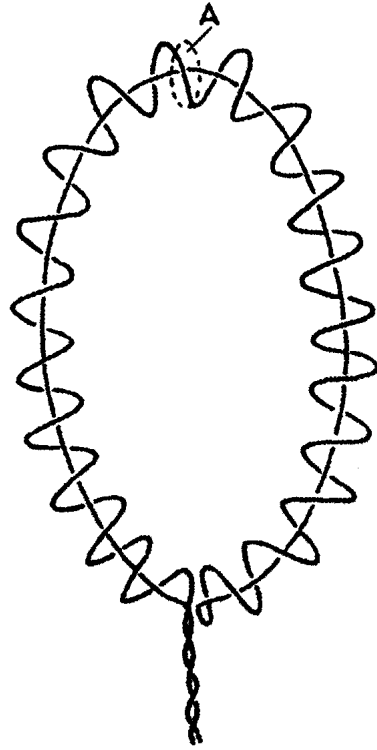


Figure 2.9: Principle of a working Rogowski coil. [20]

Where I is the total current encircled by l and the magnetic permeability of the solenoid is given by μ .

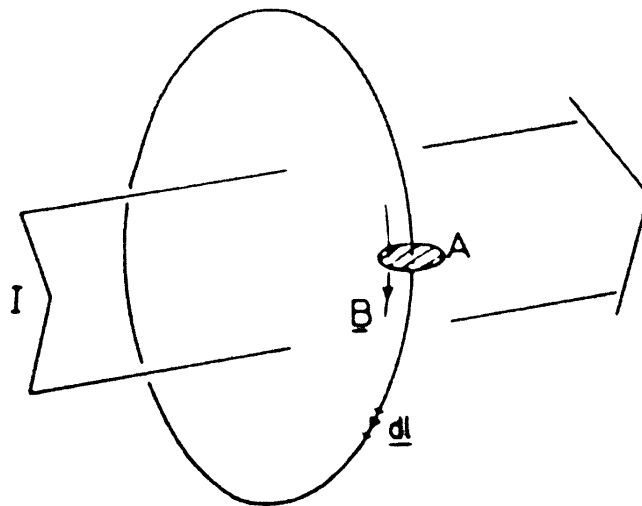


Figure 2.10: Integral geometry for integration in equation 2.41 in a Rogowski coil. [20]

Then, the magnetic flux Φ is given by:

$$\Phi = nA\mu I \quad (2.42)$$

And the voltage out of the Rogowski coil, the same as V in figure 2.8, is described by the following relationship:

$$U_{sig} = \dot{\Phi} = nA\mu\dot{I} \quad (2.43)$$

Which corresponds to electronically integrate the signal given by equation 2.42.

As it is described above, Rogowski coils provide a direct measurement of the total current flowing in plasma. It is, however, important to note that this measurement is independent of the current distribution within the loop.

2.2.4 Mirnov Coils

In geometries in which there is no coordinate, such as for a toroidally symmetric plasma, the magnetic fields can be expressed as a gradient of scalars. For example, the poloidal field of an axisymmetric toroidal plasma can be written as:

$$\mathbf{B}_p = -(\hat{\mathbf{e}}_\phi \wedge \nabla\psi)/2\pi R \quad (2.44)$$

Where $\hat{\mathbf{e}}_\phi$ is the unit vector in the toroidal direction, \mathbf{B}_p includes the radial and azimuthal parts of the field and ψ is the poloidal flux. Using 2.44 it is possible to measure the poloidal flux ψ directly using magnetic measurements. Additionally, lecture [20] deeply explains how, by integrating the voltage loop V_ϕ , it is also obtained the poloidal flux ψ .

However, using just one coil to measure the complete flux, as in the case of Rogowski coils 2.9, does not give much information about plasma position. Mirnov Coils, on the other hand, are based on a number of discrete loops ranged around the perimeter of plasma that measure the poloidal field. So, the difference in the flux measured by the different loops gives the information related to plasma position, see figure 2.11. Loops ranged around outside the plasma give the boundary conditions for a solution of the differential equation governing ψ in the inner region [20].

Theoretically, in order to solve the equation in a closed region with bounding surface S , it may not only require the ψ value but also the derivative normal to the boundary, given by $\hat{\mathbf{n}} \cdot \nabla\psi$, over the entire surface S . So, if a perfect circular plasma is supposed, the flux loops will give the value of ψ in essentially every position of the plasma boundary and, thus, $\hat{\mathbf{n}} \cdot \nabla\psi$ is needed in a similar number of positions. In this case, as $\hat{\mathbf{n}} \cdot \nabla\psi$ is equal to $2\pi R$ times the tangential component of \mathbf{B}_p , the Mirnov coils are used to give the condition of S .

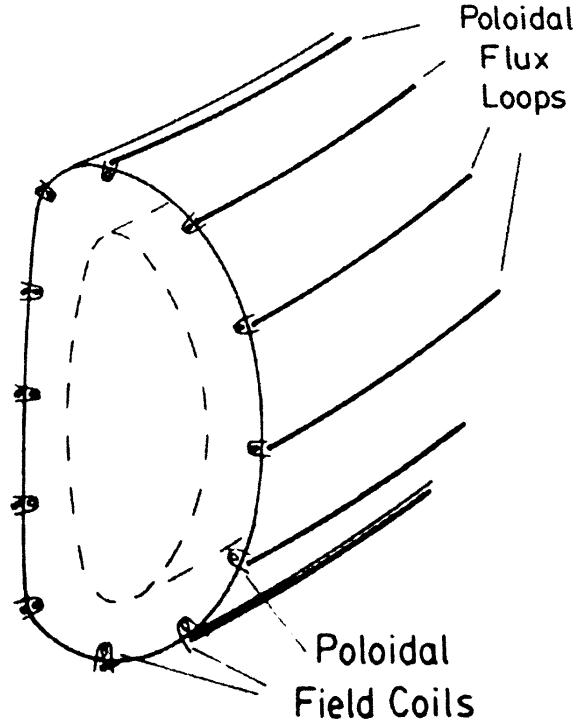


Figure 2.11: Plasma position measurements using Mirnov coils. [20]

However, for axisymmetric configurations such as tokamaks, the flux function must satisfy the following relationship:

$$\Delta^* \psi = -2\pi R \mu_0 j_\phi \quad (2.45)$$

Where the elliptic operator Δ^* is given by:

$$\Delta^* \equiv R^2 \nabla \cdot \left(\frac{\nabla \psi}{R^2} \right) = R \frac{\partial}{\partial R} \left(\frac{1}{R} \frac{\partial \psi}{\partial R} \right) + \frac{\partial^2 \psi}{\partial z^2} \quad (2.46)$$

Additionally, the equilibrium force balance within plasma the toroidal current density to be described by:

$$j_\phi = \frac{2\pi}{\mu_0} \left(\mu_0 R \frac{dp}{d\psi} + \frac{F}{R} \frac{dF}{d\psi} \right) \quad (2.47)$$

The flux equation substituted by j_ϕ in the expression above, 2.47 is the Grad-Shafranov relationship, described in equation 2.18.

The main purpose of magnetic diagnostics is to reconstruct as much information as possible about the flux function in a plasma region. Reconstruction based on vacuum fields, external fields and plasma equilibrium are discussed in lecture [20]. When these models

are developed, real-time control systems are able to provide feedback of the position and shape of the outermost flux surface, which is important for confinement experiments.

2.2.5 Hall Probes

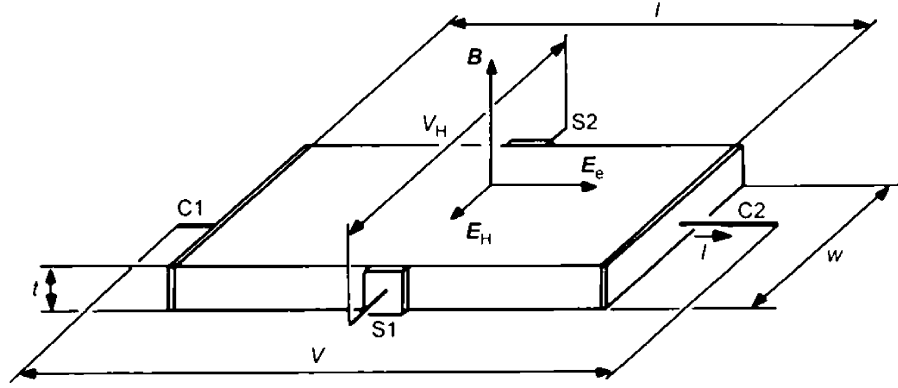


Figure 2.12: Schematic illustration of a Hall probe operating principle. [24]

Magnetic coils have one important drawback when measuring magnetic fields: they only respond to the rate of change of field \dot{B} and not to the field itself. So, for steady fields, magnetic coils are ineffective unless they can be moved within the field in a controlled way, a process that usually is very complicated on confinement machines. For these time invariant fields, as well as for the calibration process of coils in magnetic diagnostics, it is used a different physical process to sense the magnetic field: the Hall effect.

By definition [24], Hall effect is the induction of transverse Hall voltage due to electromotive force, which emerges in sample due to presence of electric current and perpendicular \mathbf{B} component at the same time. The electromotive force is proportional to the product of the intensity of the magnetic field and the velocity of the electricity. This relationship is described in the following equation:

$$\mathbf{E}_H \sim [\mathbf{v} \times \mathbf{B}] \quad (2.48)$$

Although the Hall effect take place in any medium, it is stronger in semiconductors. Considering that the plate in figure 2.12 is built in a semiconductor material with continuous media and common velocities, voltage drop between $C1$ and $C2$ induces an external electric field \mathbf{E}_e and the electric current densities of different charge carriers is given by the following equation:

$$\mathbf{J}_i = n_i q_i \mu_i \mathbf{E}_e \quad (2.49)$$

Where n_i represents the density and μ_i is the mobility of the respective i particles of charge q_i . Note that if an external magnetic field is present in this system, charge

carriers start to move in direction of the $q\mathbf{E}_e \times \mathbf{B}$ product. The resultant accumulation of charge carriers on the edge of the semiconductor plate lead to the generation of the Hall electric field \mathbf{E}_{Hi} . This field then cancels the initial magnetic force in order to fulfill the conditions of electromotive force equilibrium. Therefore, \mathbf{E}_{Hi} is given by the following relationship:

$$\mathbf{E}_{Hi} = -\mu_i \mathbf{E}_e \times \mathbf{B} \quad (2.50)$$

Additionally, the external electric field in equation 2.49 can be calculated as follows:

$$\mathbf{E}_e = \frac{V}{l} \mathbf{i} \quad (2.51)$$

Where V denotes the voltage across the current contacts $C1$ and $C2$, l is the total length of the plate and \mathbf{i} is the unity vector collinear with the longitudinal axis of the device.

Reference [24] describes how, by using 2.48 and 2.51, the Hall voltage V_H between $S1$ and $S2$ can be calculated using the following relationship:

$$V_H \simeq \frac{1}{qnt} IB \quad (2.52)$$

Where q denotes the magnitude of the electron charge, n is the carrier concentration in the plate and t is the plate thickness.

To use any semiconductor as a Hall probe, stable current I and temperature conditions need to be provided. Furthermore, it is important to highlight that, due to dependence on carrier density, semiconductor Hall probes are susceptible to radiation and to high-temperature damages [22].

2.3 General Parameters of MEDUSA-CR Spherical Tokamak

Table 2.1: Capacitative energy available in MEDUSA-CR bank of capacitors. [19]

Parameter	Value
Toroidal Field (TF)	41 kJ
Ohmic Heating (OH)	116 kJ
Vertical Field (VF)	17 kJ

General design parameters of MEDUSA-CR are shown in tables 2.2 and 2.1. Mechanical constraints, however, are given by the toroidal field coils and the vacuum vessel. External vacuum vessel of MEDUSA-CR tokamak is built in LS304 stainless steel, with a thickness

Table 2.2: Design and operation parameters for MEDUSA-CR spherical tokamak. [19]

Parameter	Value
Major Radius	0.09 m - 0.14 m
Minor Radius	0.04 m - 0.10 m
Aspect Ratio	1.5 (for 1.35 min)
Plasma Current	20 kA (40 kA max)
Toroidal Field	0.3 T (0.5 T max)
Pulse Length	1 ms (3 ms max)
OH Flux Swing	10 mV-s (on single swing)

of 7 mm, a height of 1.4 m and an external diameter of 1.34 m [12]. There are 26 half nipple ports located around the complete vessel surface: 6 with an external diameter of 13.25 in., 10 with an external diameter of 10 in., and 10 with an external diameter of 6 in.

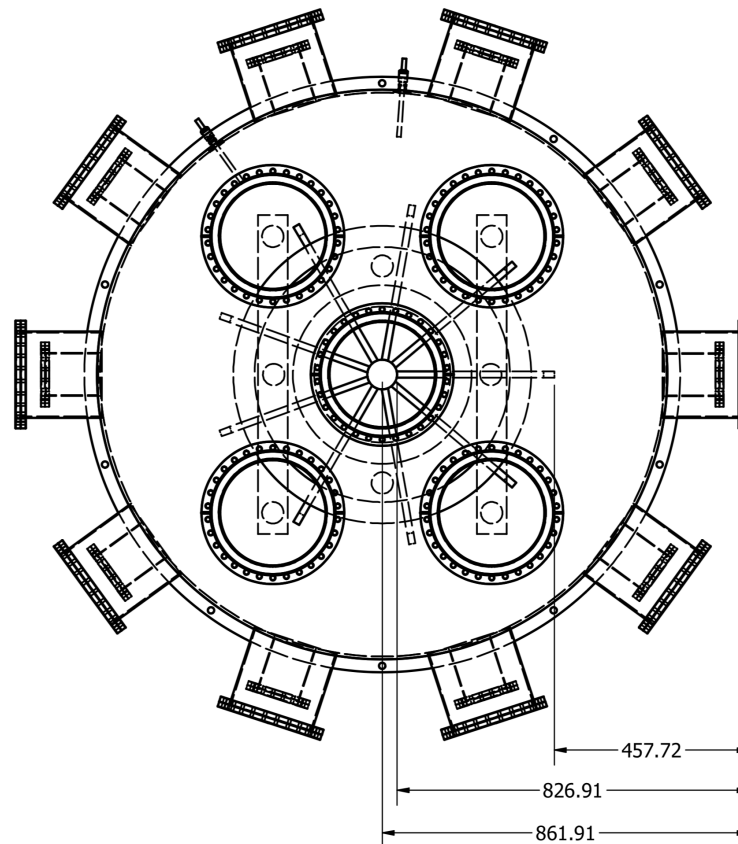


Figure 2.13: Top view diagram of MEDUSA-CR vacuum vessel in millimeters.

As it is shown in figure 2.13, the magnetic coils are located inside the vacuum chamber, and the distance from the mid-plane flange to the geometric center of the coils is 861.91 mm. So, the horizontal available perimeter inside the toroidal field coils is 369.19 mm.

Figure 2.14, on the other hand, gives the vertical constraints related to space disposal of

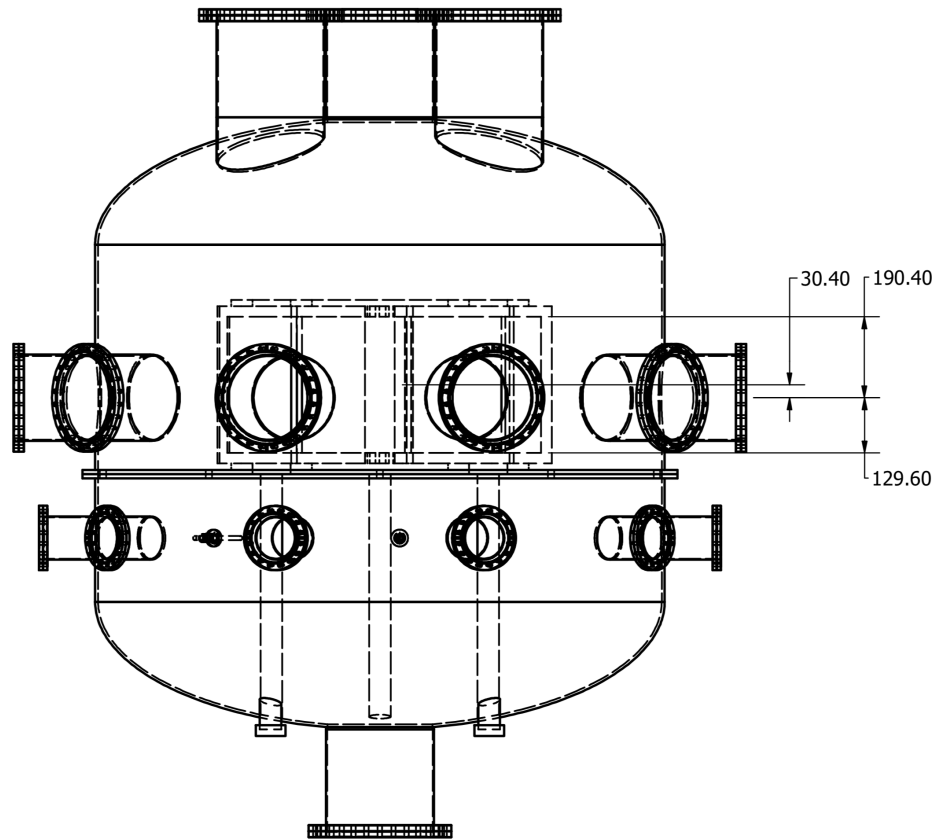


Figure 2.14: Side view diagram of MEDUSA-CR vacuum vessel in millimeters.

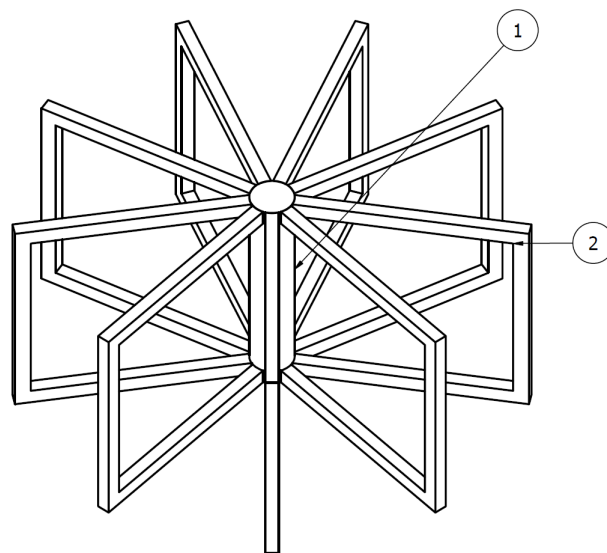
the coils and the vessel. The point of reference from which all the annotations are taken is located on the geometric center of the right-end half nipple section area. It is important to note that there is a 30.40 mm gap between the y-axis center of the coils and the y-axis center of the half nipples. Additionally, the vertical available perimeter inside the toroidal field coils is 320 mm.

Chapter 3

The Magnetic Diagnostics

3.1 Mirnov Coils System

3.1.1 Mechanical Design



PARTS LIST		
ITEM	QUANTITY	PART NUMBER
1	1	Central Coil
2	9	Toroidal Field Coil

Figure 3.1: MEDUSA-CR toroidal and central coils assembly.

As it is mentioned in section 2.2.4, the Mirnov coils system is conformed by several discrete coils located near the perimeter of plasma that measure local magnetic fields \mathbf{B} . So, in order to decide the amount of coils and their dimension, it is important to calculate the mechanical constraints of the MEDUSA-CR tokamak.

Since the vacuum vessel is located externally of the main coils [12], see figure 1.2b, the dimensional constraints for the Mirnov coils system is given by the toroidal field coils, shown in figure 3.1.

In total, there are 9 toroidal field coils arranged in a circular pattern around the central coil with an angular displacement of 40° . Each of the toroidal field coils individually surround a horizontal space of 34.5 cm and a vertical space of 32.0 cm, where plasma is generated. See figure 3.2.

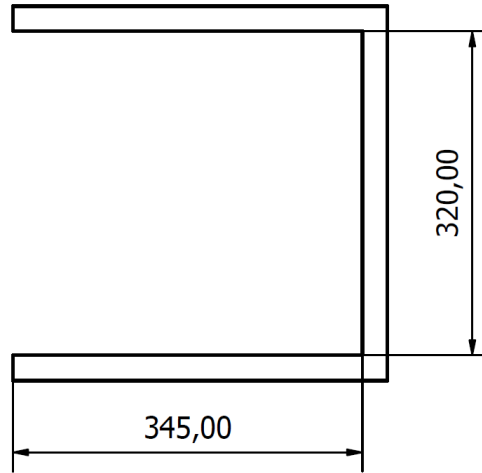


Figure 3.2: MEDUSA-CR toroidal field coil dimensions diagram in millimeters.

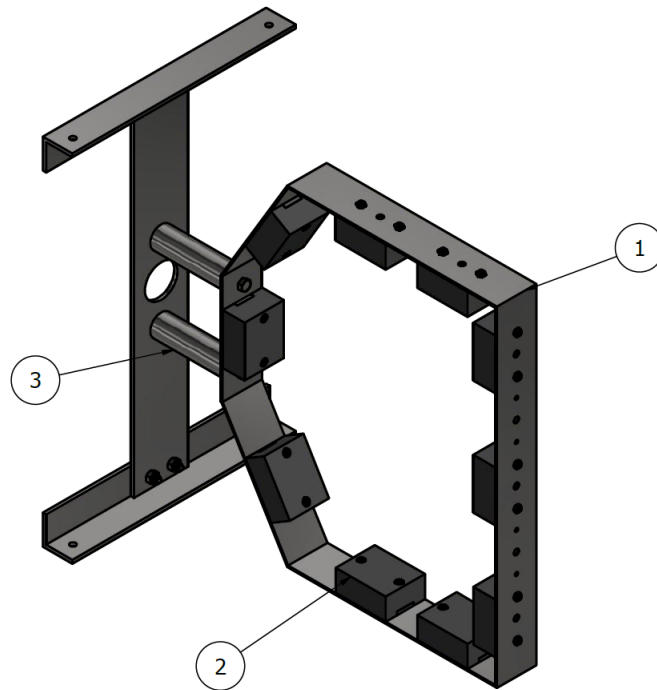


Figure 3.3: Mirnov coils structural assembly for the MEDUSA-CR tokamak.

Additionally, flux contour measurements on figure 2.5, made by author [19], shows a D-shaped plasma with a size delimited by a horizontal position of $R < 20$ cm and a vertical position of $-10 \text{ cm} < Z < 10$ cm.

So, in order to obtain a reliable data, the Mirnov coils must be installed as close as possible to plasma. However, if plasma has direct contact with any of the coils, the system will be damaged.

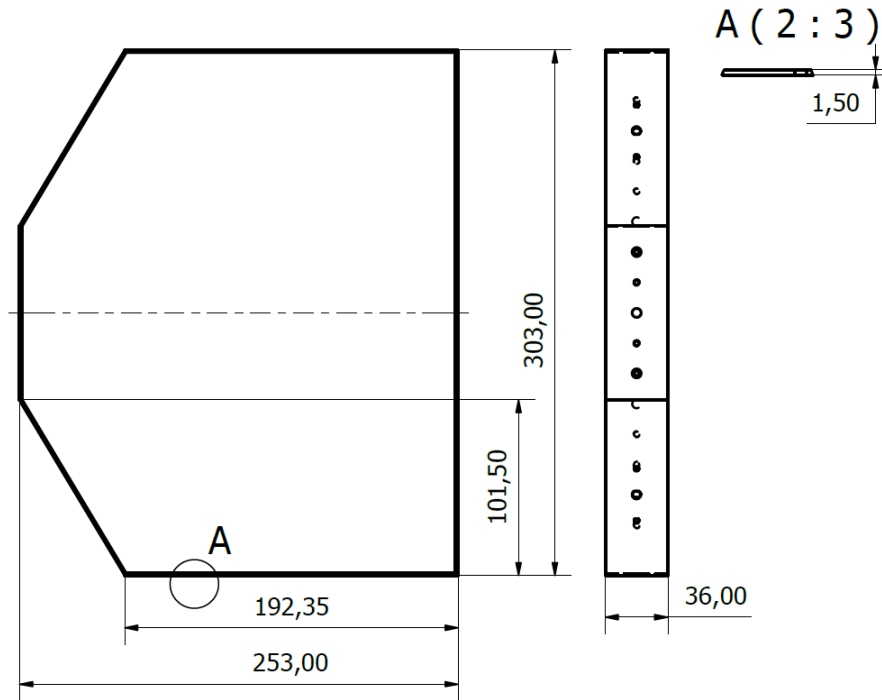


Figure 3.4: D-shape Mirnov coils support dimensions diagram in millimeters.

Taking into consideration the mechanical constraints listed above, a D-shape support structure is designed to enclose plasma precisely. Figure 3.3 shows the Mirnov coils complete system which is based on three main parts: (1) the D-shape Mirnov coils support system, (2) the Mirnov coils and graphite shield assembly and (3) the cylindrical fixation for the Mirnov coils D-shape support system.

The D-shape Mirnov coils support system, constructed on a 1.5 mm thick 316L stainless non-ferromagnetic steel sheet (a standard material in tokamak engineering [22]), has a total length of 25.3 cm, a total height of 30.3 cm and a total width of 3.6 cm. Both, material and dimension are chosen to reduce the presence of stray fields generated by MEDUSA-CR principal coils. Figure 3.4 shows the main annotations of the D-shape Mirnov coils support.

An arrangement of 10 coils is designed for MEDUSA-CR in order to maximize the data acquisition resolution while using the available space between the toroidal field coils and plasma. A custom graphite shield protects each of the coils from exposure to plasma and acts as a limiter. Expert in [8] indicates that graphite is the ideal material to construct these shields because of its thermal and magnetic properties. Furthermore, the manufac-

turing process of graphite is not expensive and is available from several providers. Figure 3.5 shows an exploded view of the Mirnov coils and graphite shield assembly.

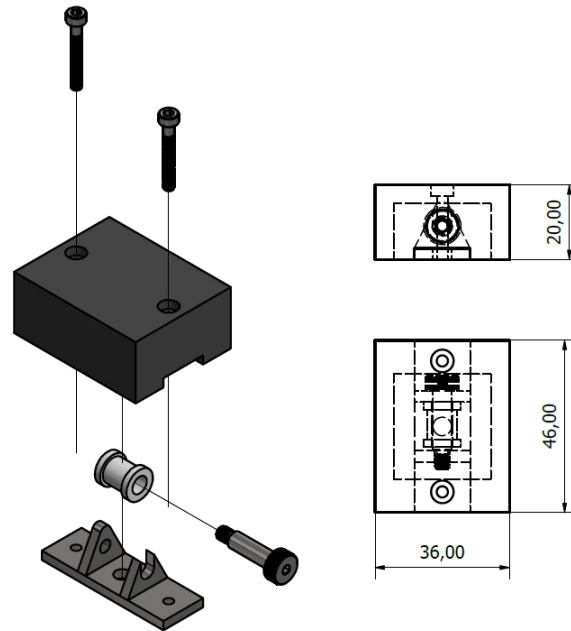


Figure 3.5: Views of the Mirnov coil and graphite shield assembly in millimeters.

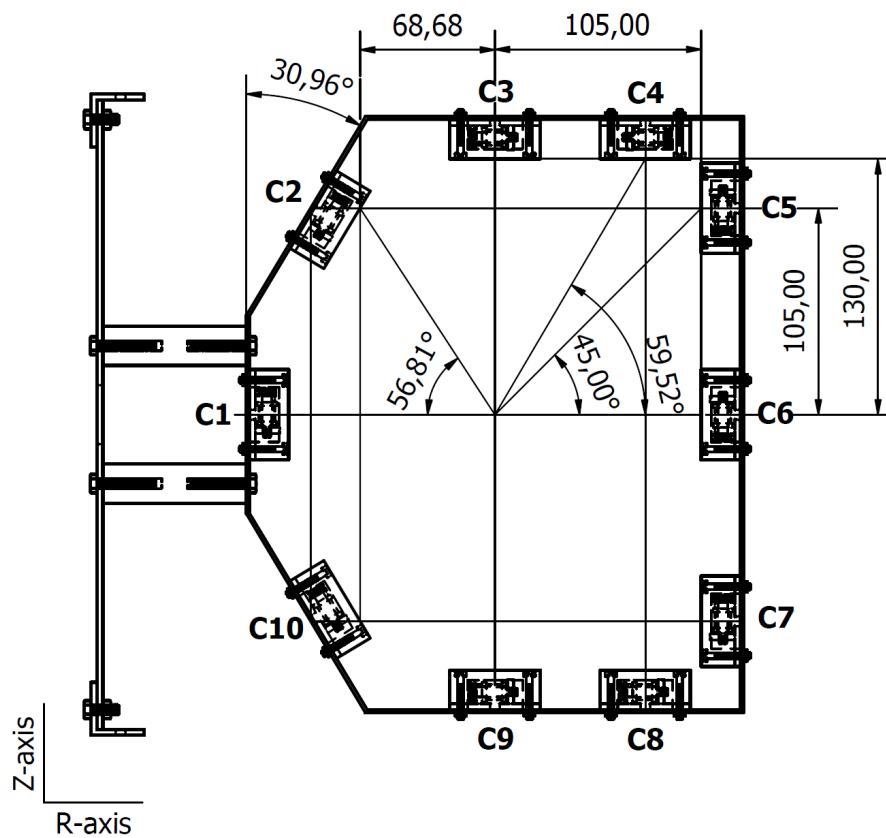


Figure 3.6: Mirnov coils position diagram in millimeters.

Figure 3.6 shows the position of each designed Mirnov coils around the D-shape support system. Coils are named from C1 to C10 in clockwise direction. Taking the reference point $(R, Z) = (0, 0)$ cm from the center of the D-shape support system, C1 $(-10.5, 0)$ cm and C6 $(10.5, 0)$ cm are located on the boundary of the R-axis, and C3 $(0, 13)$ cm and C9 $(0, -13)$ cm are located on the boundary of the Z-axis. Additionally, C2 and C10 are designed to have an angular location of $\pm 30, 96^\circ$ from the Z-axis. It is also important to notice that the geometrical centers of each coil are aligned with the opposites to enhance better results on plasma position measurements.

Although there are 10 Mirnov coils in the system, fixation holes and space between C5, C6 and C7 are provided to add two more coils if necessary. Each element is easily removable from the D-shape support system for substitution and maintenance. Additionally, a central hole on the bottom of the coil-shield assembly is designed to safely extract the connection wires.

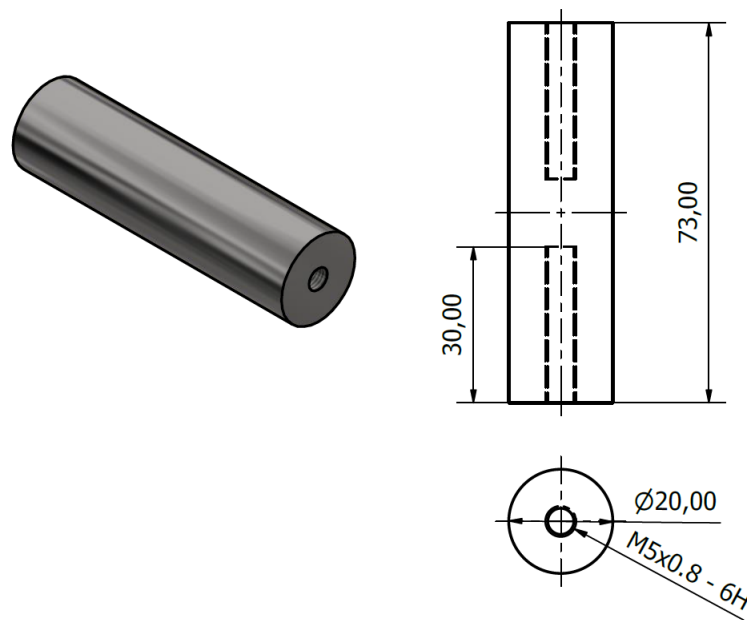


Figure 3.7: Cylindrical fixation for the Mirnov coils D-shape support system.

The cylindrical fixation for the D-shape support system is shown in figure 3.7. This element, constructed in the same 316L stainless non-ferromagnetic steel, is designed to maintain the D-shape support system as close as possible to the MEDUSA-CR central coil. Diagnostics proximity to the central coil is an important feature due to the spherical confinement found in MEDUSA-CR. In this way, more information could be extracted from plasma geometry during a shot. Additionally, a pair of $M5 \times 0.8$ screws keep this element together with other structural parts to enable future modifications and repairs.

3.1.2 Electronic Design

The first aspects to take into consideration before designing the coils for the Mirnov system are the mechanical constraints discussed in section 3.1.1. Comparison between the MEDUSA-CR plasma size in figure 2.5 and the D-shape support system overall dimensions in figure 3.4 leaves an available space for the coils of 5.3 cm in the horizontal plane (R-axis) and 10.3 cm in the vertical plane (Z-axis). Furthermore, considering that the system has a pair of coils in opposite location, D is determined by the following calculations:

$$D_{R-axis} < \frac{5.3cm}{2} = 2.65cm \quad (3.1)$$

And

$$D_{Z-axis} < \frac{10.3cm}{2} = 5.15cm \quad (3.2)$$

So, the critical condition is given by $D < 2.65$ cm in relationship 3.1. Furthermore, since plasma should not have direct contact with the coil, an additional security space has to be considered in order to include the graphite shield assembly in figure 3.5. So, based on the method of concurrent design [16] the following coils dimensions are established:

Table 3.1: Coils design parameters.

Parameter	Value (mm)
Coil Length (l)	8
Coil Diameter (D)	10
Core Diameter (D_i)	5.5

Substituting the values of table 3.1 in the relationship 2.31, which calculates the ratio between the length l and the diameter D of the coil, the following results are obtained:

$$K = \frac{l}{D} = \frac{8mm}{10mm} = 0.8 \quad (3.3)$$

Considering that author in [31] recommends a $K \sim 0.866$ for measurements in non-homogeneous fields, the chosen parameters give a correct approach of $K = 0.8 \sim 0.866$. Boron-nitride is the chosen material to construct the coils due to its good thermal properties and ease to manufacture. Figure 3.8 shows the final result of the Mirnov system CAD design of the coil. Furthermore, figures 3.5 and 3.6 give the relationship between the coil mechanical dimensions and the complete mechanism.

System resonance frequency is a signal constraint that has to be considered during the design of magnetic diagnostics. Previous experiments developed in MEDUSA-CR by author [19] manifested coherent data from magnetic oscillations in local poloidal fields

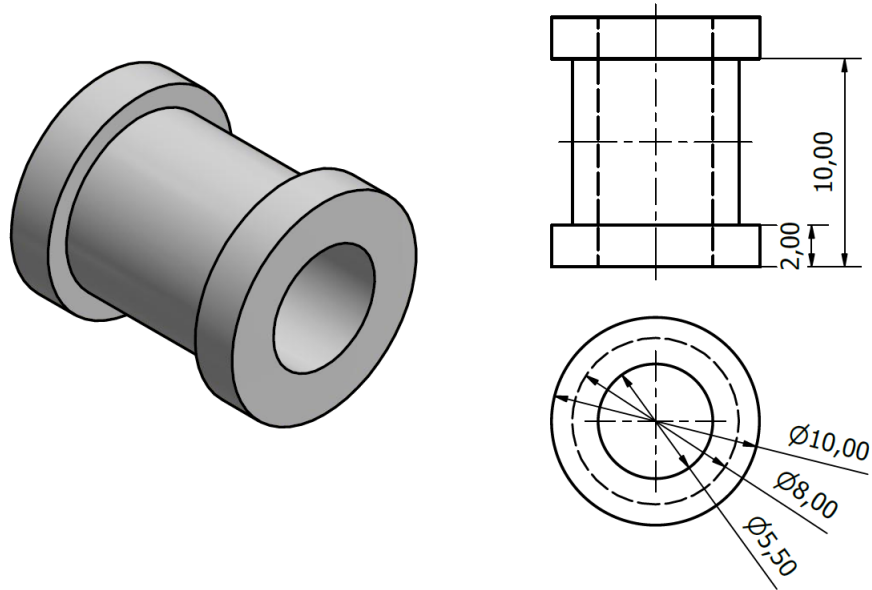


Figure 3.8: Dimensions diagram for the designed boron-nitride Mirnov coils.

at 65-75 kHz. So, for each of the Mirnov coils, response frequency should be given by $f_{res} > 75$ kHz.

Let the response frequency of the Mirnov coils be determined by the following relationship:

$$f_{res} \sim \frac{1}{2\pi\sqrt{LC}} > 75kHz \quad (3.4)$$

Where, for thin wire coils, L is given by equation 2.35 and $C \sim 100$ pF/m [31] (excluding the integration circuit).

Table 3.2: Parameters of chosen copper wire with $d = 0.1$ mm. [6].

Parameter	Value
Max. Voltage	2000 V_{DC}
Max. Current	0.1 A
Resistivity	2270 Ω/km
Conductor Diameter	0.1 mm
Thermal Range	-269 °C to 260 °C

Now that the relationship between the response frequency, inductance and capacitance is established, the next step is to chose wire diameter d . Equation in 2.30 shows that for larger wire diameters, the generated signal from coils U_{sig} decreases. So, in order to increase U_{sig} as much as possible, a thin wire has to be chosen. For vacuum conditions, KaptonTMinsulated copper wires are available in the market with a minimum of $d = 0.1$ mm [6]. Table 3.2 shows the parameters of the chosen wire.

An approximate length of 5 meters copper cable is selected for each of the Mirnov coils based on MEDUSA-CR dimensions, shown in section 2.3. For this case, $C \sim 500$ pF. Now, by substituting the values on equation 3.4 and solving the relationship for L , it is obtained the expected inductance value of each coil for a resonance frequency of 75 kHz.

$$\left(\frac{1}{75kHz \times 2\pi}\right)^2 > (L \times 500pF)^2 \quad (3.5)$$

Which gives $L < 9000 \mu\text{H}$ as the condition for the maximum inductance of each Mirnov coil.

Taking now into consideration the selected copper wire diameter $d = 0.1$ mm and the design parameters of the Mirnov coils in figure 3.8, expected inductance, resistance and effective area of the coils can be calculated with equations 2.35, 2.34 and 2.26 respectively. It is important to note that each coil has 2 winding layers N_l to fix the wire on the core of the coil and avoid unwanted displacements. The obtained results are summarized in the following table:

Table 3.3: Expected results for the Mirnov coils parameters. See section A.1.

Parameter	Value
Inductance (L)	106.2 μH
Resistance (R)	8.8 Ω
Turns per layer (n)	80
Effective Area (A_{eff})	89 cm^2

With the obtained results from table 3.3, the response frequency of each coil is calculated:

$$f_{res} \sim \frac{1}{2\pi\sqrt{106.2\mu\text{H} \times 500p\text{F}}} = 690kHz \quad (3.6)$$

The previous result is compared with the frequency condition established in 3.4. The obtained f_{res} value from the selected design parameters in 3.6 fulfill the requirements since $690 \text{ kHz} > 75 \text{ kHz}$. So, the Mirnov coils designed are suited for future high-frequency experiments. Furthermore, the inductance value L also satisfies the condition presented in 3.5, were $106.2 \mu\text{H} < 9000 \mu\text{H}$ for the required f_{res} of 75 kHz.

The signal from coil is directly related to the local magnetic field fluctuation B_0 . By substituting the design parameters in 2.30, the coil signal U_{sig} is calculated as follows:

$$U_{sig} = 32.3 \times 10^3 \dot{B}_0 \quad (3.7)$$

3.2 Diamagnetic Loop System

3.2.1 Mechanical Design

In contrast with the Mirnov coils system, the diamagnetic loop is designed to measure total fluctuations of plasma magnetic field \mathbf{B} . So, in order to obtain the correct data, the system designed coil must enclose completely the plasma contour.

As it is shown in figure 3.2, the available horizontal and vertical spaces are 34.5 cm and 32.0 cm respectively inside the toroidal coils of MEDUSA-CR. Furthermore, generated D-shaped plasma has a horizontal section $R = 20$ cm and a vertical section of $Z = 20$ cm, see figure 2.5. With the known mechanical constraints, the diamagnetic loop structure is designed following the same process described in section 3.1.1.

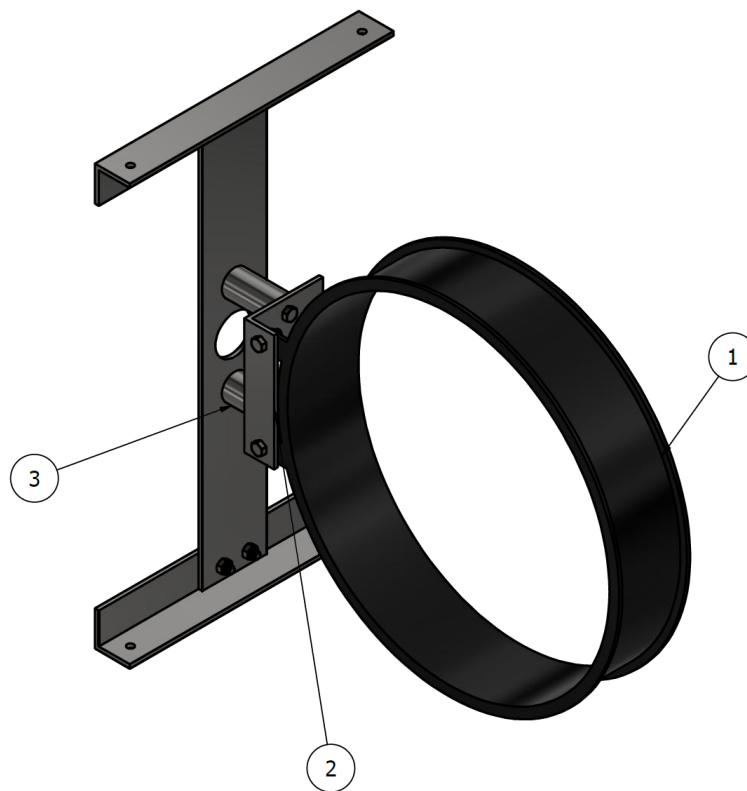


Figure 3.9: Parts diagram of the diamagnetic loop support system.

Figure 3.9 shows the complete diamagnetic loop system mechanical design for the MEDUSA-CR tokamak. The system is composed of three main components which are enumerated from 1 to 3. The diamagnetic loop main support (1) is fixed by the L-shape bracket (2) and the cylindrical fixation (3) to keep a correct position inside the toroidal field coils of MEDUSA-CR.

The diamagnetic loop main support is the principal element of the mechanism. It is designed to held the copper wire coil around the plasma surface and has a dimension of 26.5 cm to the most external diameter and 25.0 cm to the most internal diameter. Two

parallel straps are designed to set the circular structure to the other components of the system. Furthermore, the main support acts as the winding core and is built entirely of graphite, the same material selected for the Mirnov coils shielding (see section 3.1.1). A graphite structure is selected to avoid stray magnetic fields and to protect the copper wire from direct exposure to plasma. Figure 3.10 shows main dimensions of the element.

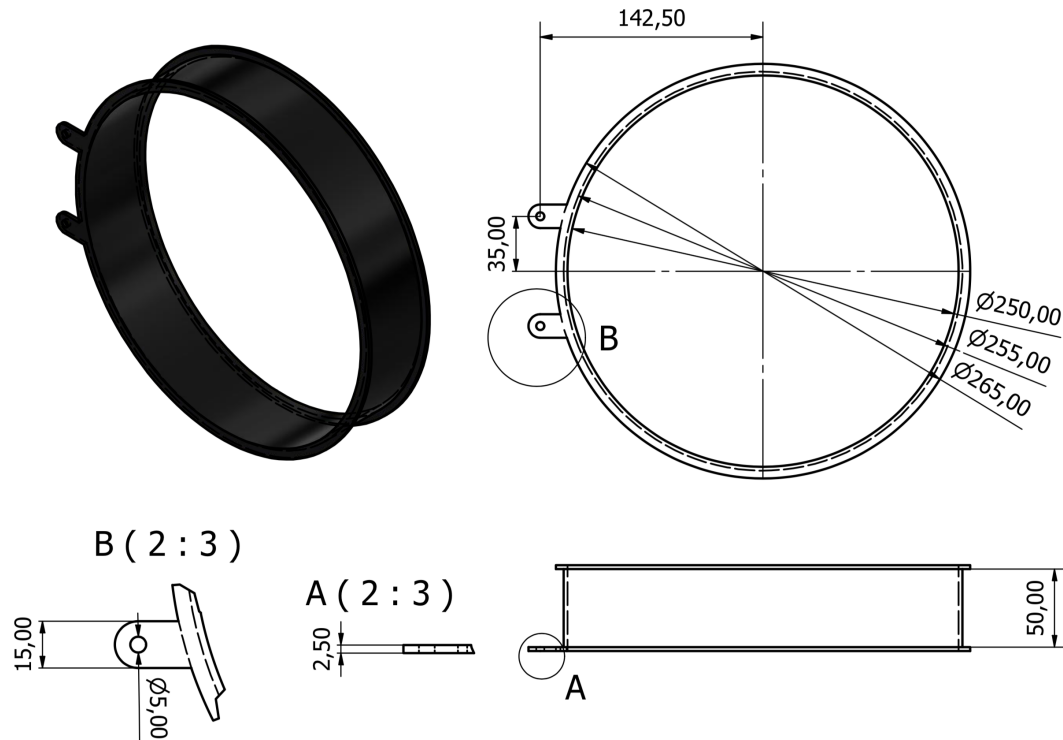


Figure 3.10: Dimensions diagram for the diamagnetic loop main support in millimeters.

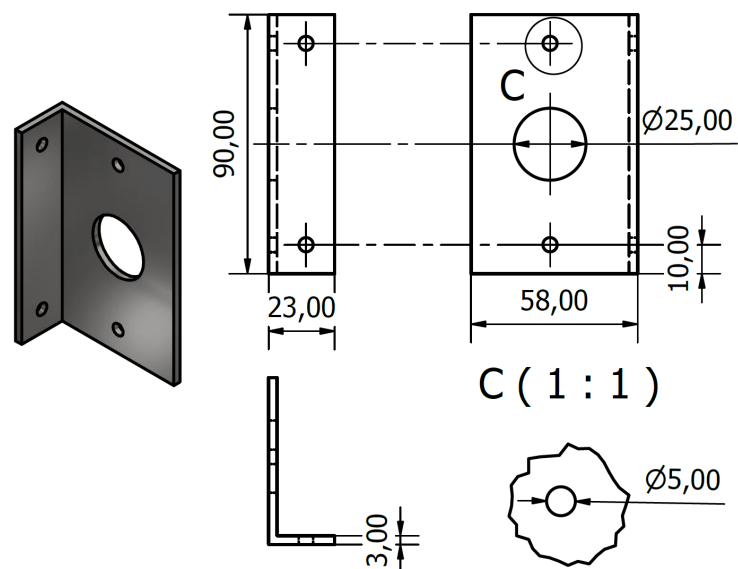


Figure 3.11: Dimensions diagram for the diamagnetic loop L-shaped bracket in millimeters.

On the other hand, the L-shaped bracket, see figure 3.11, joins up the main support with the entire system. It is designed on a 3 mm sheet of 316L stainless non-ferromagnetic steel and has two faces in an angular configuration with a 90° bent. Both of these faces have two concentric 0.5 cm holes for fixation screws, and a 2.5 cm central hole is provided in the larger side as a wire feedthrough.

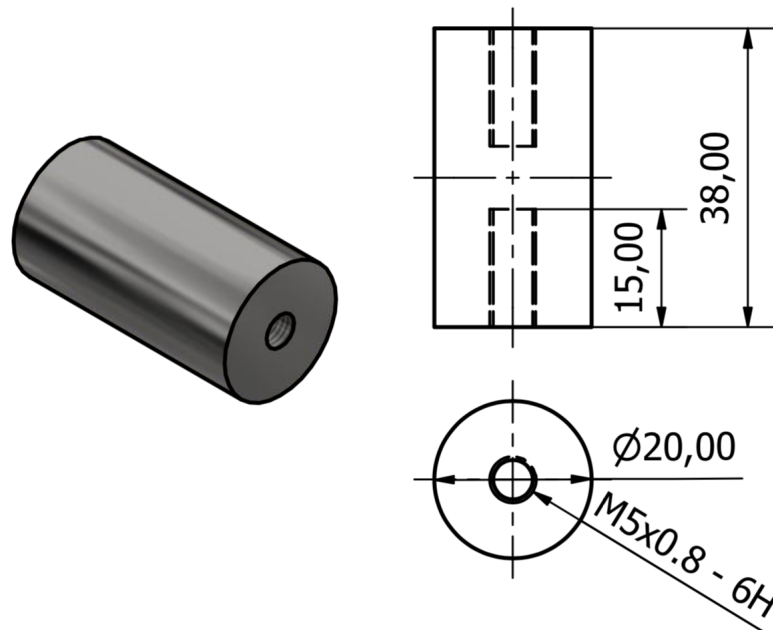


Figure 3.12: Dimensions diagram for the cylindrical fixation in millimeters.

There are two cylindrical fixations in the diamagnetic loop mechanism, see figure 3.12 and figure 3.9. Similar to Mirnov coils support system, this fixation is constructed in 316L stainless non-ferromagnetic steel and maintain the main diamagnetic coil as close as possible to the MEDUSA-CR central coil. This fixation element has a total diameter of 2 cm and a length of 3.8 cm. Additionally, a pair of 0.5 cm holes in both of its faces are designed to house two $M5 \times 0.8$ screws to keep the entire structure together. It is important to note that the entire system uses non permanent unions between its parts to enable future modification and maintenance.

3.2.2 Electronic Design

The principal constraint to design the diamagnetic loop coils is mechanical space. As it is discussed in the previous section, the mechanical support system is disposed to enclose plasma as closer as possible without exposing the copper wire. Since the diamagnetic loop measures the total magnetic fluctuation in plasma, the system resonance frequency f_{res} is not as high as in Mirnov coils. Based on recommendation from authors [9] and [8], $f_{res} < 20$ kHz is the chosen range for the design frequency. Selecting this frequency correctly is important to obtain the desired data while avoiding high frequency noise.

Based on figure 3.10 the following design parameters are established.

Table 3.4: Diamagnetic loop coil design parameters.

Parameter	Value (mm)
Coil Length (l)	50
Coil Diameter (D)	255
Core Diameter (D_i)	250

Now that the coil dimensions are established, it is necessary to chose the wire diameter d . Additional to the option shown in table 3.2, provider in [6] also offers a 0.25 mm copper wire suited for vacuum conditions. Operation values of this wire are shown in the next table.

Table 3.5: Parameters of chosen copper wire with $d = 0.25$ mm. [6].

Parameter	Value
Max. Voltage	2000 V_{DC}
Max. Current	1 A
Resistivity	360 Ω/km
Conductor Diameter	0.25 mm
Thermal Range	-269 $^{\circ}\text{C}$ to 260 $^{\circ}\text{C}$

Since the coil core is designed with a large diameter D_i to enclose plasma, the winding process difficulty is increased. To ease the manufacture of the coil, a thicker copper wire with diameter of $d = 0.25$ mm is chosen without affecting significantly the signal output U_{sig} . Furthermore, the coil has two winding layers $N_l = 2$ to avoid unwanted displacements of the wire over each turn. Expected design parameters for the coil inductance, resistance and effective area are now calculated by substituting values in equations 2.35, 2.34 and 2.26 respectively. The obtained results are shown in the following table.

Table 3.6: Expected parameters for the diamagnetic loop coil. See section A.2.

Parameter	Value
Inductance (L)	100.7 mH
Resistance (R)	109 Ω
Turns per layer (n)	200
Effective Area (A_{eff})	20.2 m^2

Author [31] mentions that for thin wire coils their capacitance is given by $C \sim 100$ pF/m. For MEDUSA-CR, considering the dimensions of the coil core and the distance between the probe location and the nearest port, a 10 meter wire is chosen for the diamagnetic loop. In this case, $C \sim 1000$ pF.

Then, the resonance frequency of the coil is calculated by substituting the previously discussed values of C and L in equation 3.4.

$$f_{res} \sim 15.8kHz \quad (3.8)$$

As it is seen in relationship 3.9 the condition for $f_{res} < 20$ kHz is fulfilled. However, it is important to highlight that if a wire diameter $d = 0.1$ mm is chosen, the system will also fulfill the frequency requirement by augmenting the resistance R . However, while choosing this wire diameter increases the coils signal U_{sig} , it also creates a difficult winding process during coil construction.

$$f_{res_{0.1mm}} \sim 6.3kHz \quad (3.9)$$

For comparison, the following table shows the calculations for inductance L , resistance R and effective area A for the designed diamagnetic loop with a $d = 0.1$ mm wire, the same used in the Mirnov coils.

Table 3.7: Expected parameters for the diamagnetic loop coil with a $d = 0.1$ mm wire.

Parameter	Value
Inductance (L)	629.2 mH
Resistance (R)	1.7 k Ω
Turns per layer (n)	500
Effective Area (A_{eff})	51.3 m ²

The signal from the coil is directly related to the total time varying magnetic field \dot{B} . By substituting the design parameters of tables 3.6 and 3.7 into equation 2.38, the following results are obtained.

$$U_{sig} = nA_{eff}\dot{B} = 8.1 \times 10^3 \dot{B} \quad (3.10)$$

$$U_{sig_{0.1mm}} = 51.3 \times 10^3 \dot{B} \quad (3.11)$$

3.3 Rogowski Coil System

3.3.1 Mechanical Design

The Rogowski coil system is designed to measure the total current I from plasma in MEDUSA-CR. As it is explained in section 2.2.3, the mechanical support has to enclose plasma in order to obtain the desired signal U_{sig} . Author [8] explains that there are to

ways to measure correctly the current during a plasma discharge: (1) by installing the Rogowski coil outside the vacuum vessel, as in GOLEM tokamak in figure 1.2a, or (2) by installing the coil inside the vacuum vessel, as in COMPASS tokamak in figure 1.2.

In the case of MEDUSA-CR, the vacuum vessel is external to the confined plasma. So, measuring the plasma current from the outside is not possible. For this, an internal mechanical support system, similar to the one described in section 3.2.1, is designed to hold the Rogowski coil between the toroidal field coils of the tokamak and plasma.

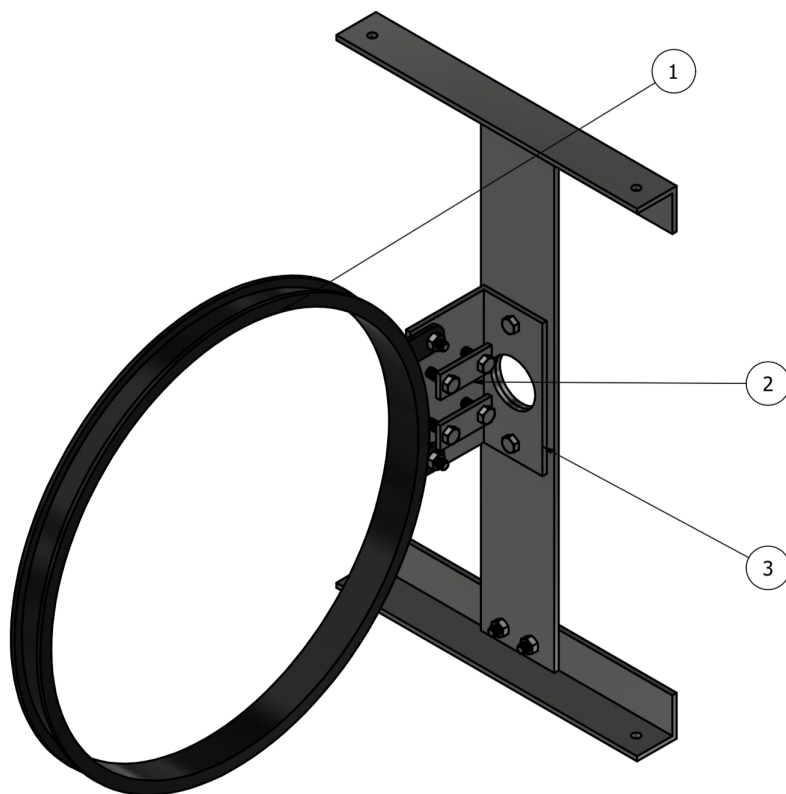


Figure 3.13: Parts diagram of the Rogowski coil support system.

Figure 3.13 shows the complete mechanical support system for the internal Rogowski coil in MEDUSA-CR tokamak. As it is seen, the structure is composed of 3 main parts: (1) the main support ring, (2) the pressing brackets and (3) the L-shaped holder.

The rogowski coil main support is the principal element of the system. Its dimensions are established to fit inside the toroidal field (TF) coils of MEDUSA-CR, see figure 3.2. As it is seen in figure 3.14, the ring is completely constructed in graphite to tolerate high temperature and vacuum conditions [8]. A total inner diameter of 25 cm is left to avoid contact with plasma. Furthermore, a width of 1.5 cm is designed to act as a rail where the Rogowski coil is attached. This rail avoids unwanted displacements generated from structural vibrations during tokamak operation.

In contrast with the L-shaped holders from the Mirnov coils and diamagnetic loop systems, shown in sections 3.1.1 and 3.2.1 respectively, the Rogowski coil L-shaped holder (3) is the only joint between the main support ring and the Fixing Structure, discussed

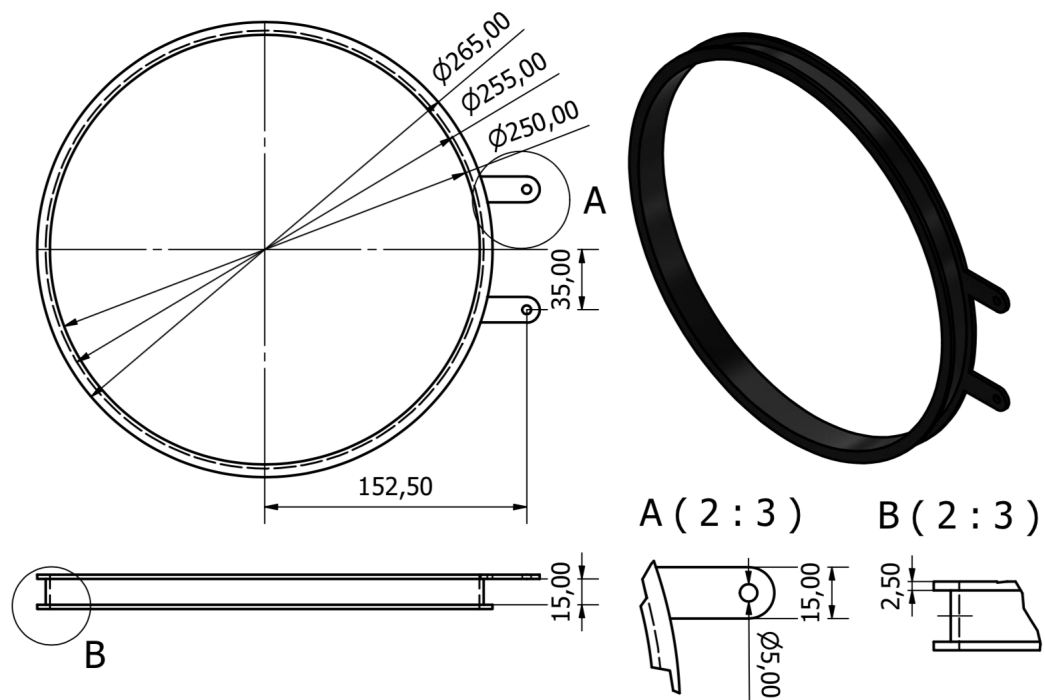


Figure 3.14: Dimensions diagram in millimeters for the main support ring of the Rogowski coils system.

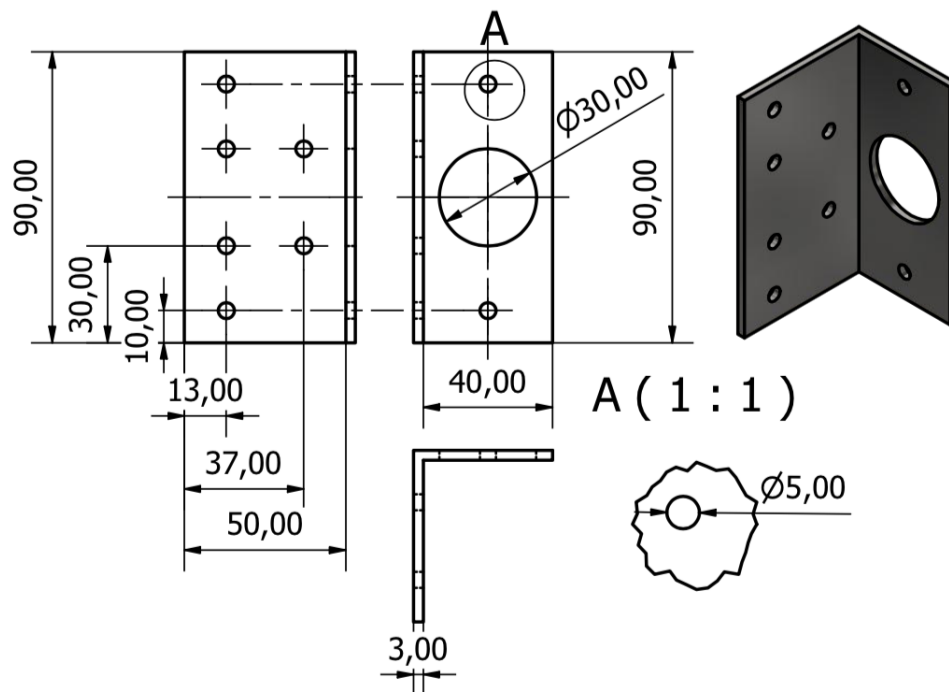


Figure 3.15: Dimensions diagram in millimeters for the L-shaped holder of the Rogowski coils system.

later in section 3.4.

Figure 3.15 shows the main annotations of the L-shape holder. As it is illustrated, the part is made entirely in 316L stainless-steel and has a thickness of 3 mm. The principal face of this element is shown in the left side the diagram in figure 3.15 and has a total length of 5 cm and a height of 9 cm. Six holes with a diameter of 5 mm are designed on it, horizontally symmetric, to join the main support ring (1) with the pressing brackets (2).

On the other hand, the secondary side has three concentric holes. The central hole is used as a feedthrough to enable the wires of the copper Rogowski coil to be extended out of the toroidal field region. The other two holes have a diameter of 5 mm to enable two M5 × 0.8 screws attach the system with the Diagnostics Fixing Structure, discussed later in section 3.4.

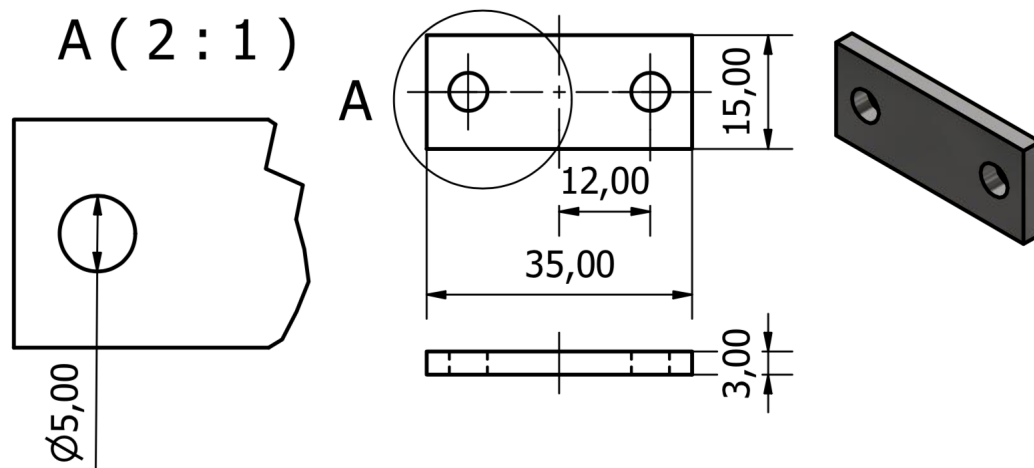


Figure 3.16: Dimensions diagram in millimeters for the pressing brackets of the Rogowski coils system.

The last elements of the Rogowski coil mechanical system are the pressing brackets shown in figure 3.16. These elements are designed in 316L stainless-steel to hold the coil in the correct position so that the loop is closed as much as possible, creating the geometry explained in figure 2.9. With a length of 3.5 cm, a height of 1.5 cm and a thickness of 3 mm, its mechanical fixation is completely adjustable to the coil diameter. Furthermore, two holes with a 5 mm diameter are designed on the primary face of the pressing brackets in order to bear the M5 × 0.8 screws.

3.3.2 Electronic Design

The main constraints related to the electronic design of the Rogowski coil system are the plasma circumference, which is shown in figure 2.5, and the coil wire diameter. Resonant frequency f_{res} , in contrast with the previous magnetic diagnostics, is not a critical design aspect because total plasma current detection occurs at lower frequencies [8].

Now that the mechanical constraints have been established on the previous section, a wire

type is chosen. As winding is important to create more precision during measurements, the conductor diameter must enable tight loops and mechanical stability for a high number of turns. Provider in [6] offers a wire with a 0.25 mm conductor diameter, the same used for the diamagnetic loop system, suited for vacuum. Operation parameters of this cable are shown in table 3.5.

In order to construct the closed loop for current measurements, the thinner wire previously described is wound around a 16-AWG vacuum isolated cable with a total length of 1.2 m. For signal return described in figure 2.9, the thinner wire is welded to one end of the thicker wire after winding is completed. Voltage output U_{sig} can then be measured between other ends of both cables.

Operational parameters of the thicker wire are shown in the following table:

Table 3.8: Parameters of the chosen 16-AWG KaptonTMinsulated wire [25].

Parameter	Value
Max. Voltage	600 V_{AC}
Max. Current	11 A
Resistivity	20.6 Ω/km
Max. Vacuum Level	10×10^{-10} Torr
Conductor Diameter	1.29 mm
Insulation Diameter	6 mm
Thermal Range	-250 °C to 250 °C

To calculate inductance L , resistance R and number of turns n , the core parameters are defined by the 16-AWG cable. So, making an analogy between the information in table 3.8 and figure 2.7 the following core dimensions are established:

Table 3.9: Rogowski core design parameters.

Parameter	Value (mm)
Coil Length (l)	1200
Core Diameter (D_i)	7.29

Now that the core length l is defined, the number of turns in the Rogowski coil can be calculated by the following expression:

$$n = \frac{1200\text{mm}}{0.25\text{mm}} = 4800 \quad (3.12)$$

Substituting the information calculated previously in equations 2.34 and 2.35 respectively, resistance and inductance can be calculated. The following table shows the expected parameters of the Rogowski coil:

Table 3.10: Expected results for the Rogowski coil parameters. See section A.3.

Parameter	Value
Inductance (L)	1.5 mH
Resistance (R)	60.2 Ω
Turns per layer (n)	4800
Effective Area (A_{eff})	267.7 m^2

Substituting in 2.43, the theoretical value for U_{sig} is given as follows.

$$U_{sig} = 1.606\dot{I} \quad (3.13)$$

3.4 Diagnostics Fixing Structure

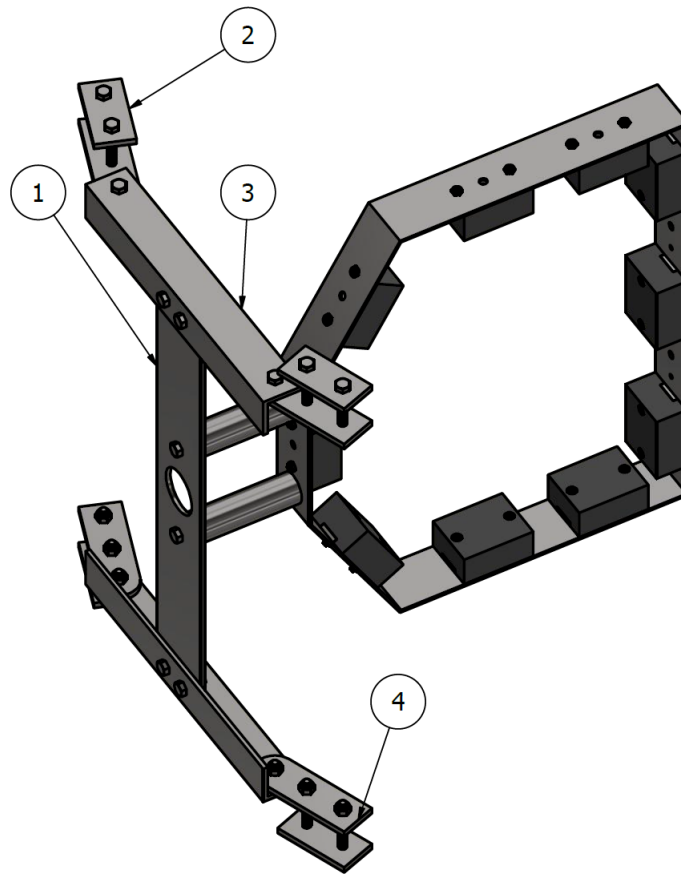


Figure 3.17: Fixing Structure diagram from the Mirnov coils system.

The three diagnostics are mounted on a identical support system called the Fixing Structure. This mechanism is designed to join the main mechanical elements from the diagnostics with the toroidal field coils from MEDUSA-CR. It is entirely designed in 316L

stainless non-ferromagnetic steel and provides support to locate each of the diagnostics in the correct position between the central coil and plasma region.

As it is shown in figure 3.17, the Fixing Structure is composed by four main elements, some of which are repeated in the mechanism. The central bar (1) joins together the Mirnov coils system with two L-shaped bearings (3). These bearings are attached to the MEDUSA-CR toroidal field coils by the pressing holders (2) and (4).

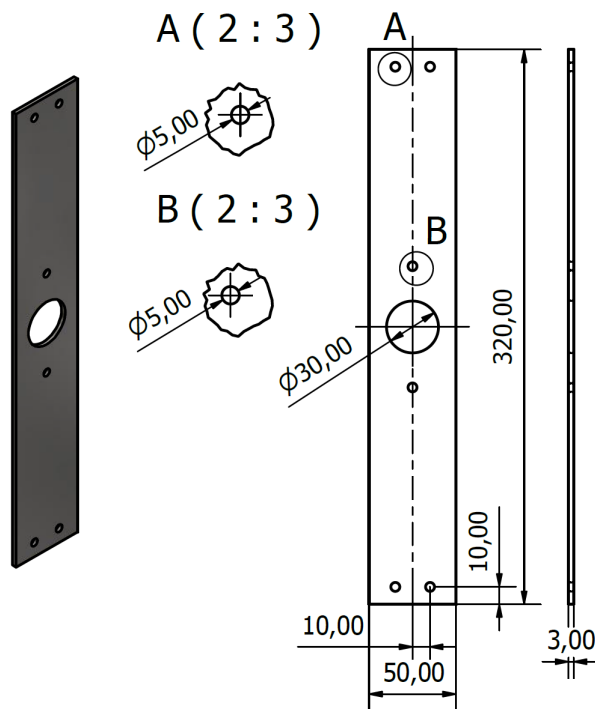


Figure 3.18: Central bar diagram in millimeters of the Fixing Structure.

The central bar element of the Fixing Structure is shown in figure 3.18. This part has a width of 5 cm and a length of 32 cm and a thickness of 3 mm. In total, there are six 5 mm holes located symmetrically on both faces of the central bar that house the $M5 \times 0.8$ screws used for fixation. Additionally, a central 3 cm hole is also designed as feedthrough for diagnostics wiring components.

On the other hand, the L-shape bearings are designed to connect the diagnostics mechanical system to the pressing holders. They have a total length of 20.5 cm and two faces with a width of 2.7 cm. In total, four holes are located on both angular sides of the bearings with a 5 mm diameter to enclose the supporting $M5 \times 0.8$ screws. As it is seen in figure 3.19, holes related to *C* view are bidirectionally located 9 cm away from the face center and holes related to *D* are bidirectionally located 1 cm away from the center.

The most external parts of the Fixing Structure are the press holders. These elements are designed to match with the angular disposition of the toroidal field coils from MEDUSA-CR. As it is seen in figure 3.20, both holders types have, in total, four concentric 5 mm holes for the $M5 \times 0.8$ screws. It is important to highlight that only the longest element has a thread for the used screws to add grip to the opposite hexagonal nuts. Additionally,

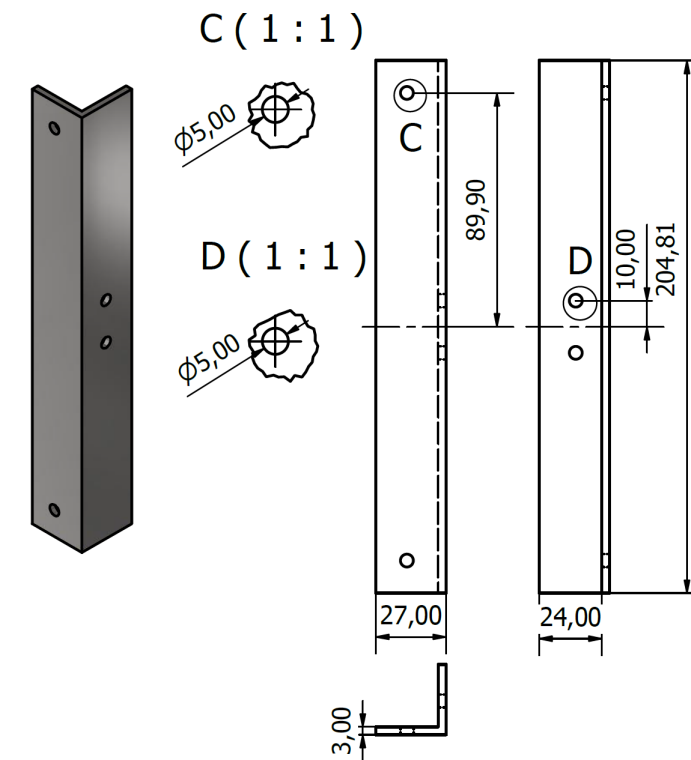


Figure 3.19: L-shaped bearings diagram in millimeters of the Fixing Structure.

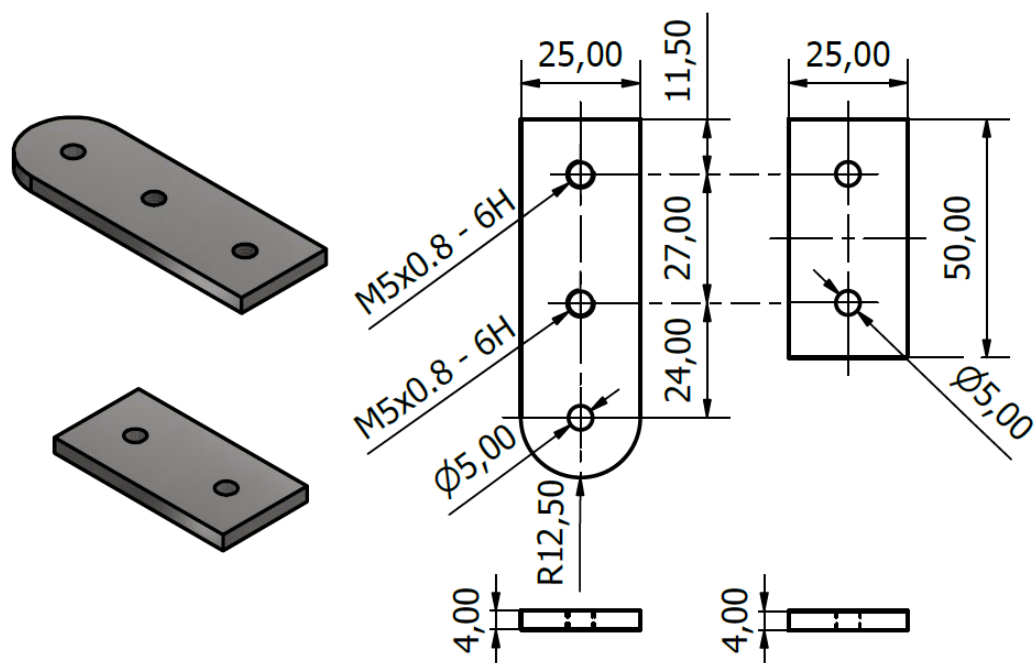


Figure 3.20: Pressing holders diagram in millimeters of the Fixing Structure.

the longest holder, includes a radial end to enable the supporting position of the L-shape bearings in a 40° generated by the nine toroidal field coils locations.

Figures 3.21 and 3.22 show the the complete system of the magnetic diagnostics and their

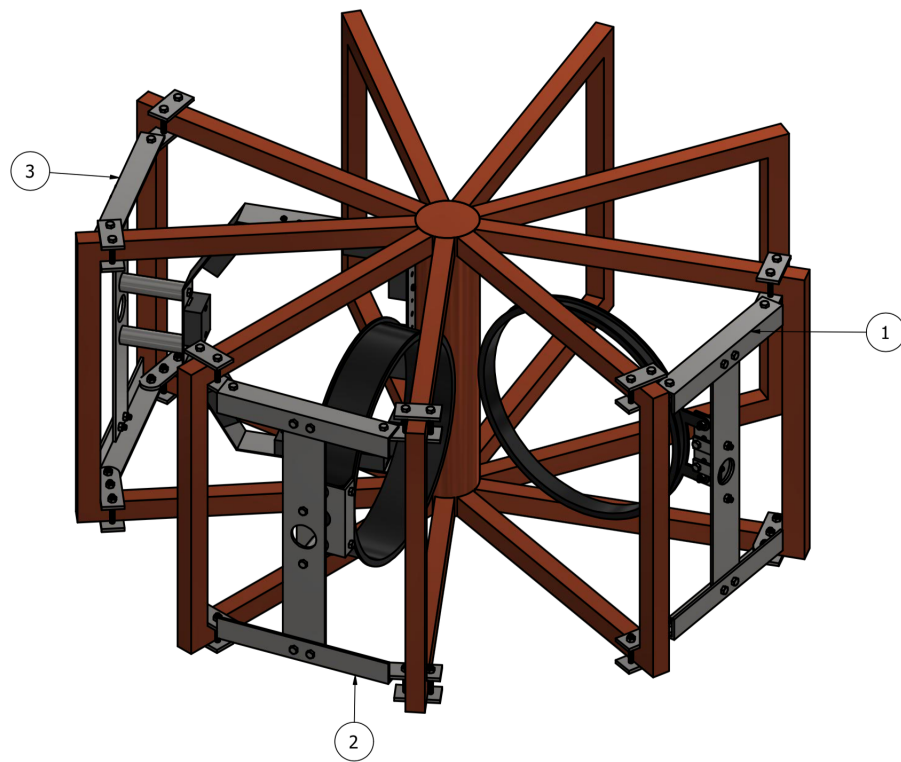


Figure 3.21: Coils system mounted on the toroidal field coils from MEDUSA-CR.

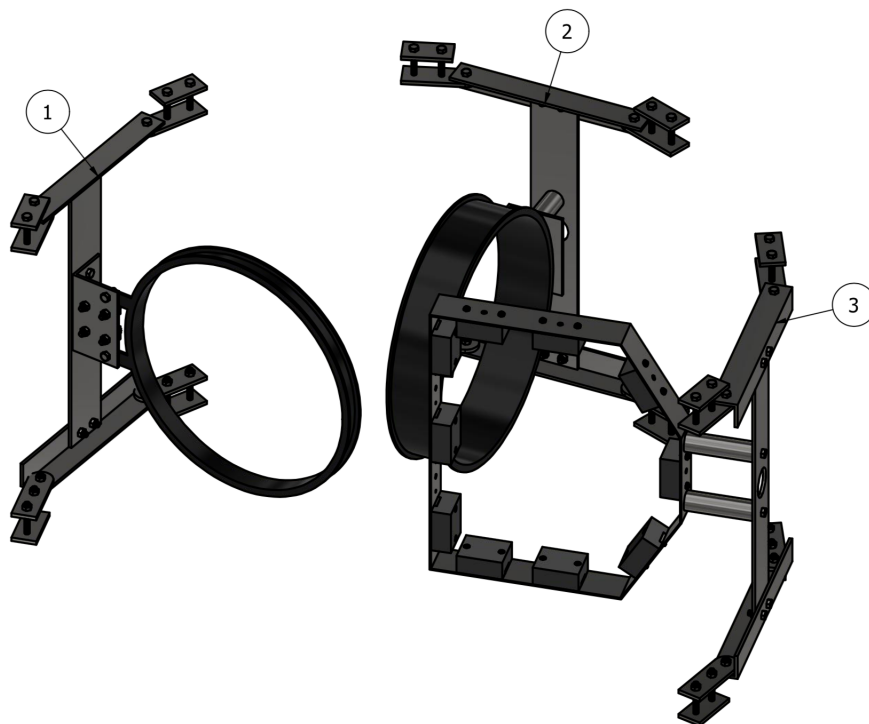


Figure 3.22: Magnetic diagnostics position without the MEDUSA-CR toroidal field coils.

position in MEDUSA-CR tokamak. As it is seen, the Rogowski coil (1), the diamagnetic loop (2) and the Mirnov coils (3) systems are attached to the MEDUSA-CR toroidal field

coils by the same Fixing Structure discussed previously. The arrangement is made based on the distance between each of the diagnostics to operate correctly and while avoiding contact with each other from reactor vibrations produced during each plasma shot.

3.5 Signal Conditioning

3.5.1 Coils Construction

Mirnov Coils

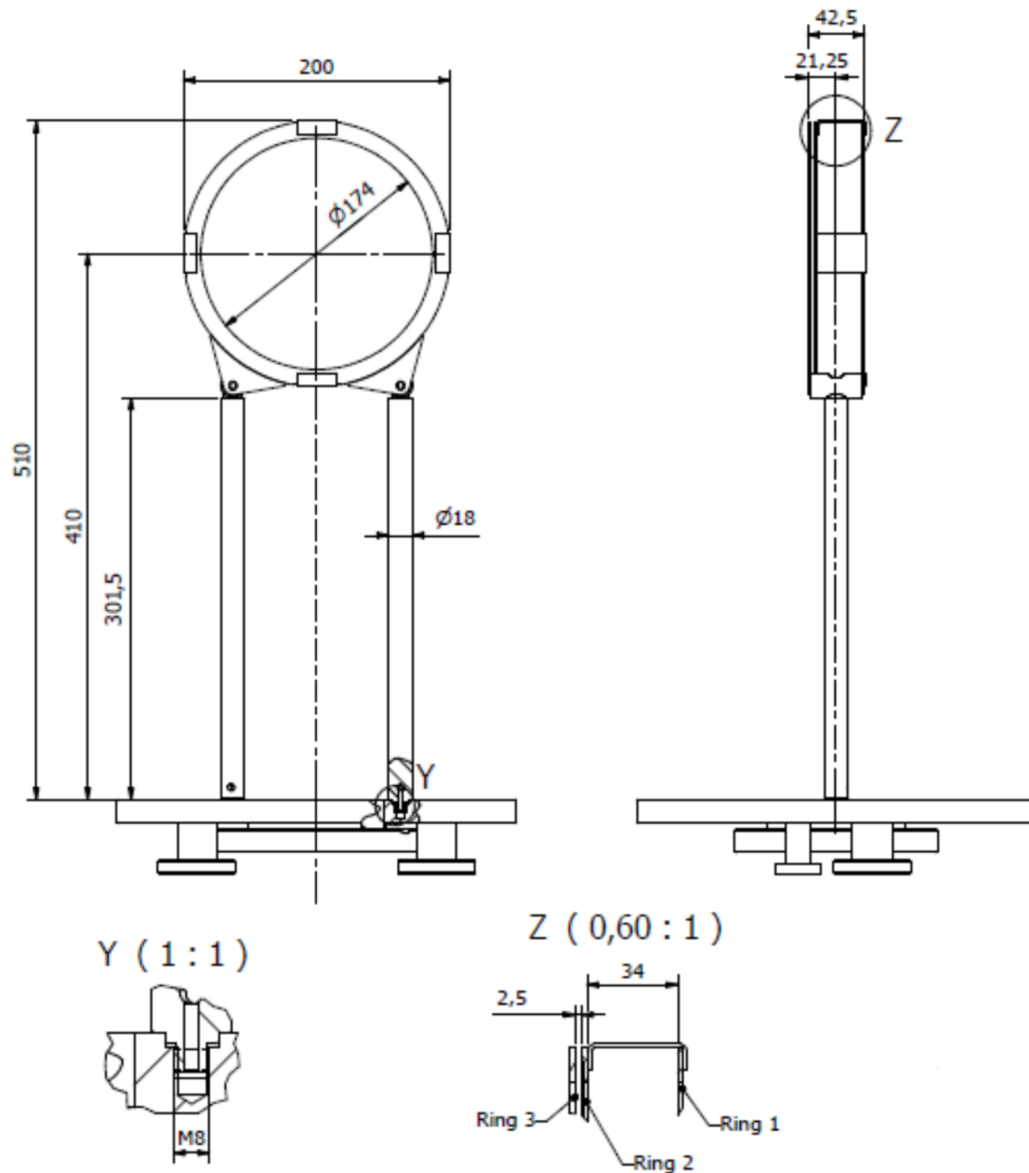


Figure 3.23: Dimensions diagram in millimeters for the set of 16 Mirnov coils installed in GOLEM tokamak [22].

Figure 3.23 shows the blueprints of the fixing structure for the Mirnov set installed in GOLEM tokamak. It is built completely in 316L non-ferromagnetic stainless steel and supports a total of 16 Mirnov coils. Using this assembly, a new set of 16 coils is constructed and then implemented in GOLEM tokamak as a proof of concept for MEDUSA-CR diagnostics design. The process is described later in this section.

Two types of boron-nitride coils are constructed to fit correctly on the assembly shown in figure 3.23. Type A coils are constructed based on dimensions described in figure 3.8 and in table 3.1. On the other hand, parameters of Type B coils are shown in the following table:

Table 3.11: Type B coils parameters.

Parameter	Value (mm)
Coil Length (l)	10
Coil Diameter (D)	12
Core Diameter (D_i)	5.5

Twelve Type B coils and four Type A coils are fixed in the circumference of the ring as it is shown in figure 3.24. The arrangement of these coils, based on their type, is presented in the following table.

Table 3.12: Coils type arrangement.

Coil Number	Type
1	A
2	B
3	B
4	B
5	A
6	B
7	B
8	B
9	B
10	B
11	B
12	B
13	A
14	B
15	A
16	B

Having two types of coils is important to compare the results from the data obtained by the system. However, authors in [28] and [8] describe that construction parameters of

both types, including wire thickness, are suitable for experiments in both MEDUSA-CR and GOLEM.

It is important to highlight that Type A coils are identical to the ones designed for MEDUSA-CR Mirnov system. However, dimensions of these coils can be modified, if necessary, without significant changes on the mechanical support system. Differences in parameters between both types shown in table 3.12 are deeply studied in [22].

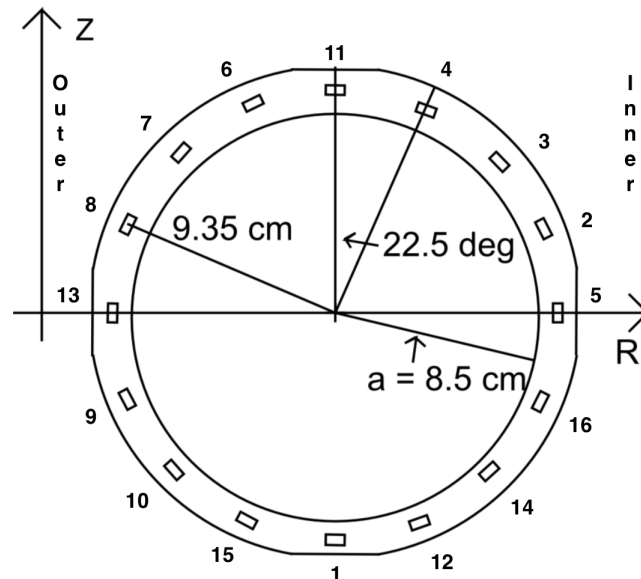


Figure 3.24: Position diagram for the set of 16 Mirnov coils installed in GOLEM tokamak [22].

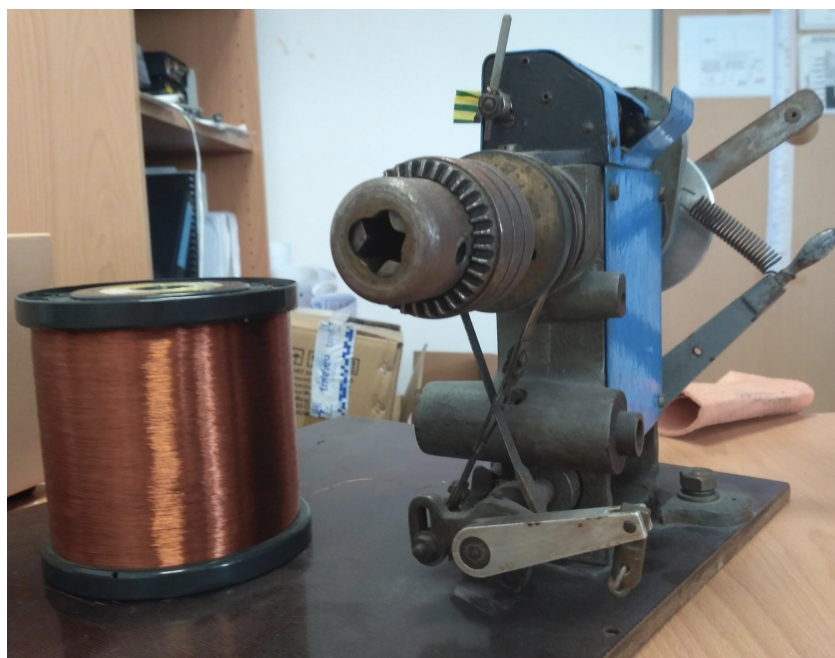


Figure 3.25: Side view of the manual drill used in the winding process of the Mirnov coils.

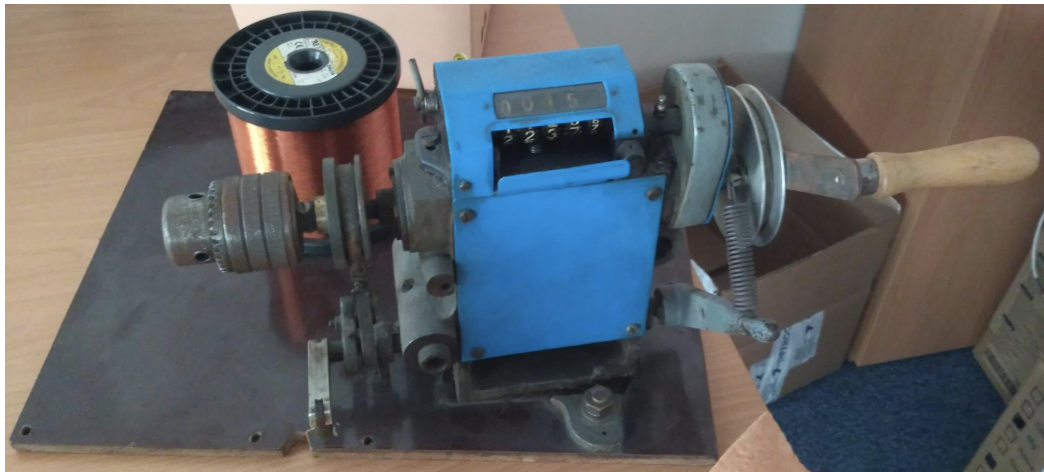


Figure 3.26: Front view of the manual drill used in the winding process of the Mirnov coils.

Before beginning with the construction of the Mirnov coils, all winding tools have to be prepared. As it is shown in figures 3.26 and 3.25 a mechanical drill is used to correctly wind the copper wire to the coils core. It is important to highlight that a turn counter is built in this machine to ease the winding process. Additionally, the total number of turns for each coil is essential for later resistance R and inductance L calculations.

To attach the coils with the drill, an additional part is constructed using a standard screw and three hexagonal nuts, see figure 3.27. This support element has an external diameter of 5 mm, to be fixed inside the coil core, and a length of 40 mm. Additionally, fixation between the hexagonal nuts must be optimal to avoid unwanted displacements of the coil while avoiding any fissure in the boron-nitride core.

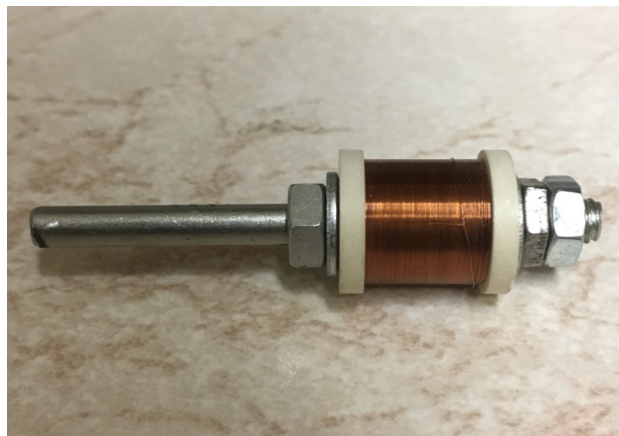


Figure 3.27: Mechanical support for coils fixation.

When the mechanical support for the coils is ready, it has to be fixed in the drill. Figure 3.28 shows the complete system with a constructed coil. As it is seen, an additional length, which depends on the mechanical distance between the coil and its end, of copper wire is left next to the coil to ensure an optimal connection with the feedthrough.



Figure 3.28: Coil and drill system for winding process.



Figure 3.29: Constructed coil with twisted end.

After the coil is wound, the additional end left during the construction process has to be twisted, see figure 3.29. The twisted wire length for each coil is approximately 70 cm and it is based on the mechanical assembly shown in figure 3.23. The entire process of winding and twisting takes approximately 3 hours per coil. For this experiment, a full set of 16 coil are constructed at the precision laboratory of the Czech Institute of Plasma Physics. The final result is shown in figure 3.30.

When the set of Mirnov coils is finished, installation process takes place within the de-

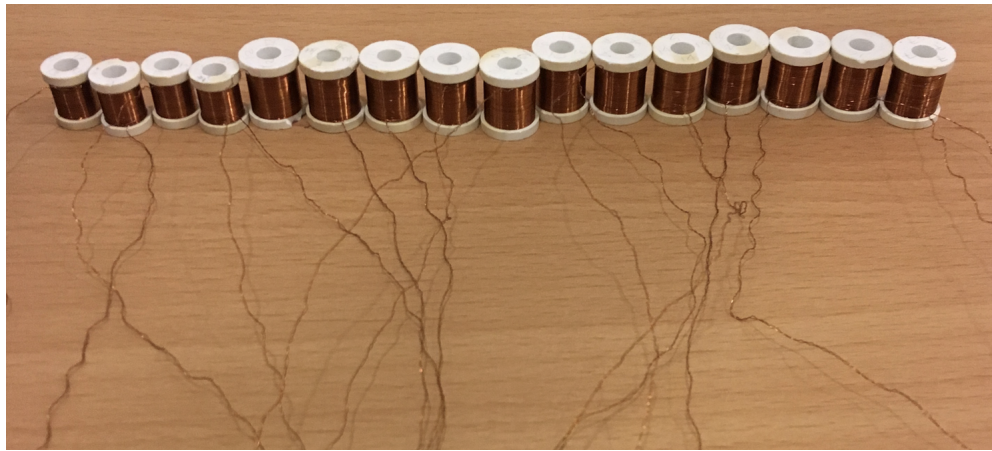


Figure 3.30: Set of 16 Mirnov coils constructed at IPP.



Figure 3.31: Set of 16 Mirnov coils installed in the assembly ring.

signed ring. Each of the coils is attached to the assembly as it is shown in figure 3.31. It is important to notice that wires must be manipulated carefully, otherwise cables could brake and the entire process has to be repeated.

As it is seen in figure 3.32, all the twisted wires are welded to the feedthrough pins. To avoid any contact between each of the cables, that may cause signal noise, two layers of heat-compressible tubes are installed around the ends of each wire. Correct installation of these tubes also produce an optimal adherence between conductor cables and pins.

The completed assembly is shown in figure 3.33. As it is seen, position of each of the constructed coils are related to diagram in figure 3.24. It is important to account that before introducing the diagnostic into the reactor, it should be cleaned for vacuum. Copper

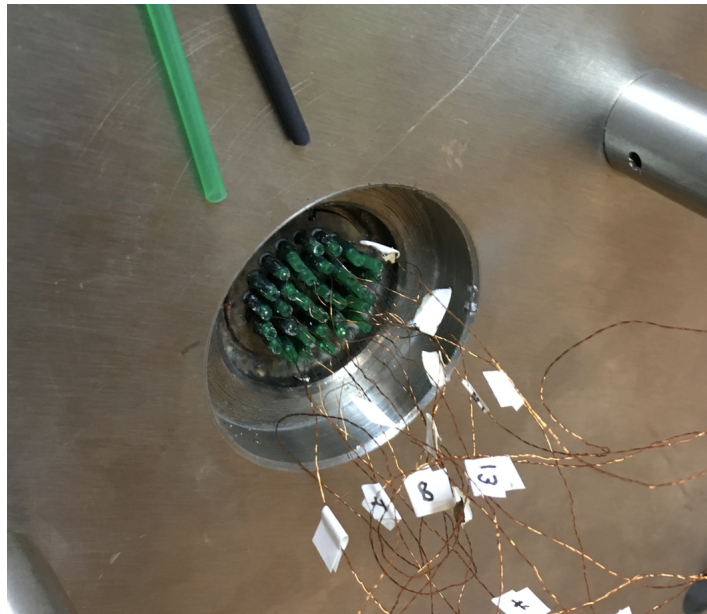


Figure 3.32: Coils welding with the assembly feedthrough.



Figure 3.33: Complete assembly with 16 Mirnov coils installed.

wires, heat-compressible tubes, KaptonTM tape and welding tin used during the construction process are all suited for high temperatures and vacuum applications.

Rogowski Coil

A Rogowski coil is constructed based on the characteristics presented in figure 2.9 and design parameters for the MEDUSA-CR tokamak shown in section 3.3. For this process, the main parameters to take into consideration are the total length $l = 1.2$ m and the core diameter $D_i = 7.29$ mm, see table 3.9.

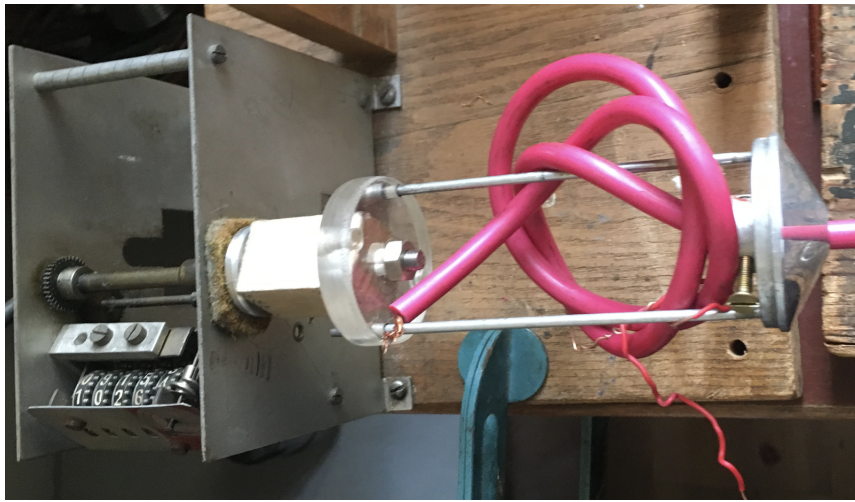


Figure 3.34: Winding drill with turns counter used for the Rogowski coil construction.



Figure 3.35: Free-rotation bearing fixed at the second end of the thicker cable.

Similar to the construction process of the Mirnov coils, tools are prepared before starting winding. Figure 3.34 shows the drill used to attach the thicker cable, which also works as the coil core, used for the Rogowski system. The thicker cable, with a pink color in the figure, has a total length $l = 1.2$ m and both of its ends are fixed to increase winding precision. Figure 3.35 shows the second end of the pink cable fixed to a free-rotation bearing.

After the pink cable is attached in both ends, winding process is executed. The copper insulated wire ($d = 0.25$ mm) is rolled around the pink cable using the manual drill. Figure 3.36 shows how the Rogowski coil is constructed. The thinner copper wire winding should fit the AWG-16 cable as much as possible around its entire length l to optimize U_{sig} [28].

When the Rogowski coil is ready, it has to be protected from external exposure that



Figure 3.36: Half wound Rogowski coil using a $d = 0.25$ mm copper wire.



Figure 3.37: Rogowski coil with electric tape wrapping.

could cause wire displacements. Figure 3.37 shows how the complete coil is wrapped with electrical tape. However, electrical tape is not suited for vacuum and high-temperature applications. Instead, it is recommended to use KaptonTM tape for MEDUSA-CR coil.

The final step of coil construction is to weld both ends of the wires to close the loop, as shown in figure 2.9. Figure 3.38 presents the thinner copper wire with $d = 0.25$ mm welded to the inner conductor of the AWG-16 cable. The entire coil should then be attached to the the main support ring of the Rogowski mechanical system, see figure 3.13.



Figure 3.38: Welded ends of the Rogowski coil.

3.5.2 Coils Calibration

Mirnov Coils

Calibration is made with a custom-designed coil connected in a LC circuit. Capacitors are then charged with 220 V and switched on to create a specific oscillating signal. Design parameters of this custom inductor are shown in the following table.

Table 3.13: Calibration coil parameters.

Parameter	Value
Inductance (L)	25.48 μH
Number of Turns (n)	30
Number of Layers (N_l)	2
Coil Length (l)	6 cm
Core Diameter (D_i)	4 cm
Wire Diameter (d)	2.2 mm

Calibration coil shown in figure 3.39 is designed to maintain a constant magnetic field in its geometrical center. Its 30 turns are distributed in non-uniform winding around the plastic core. The first layer N_l has 24 turns and the second layer contains the remaining 6 turns, with a distribution of 2 turns tightly located on each end.

Magnetic field distribution and density on the length of the calibration coil is shown in figure 3.40. The highest magnetic field density is located on the ends of the coil, where the number of turns is maximized. On the other hand, this winding configuration produces a flat-top distribution with a quasi-constant 0.304 mT field in the central region of the

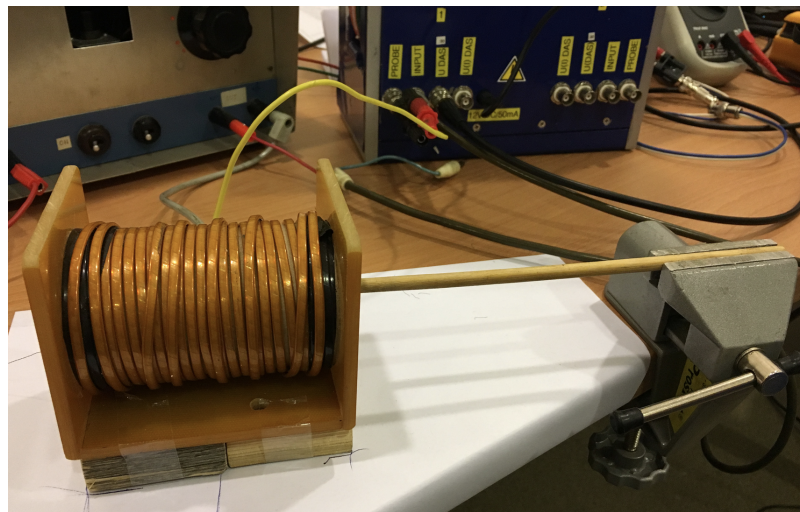


Figure 3.39: Calibration coil connected to a LC circuit.

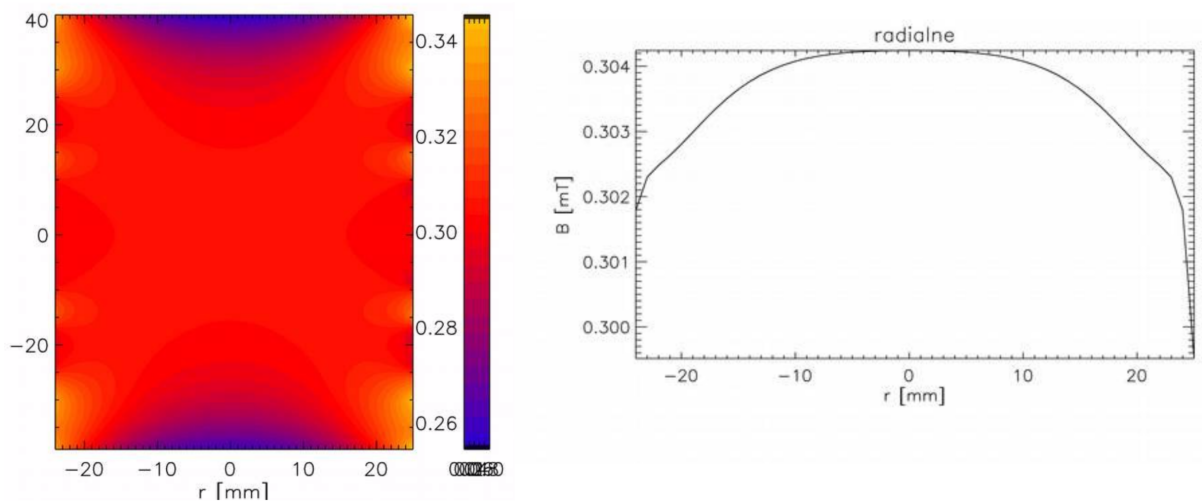


Figure 3.40: Magnetic field simulation of the calibration coil [29].

calibration coil. This flat-top distribution is important to set a reference during the calibration of each Mirnov coil [29].

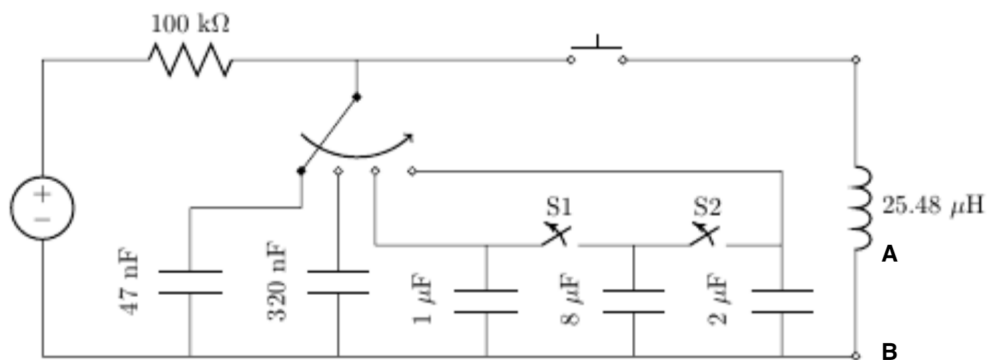


Figure 3.41: Connection diagram of the calibration coil with the LC circuit [29].

The calibration coil is connected to the LC circuit as it is shown in figure 3.41. By switching between the capacitance values, different discharge frequencies are obtained. The following table shows the frequency configurations related to the capacitance values.

Table 3.14: Frequency configuration with different capacitance values.

Nominal Capacitance (nF)	Frequency (kHz)
11000	9.4
10000	9.9
9000	10.4
2000	21.4
1000	30.7
320	52.8
47	143.9

For calibration, each of the Mirnov coils is introduced inside the core tube of the calibration coil in a centered position, as shown in figure 3.43. Capacitors are then discharged to generate different magnetic field frequencies. Points A and B, in figure 3.41 are connected directly to a current measuring device and its output signal is then plugged to the oscilloscope. Output voltage U_{sig} from each Mirnov coil is connected to the other channel of the oscilloscope for signal comparison.

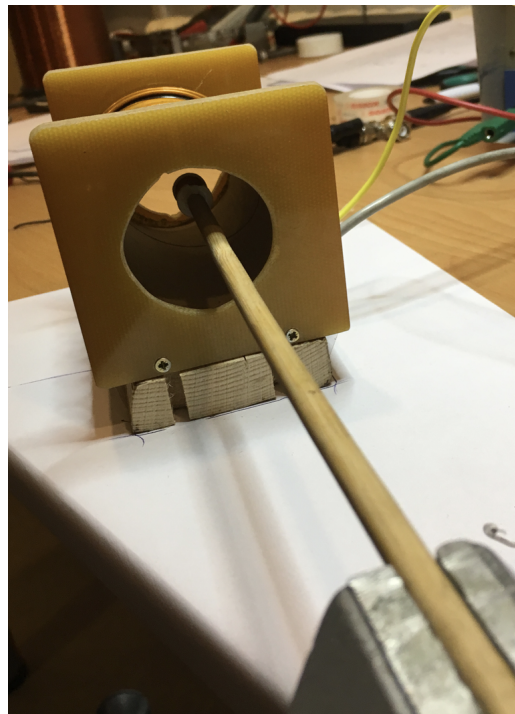


Figure 3.42: Mirnov coil position inside the calibration coil.

When capacitor discharge is done, two signals are received in the oscilloscope. Channel A input current from the LC circuit and channel B input U_{sig} from the Mirnov coil. As

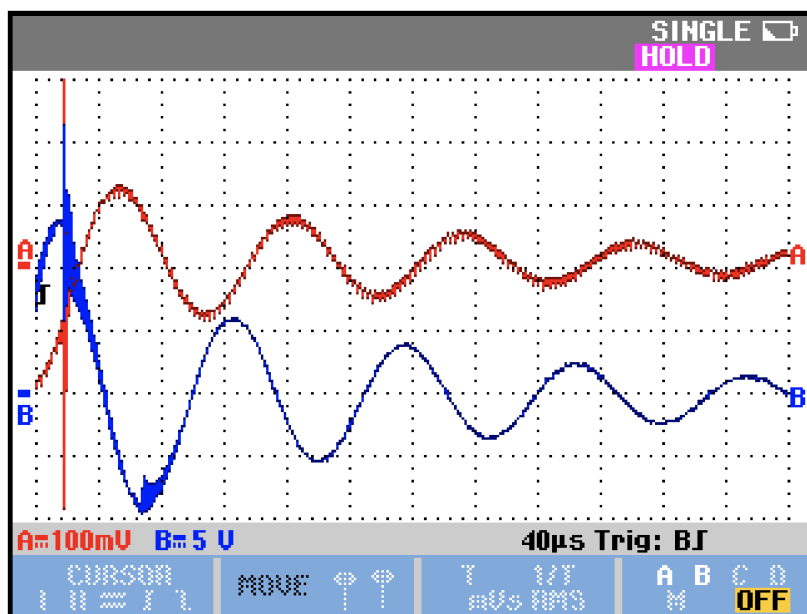


Figure 3.43: Oscilloscope input signals for 11000 nF nominal capacitance.

it is shown in figure 3.43 both signals have the same frequency but different phases. It is important to notice that signal A is scaled to 5 V/A, so in this case, its amplitude is equivalent to 20 mA.

However, calibration is not finished yet. Data obtained from the oscilloscope is analyzed and reconstructed to calculate the correct linear relationship between U_{sig} and calibration coil current.

Using data from the oscilloscope inputs, the initial noise is erased by code. However, as it is seen in figure 3.43, current signal needs to be amplified before comparing it with the Mirnov coil signal U_{sig} . Figure 3.44 shows the result of the processed data. As it is noticed, phases between both signals are still different. So, using a time displacement of the current plot, the problem is fixed. The result of phase correction is shown in figure 3.45.

Now that the signals can be compared with a similar amplitude and phase, the linear relationship between both is calculated. As it is seen in figure 3.46, the data from both signals is plotted in the same graph. Based on the relationship, the tendency equation is calculated automatically as:

$$U_{sig} = 260I - 0.48 \quad (3.14)$$

Let the Ampere Law describe the magnetic field B in the center of the calibration coil as:

$$B = \mu \frac{n}{l} I \quad (3.15)$$

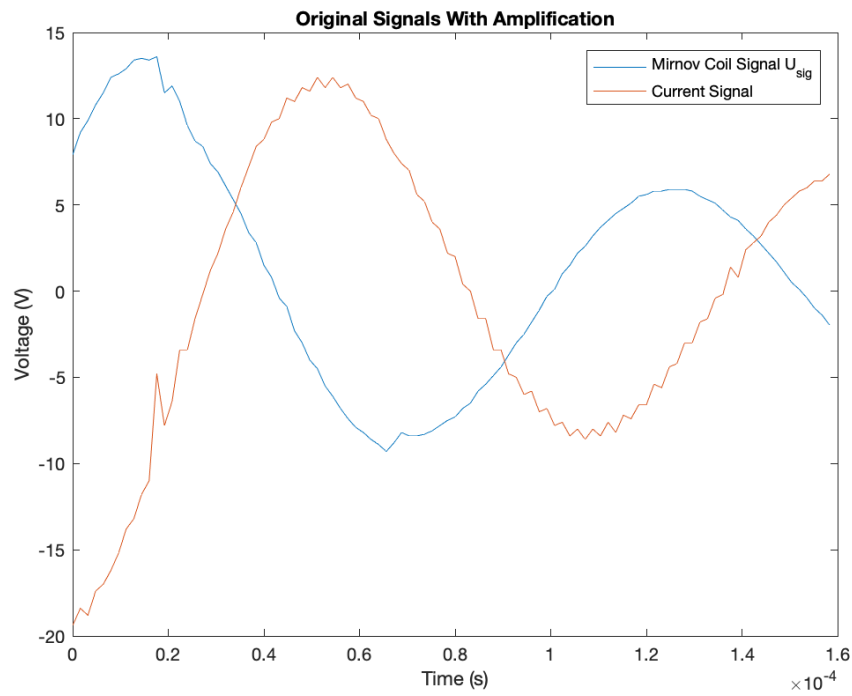


Figure 3.44: Amplified signals obtained from oscilloscope data.

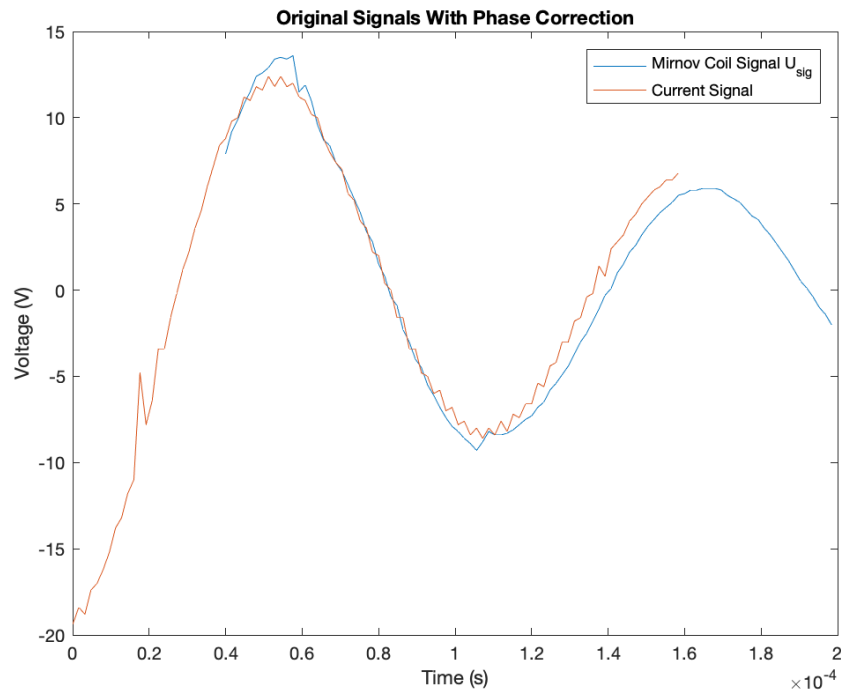


Figure 3.45: Amplified signals with phase correction.

So, substituting 3.15 in 3.14, the following relationship between U_{sig} and B is calculated:

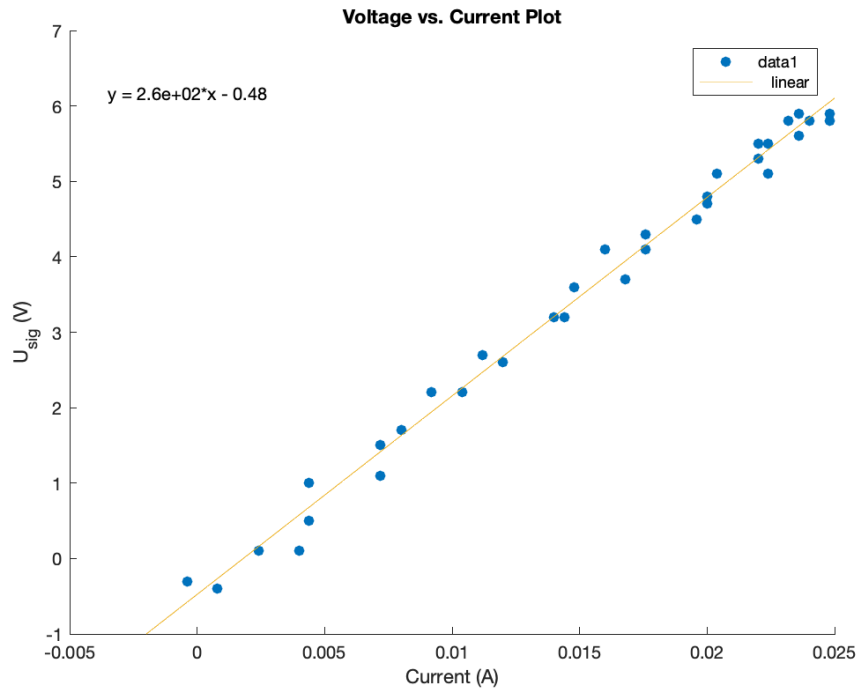


Figure 3.46: Linear relationship between the Mirnov coil signal U_{sig} and calibration coil current.

$$U_{sig} = 260 \frac{l}{\mu n} B - 0.48 \quad (3.16)$$

It is important to highlight that values for n , l and μ are constants related to the calibration coil and shown in table 3.13. Parameters calculated during construction and calibration of each Mirnov coil are discussed later in chapter 4. Source code to calculate figures 3.44, 3.45 and 3.46 is shown in appendix A.4. Notice that the attached program is made for Mirnov coil 1, Type A (see table 3.12), NC=320 nF and a low pass filter is applied to the current signal.

3.5.3 Signal Integration

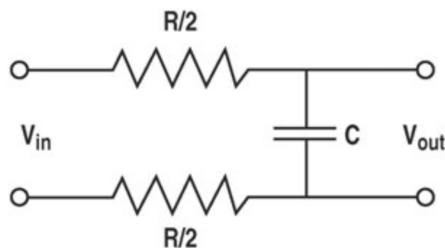


Figure 3.47: Passive integration circuit [10].

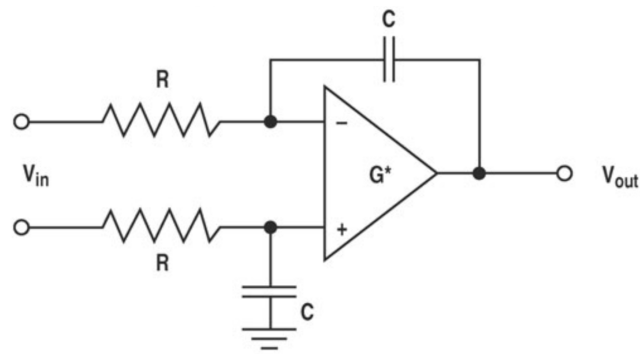


Figure 3.48: Active integration circuit [10].

Signal integration is critical for the correct operation of magnetic diagnostics in tokamaks and it can be done using circuits or programming, depending on the application. Figure 3.47 represents a passive integration circuit and figure 3.48 represents an active integration circuit where V_{in} is equivalent to U_{sig} and V_{out} is equivalent to U_{out} . Additionally, G^* symbolizes the gain of the amplifier G . Authors in [10] and [30] explain how to design and implement this physical integration circuits.

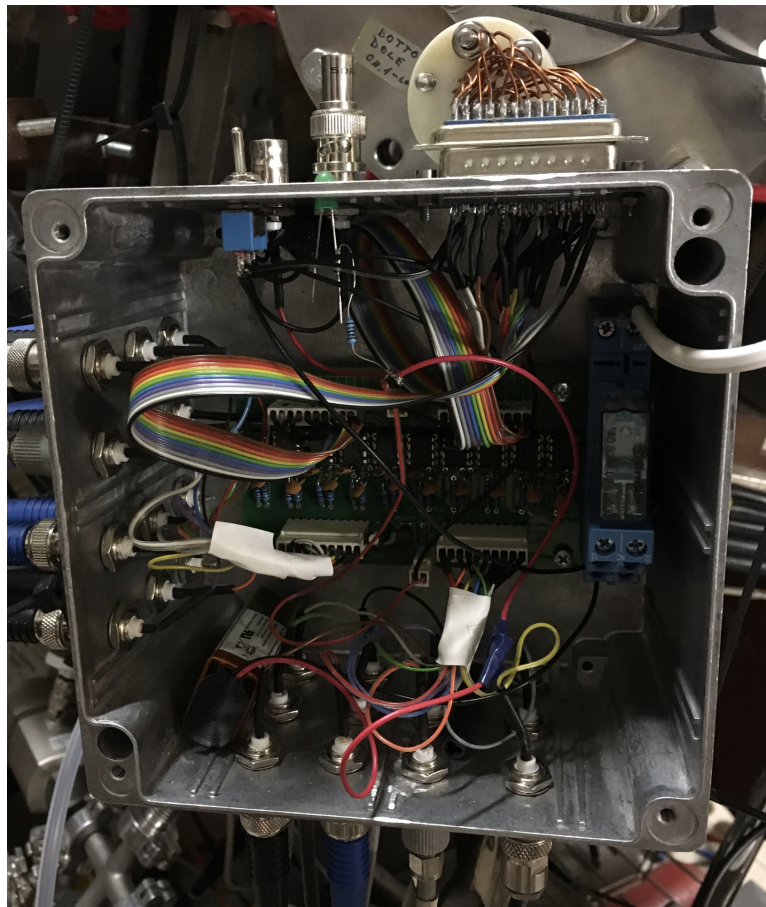


Figure 3.49: Physical integration circuit installed in GOLEM for 6 temperature probes.

In the case of Mirnov coils, diamagnetic loop and Rogowski coil, references in [28] and [8] recommend to integrate the signals numerically. To obtain the correct quantities of B

or I in a given time t , U_{sig} has to be detected for the entire duration of a plasma shot. For this, a physical integration circuit may accumulate errors in U_{sig} such as DC offsets, electromagnetic noise, missing data, failing trigger, need of extra space and even increased costs. Figure 3.49 illustrates the drawbacks of installing a physical integration circuit in a tokamak.

For the magnetic diagnostics in MEDUSA-CR a numerical integration method is designed and tested at GOLEM tokamak. After installing the Mirnov set, discussed in 3.5.1, data is acquired from each of the 16 coils individually. In this analysis, data from a good plasma discharge is required, so GOLEM shot No. 29293 [2] is chosen as a reference, see figure 3.50.

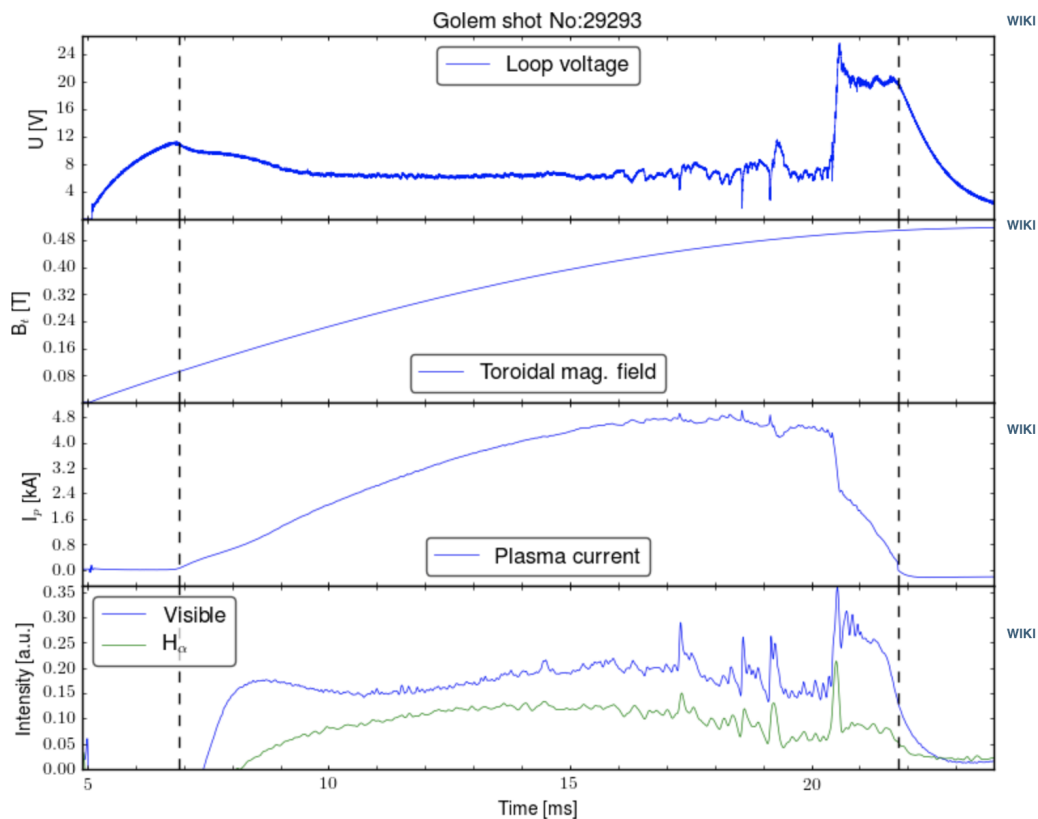


Figure 3.50: Plasma shot No. 29293 in GOLEM tokamak [2].

In figure 3.50, loop voltage indicates a plasma life of approximately 15 ms and a maximum current of 4.8 kA . Additionally, there is a double breakdown and some instabilities during plasma generation. These characteristics affect plasma position that can be analyzed with the Mirnov coils.

Raw data obtained from Mirnov coil No. 11 is shown in figure 3.51. Values from plotted data are equivalent to zero before and after plasma discharge. Data is then integrated to calculate the local magnetic fluctuations of plasma B_0 , see figure 3.52.

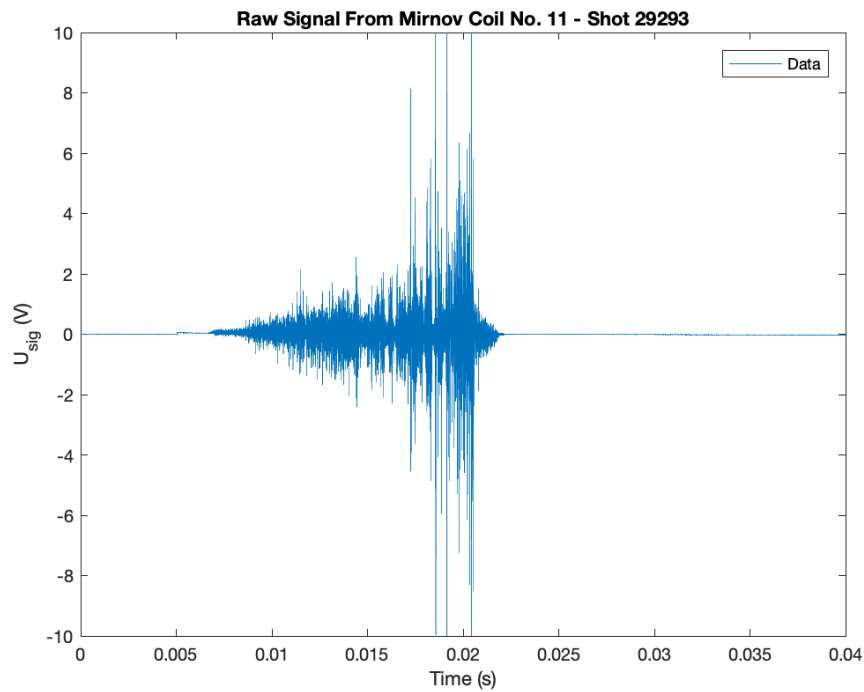


Figure 3.51: Raw data from Mirnov coil No. 11, Type B.

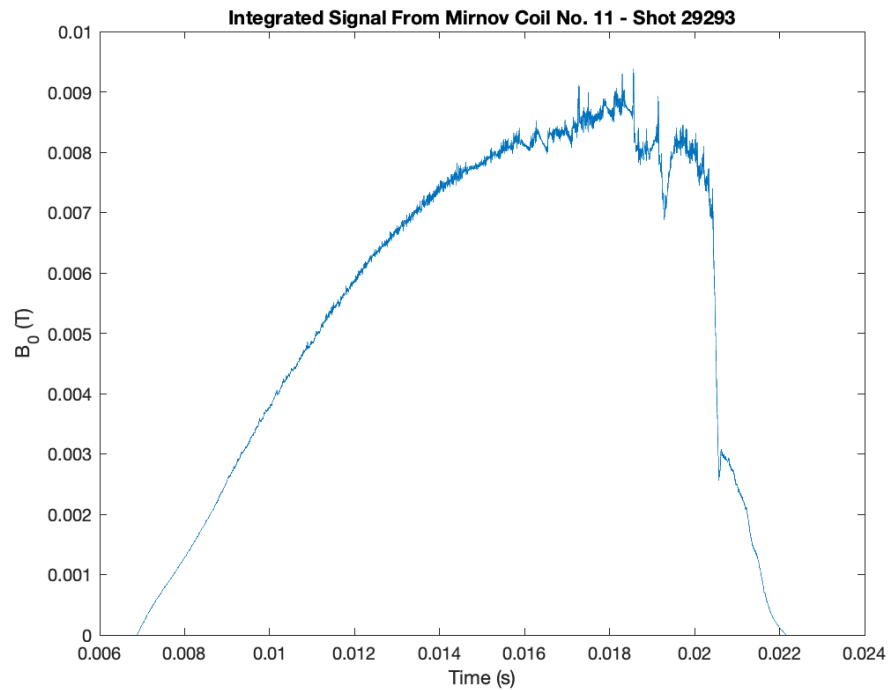


Figure 3.52: Integrated data from Mirnov coil No. 11, Type B.

Signal Integration Code Using Matlab

```
1 Mc = csvread('j11.csv');
```

```

2 A2c=Mc(:,end);
3 t=Mc(:,1);
4
5 %Cutting data in presence of plasma:
6 coil=A2c(6883:22150);
7
8 %Time lapse is also cut in the same range:
9 tp=t(6883:22150);
10
11 %Substracting the drift:
12 Mcoil=mean(coil);
13 Dcoil=coil-Mcoil;
14
15 %Data integration:
16 intCoil=cumsum(Dcoil);
17
18 %Dividing integrated data by the coefficient:
19 coeff = 32.3*1000;
20 Fint=intCoil/(coeff);

```

Listing 3.1: Source: IntegrationM11.m

Segment of the code used to generate graphs in figures 3.51 and 3.52 is listed above. As it is shown, raw data obtained from coil No.11 is stored in a file called *j11.csv*. This file is composed of two columns, the first one has the values of time samples and the second one has the values of U_{sig} . Both columns are stored in t and $A2c$ arrays respectively.

Lines 5 to 9 show that the data is cut in the values in which the plasma discharge is present. The selection of these values are made manually, by first graphing the entire sample of information. The mean value of the U_{sig} data is then calculated and subtracted to each of the original array elements, eliminating the signal offset. Integration is finally done by calculating the cumulative sum $cumsum()$ of the resulting subtracted values. However, the process is not finished since integration is calculated without taking into consideration relationship in 3.7. The coefficient $coeff$ in this equation is calculated theoretically and is related to the coils design parameters of D , d , f and N_l .

So, integration of the expression in 3.7 results in the following.

$$B_0 = \frac{1}{32.3 \times 10^3} \int U_{sig} \quad (3.17)$$

Relationship in 3.17 is programmed in lines 19 and 20 of the code listed above and its result is graphed in figure 3.52. Further comparison of signal integration is found in chapter 4. It is important to highlight that processes are analogue in the case of signal integration from the Rogowski coil and the diamagnetic loop. However, relationship described in 3.17 should be calculated for 3.12 and 3.13 respectively for Rogowski coil and diamagnetic loop.

The complete code used to integrate the signals is attached in appendix A.5.

3.6 Data Acquisition System

Data acquisition system (DAS) in MEDUSA-CR is based on the diagnostics with the higher response frequency f_{res} : the Mirnov coils. As it is discussed in section 3.1.2 and in reference [19], magnetic measurements in MEDUSA-CR are observed in a frequency around 75 kHz. However, as it is shown in 3.6, each of the coils are designed with a response frequency f_{res} of 690 kHz.

Higher frequencies phenomena are not common in small machines as GOLEM or MEDUSA-CR [28]. So, data acquisition systems for increased sampling rates could unnecessarily elevate costs.

The maximum resolvable frequency f_{max} for signals from MEDUSA-CR magnetic diagnostics is determined to be 500 kHz, leaving a safety factor for future high frequency measurements.

Calculating the sampling frequency for $f_{max} = 500$ kHz:

$$f_{max} = f_{Nyquist} = 500kHz = \frac{f_{sampling}}{2} \quad (3.18)$$

Based on the relationship above, $f_{sampling} = 1$ MHz for the data acquisition system. Now, in a typical MEDUSAR-CR plasma discharge of $t_p = 3$ ms [19], a relationship between the sampling period $T_{sampling}$ and t_p can be calculated.

$$T_{sampling} = \frac{1}{1MHz} = 1\mu s < t_p \quad (3.19)$$

Which gives a time difference in the order of 10^3 , suitable for measurements in MEDUSA-CR.

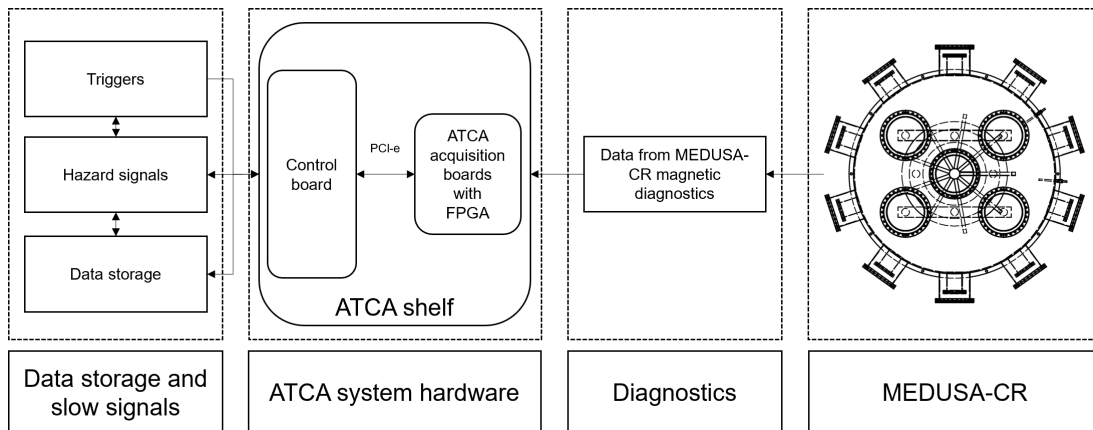


Figure 3.53: Data Acquisition diagram for MEDUSA-CR.

In order to obtain data from alternate discharges, the chosen system is based on the Advanced Telecommunications Computing Architecture (ATCA) standard. The main advantage of ATCA standard for fusion devices is the improved *Reliability, Availability and Serviceability* (RAS) characteristics. Additionally, for machines like MEDUSA-CR, author in [7] recommends programming a real-time control system over a MART-e framework with a 100 μ s control cycle.

As it is seen in figure 3.53, the MEDUSA-CR actuators, as toroidal field power supply and gas puffing, can be connected to ATCA control system in addition to the magnetic diagnostics. Furthermore, the main aim of this system is to enable information gathering from different real-time diagnostics that will be installed in MEDUSA-CR.

Regarding the database communication with the control system, author in [7] also recommends installing a driver to pool variables set at the end of each discharge from control system. When the discharge is complete, the database accesses the data stored on the real-time system. This data includes raw data from the diagnostics, as shown in figure 3.51, observed plasma parameters, obtained from numerical integration as in 3.5.3, and values sent to the actuators.

Compatible ATCA data acquisition systems are specified by the PICMG (PCI Industrial Computer Manufacturers Group) and specification 3.x is selected for future DAS developments in MEDUSA-CR. Family requirements related to PICMG 3.x are listed as follows [1].

1. **PICMG 3.0** is the overall general specification that defines mechanics, board dimensions, power and data connectors, power distribution, and system management.
2. **PICMG 3.1** defines an Ethernet switch fabric over the generic backplane fabric interconnect up to 10 Gbit/s per link.
3. **PICMG 3.2** defines how InfiniBandTM systems are built within the architecture and will specify, link physical layers, protocols, and protocol mappings.
4. **PICMG 3.3** defines a StarFabricTM implementation over the backplane providing TDM, cell, control, and packet connectivity over the same fabric.

Chapter 4

Results and Analysis

4.1 Mechanical Design

The mechanical system of each diagnostic is designed to operate under vacuum and high temperature conditions. Materials chosen for their construction, which are commonly used for fusion applications, are mentioned in chapter 3 and listed in appendix A.6.

A complete structural analysis of the critical mechanical parts is executed using a CAD simulation tool. As it is shown in subsection 3.4, the Fixing Structure, which is the critical system, attaches the diagnostics with the toroidal field coils of MEDUSA-CR. Material properties of 316L stainless steel are shown in the following table.

Table 4.1: Material properties for 316L stainless steel, used in the Fixing Structure [26].

Property	Value
Mass Density	8 g/cm ³
Yield Strength	228 MPa
Ultimate Tensile Strength	540 MPa
Young's Modulus	190.3 GPa
Poisson's Ratio	0.305
Shear Modulus	72.9 GPa

Table 4.2: Total mass of the magnetic diagnostics, excluding the Diagnostics Fixing Structure.

Diagnostic	Mass (kg)
Mirnov Coils System	3.51
Diamagnetic Loop System	2.40
Rogowski Coil System	2.10

As it is shown in table 4.2, the critical mass value is given by the Minov coils system with

3.51 kg, which is equivalent to 34.34 N. However, adding a conservative margin of 14 N to anticipate any other element added during construction process, the total input force used for simulation is 48 N.

Table 4.3: Input mesh parameters for stress analysis.

Description	Parameter
Average element size	0.020 mm
Minimum element size	0.010 mm
Maximum turn angle	60°
Grading factor	1.5

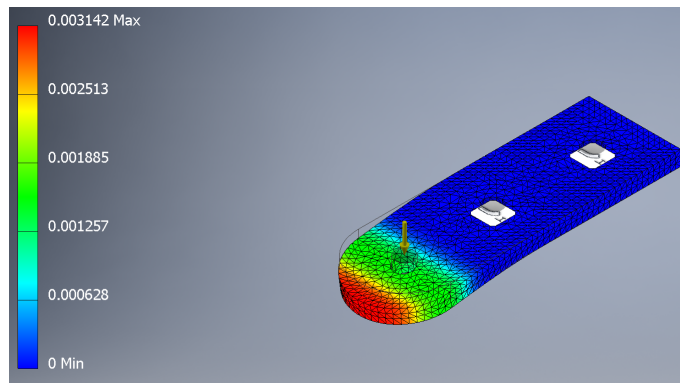


Figure 4.1: Mechanical displacement simulation for the lower pressing holder of the Fixing Structure, in 316L stainless steel.

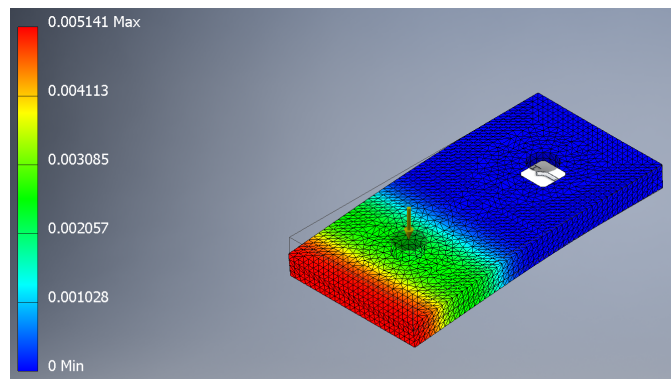


Figure 4.2: Mechanical displacement simulation for the upper pressing holder of the Fixing Structure, in 316L stainless steel.

A structural finite element study is then performed for each mechanical part of the diagnostics Fixing Structure in 3.4. The analysis takes into consideration parameters from tables 4.1, 4.2 and overall dimensions of each part. Additionally, simulations are individually run with the same input mesh parameters in table 4.3 to generate a displacement convergence value of $X_{conv} > 99\%$.

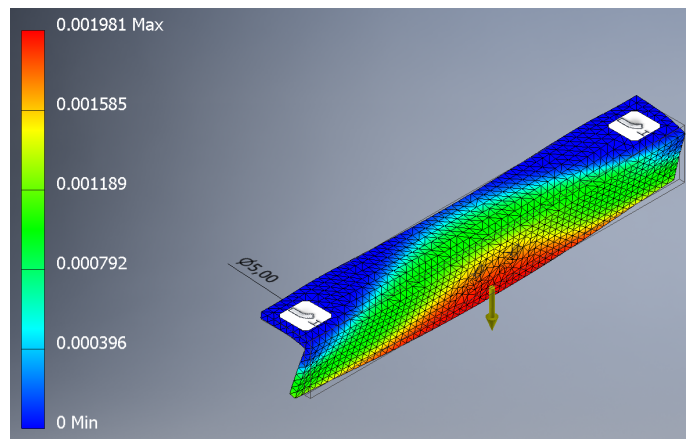


Figure 4.3: Mechanical displacement simulation for the L-shaped bearings of the Fixing Structure, in 316L stainless steel.

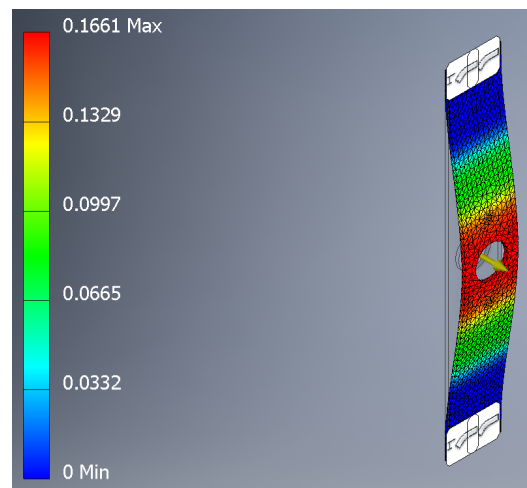


Figure 4.4: Mechanical displacement simulation for the central bar of the Fixing Structure, in 316L stainless steel.

Figures 4.1 to 4.4 show the result of CAD finite elements simulations for each part due to force application. Color red indicates the maximum shift and color blue indicates the minimum. For each element of the Fixing Structure, force is applied on stress acting points related to weight distribution of the Mirnov set. On the other hand, fixed positions are selected based joint supports with the other assembly components.

Table 4.4 lists calculated values for Von Mises Stress, total mechanical displacement and safety factor for the studied parts. Comparing the results from all tests, a maximum displacement of 0.16 mm in the force application direction is obtained in the central bar. Additionally, a minimum safety factor of 6.56 is also obtained in the same element.

Table 4.5 is generated based stress analysis results of the studied components. As it is seen, $X_{conv} > 99\%$ for all the mechanical parts. Additionally, the amount of mesh nodes and elements produced during simulation is related to input parameters shown in table 4.3, used material shown in table 4.1 and overall dimensions shown in appendix A.6.

Table 4.4: Results for the finite elements analysis of the Fixing Structure.

Name	Min. Value	Max. Value
Lower pressing holder:		
Von Mises Stress	0.0005 MPa	9.61 MPa
Displacement	0.00 mm	0.0031 mm
Safety Factor	6.65	15.00
Upper pressing holder:		
Von Mises Stress	0.0014 MPa	14.53 MPa
Displacement	0.00 mm	0.0051 mm
Safety Factor	8.10	15.00
L-shaped bearings:		
Von Mises Stress	0.0087 MPa	8.8300 MPa
Displacement	0.00 mm	0.0019 mm
Safety Factor	9.00	15.00
Central bar:		
Von Mises Stress	0.081 MPa	35.30 MPa
Displacement	0.00 mm	0.166 mm
Safety Factor	6.56	15.00

Table 4.5: Convergence results for the finite elements analysis of the Fixing Structure.

Description	Value
Lower pressing holder:	
Mesh nodes	26273
Mesh elements	16397
Convergence (X_{conv})	99.82%
Upper pressing holder:	
Mesh nodes	49266
Mesh elements	32213
Convergence (X_{conv})	99.98%
L-shaped bearings:	
Mesh nodes	15455
Mesh elements	8581
Convergence (X_{conv})	99.36%
Central bar:	
Mesh nodes	16033
Mesh elements	9175
Convergence (X_{conv})	99.44%

4.2 Coils Construction

Coils parameters vary depending on the construction process. As it is discussed in section 3.5.1, two types of Mirnov coils are constructed to be installed in tokamak GOLEM. However, mechanical dimensions and electrical parameters designed for the MEDUSA-CR Mirnov system are equivalent to Type A, see table 3.1.

Table 4.6: Expected results for the Mirnov coils Type B parameters.

Parameter	Value
Inductance (L)	140.2 μH
Resistance (R)	14.0 Ω
Turns per layer (n)	100
Effective Area (A_{eff})	165.1 cm^2

To be able of comparing the obtained results from all the coils during the construction process, a reference of the expected parameters for Type B coils are calculated and presented in 4.6 and 3.11. Although values change compared with Type A coils, both coils can be used for measurements in MEDUSA-CR, see section 3.5.1.

Table 4.7: Measured parameters for Mirnov coils after construction.

Coil No.	R (Ω)	L (μH)	n_{l1}	n_{l2}	L_{err} (%)	R_{err} (%)
1	10.1	99.6	63	65	6.21	14.6
2	14.3	181.1	83	80	29.17	2.14
3	14.4	187.5	83	80	33.73	2.85
4	13.9	176.6	79	77	25.9	0.71
5	10.9	96.7	66	65	8.94	23.72
6	14.6	184.4	81	82	31.52	4.28
7	14.6	186.6	82	83	33.09	4.28
8	14.2	176.2	83	82	25.67	1.42
9	14.6	189.2	81	80	34.95	4.28
10	14.9	190.1	81	83	35.59	6.42
11	14.4	183.6	82	83	30.95	2.85
12	14.6	188.6	83	81	34.52	4.28
13	9.4	87.9	60	65	17.23	6.69
14	15.7	189.7	82	79	35.30	12.14
15	9.5	96.3	65	65	9.33	7.82
16	16.3	190.5	75	78	35.87	16.42

Table 4.7 lists the measured values of each coil after the construction process. As it is seen, resistance R for Type A coils, (1, 5, 13, 15) in table 3.12, has an average of 9.975 Ω and R for Type B coils has an average of 14.70 Ω . Inductance average for Type A coils is 95.125 μH and for Type B is 185.34 μH , measured with a 400 kHz frequency. Furthermore, the

average amount of turns, per layer, for Type A coils is 64.25 and for Type B is 80.95, which is related to the performance of other measurements. Error percentages for inductance and resistance values are calculated in the last two columns of the table.

Table 4.8: Measured parameters for Rogowski coil after construction.

\mathbf{R} (Ω)	\mathbf{L} (mH)	n_{l1}	L_{err} (%)	R_{err} (%)
49.2	1.0059	4510	33.33	18.27

Additionally, table 4.8 shows the measured results for the Rogowski coil constructed. As it is seen in tables 4.7 and 4.8, in both cases the error percentages related to inductance L_{err} are greater than the errors calculated to resistance R_{err} .

4.3 Calibration

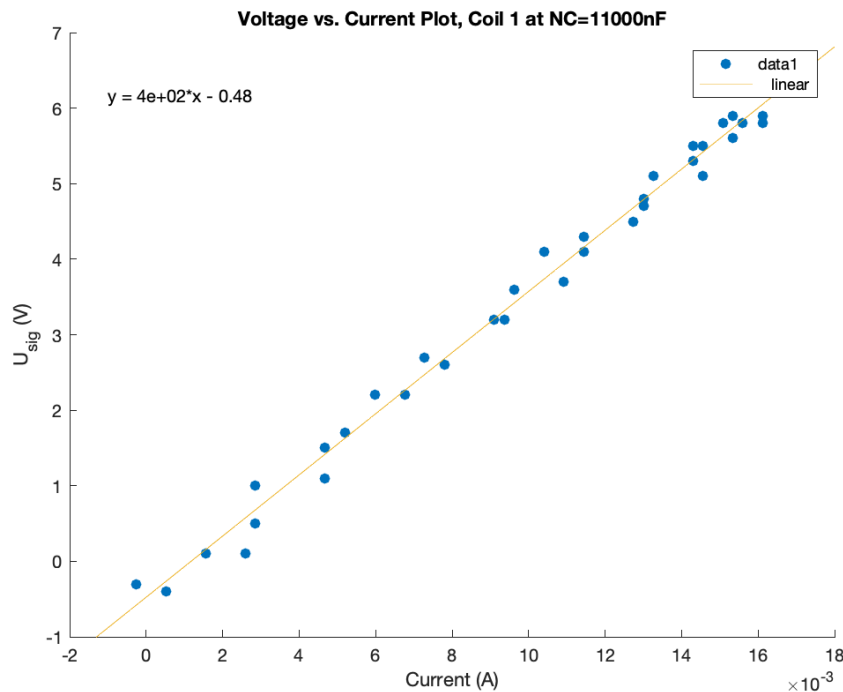


Figure 4.5: U_{sig} vs. Current graph from the calibration of coil No. 1 with 11000 nF.

Calibration results are presented for coils Type A in nominal capacitances of 11000 nF. As it is explained in section 3.5.2, U_{sig} from the Mirnov coil is plotted against current from the calibration coil. The amount of plotted data is related to the signal cut range for noise reduction, phase correction and amplification.

Then, the best fitting linear equation is calculated, as it is shown in figures from 4.5 to 4.8. Values from the calibration coil, see table 3.13, are substituted in the generated

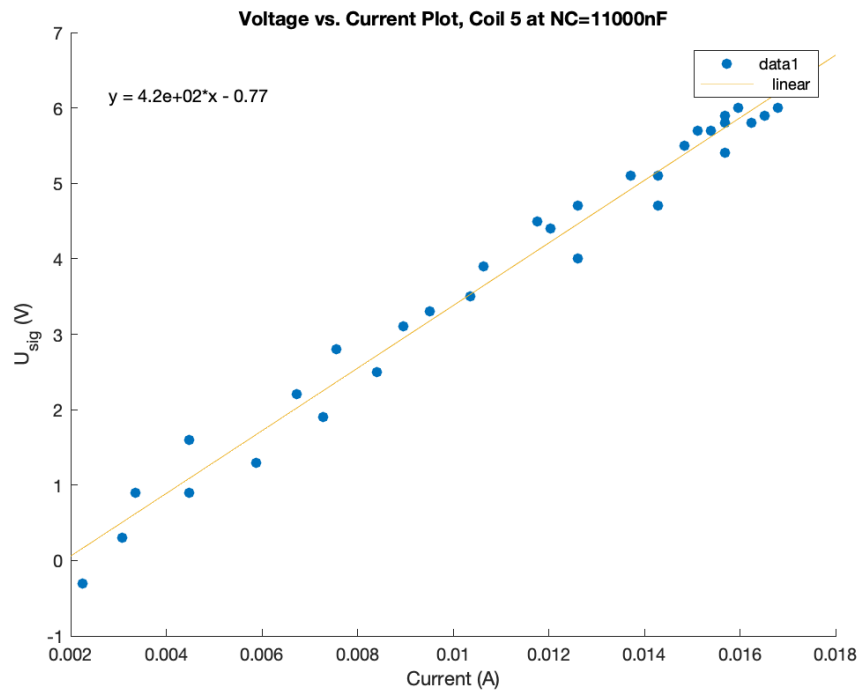


Figure 4.6: U_{sig} vs. Current graph from the calibration of coil No. 5 with 11000 nF.

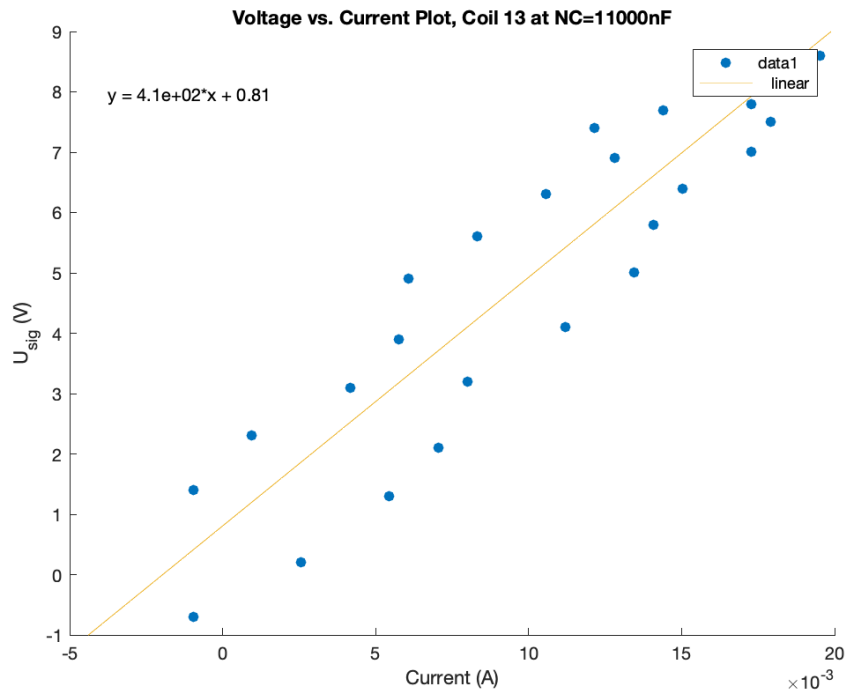


Figure 4.7: U_{sig} vs. Current graph from the calibration of coil No. 13 with 11000 nF.

linear equations to relate U_{sig} with B . Results are summarized in table 4.9 for further implementation in MEDUSA-CR tokamak.

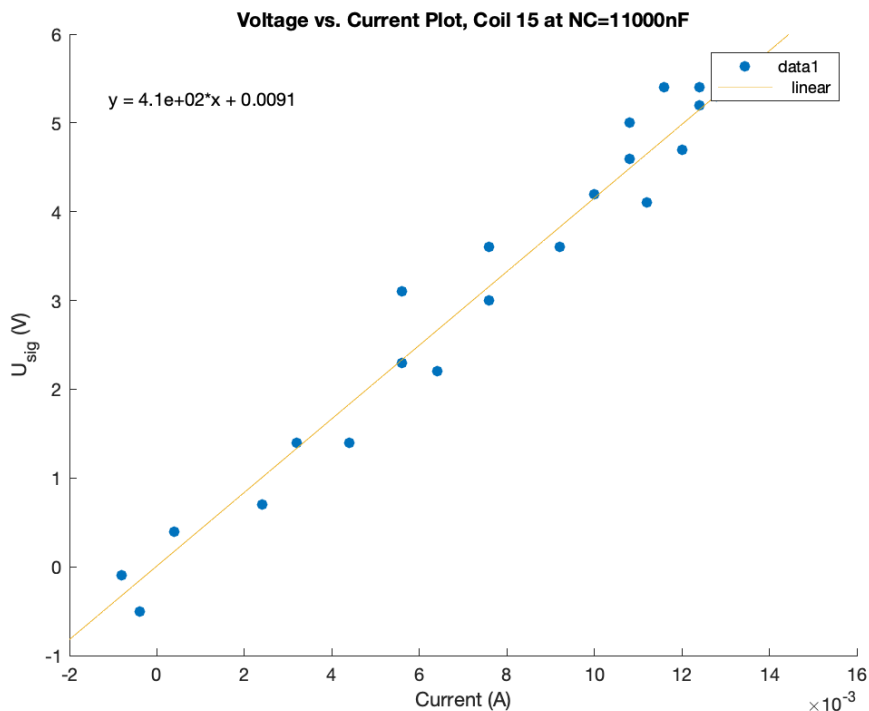


Figure 4.8: U_{sig} vs. Current graph from the calibration of coil No. 15 with 11000 nF.

Table 4.9: Linear relationships from coils Type A calibration.

Coil	Equation
1	$U_{sig} = 400 \frac{l}{\mu n} B - 0.48$
5	$U_{sig} = 420 \frac{l}{\mu n} B - 0.77$
13	$U_{sig} = 410 \frac{l}{\mu n} B - 0.81$
15	$U_{sig} = 410 \frac{l}{\mu n} B - 0.0091$

4.4 Integration

Signal integration is based on data obtained by Mirnov coils No. 15, Type A. As mentioned in section 3.5.3, signal is generated by plasma discharge No. 29293 in GOLEM tokamak. It is important to highlight that the full data spectrum from the 16 Mirnov coils, analyzed in section 3.5.1, can be retrieved from reference in [2], for useful plasma position calculations and MHD simulations.

GOLEM tokamak currently has 2 sets of Mirnov coils installed in opposite toroidal locations. Both rings have the same 16 coils mechanical configuration and electrical parameters. So, to check the correct functionality of the newly constructed coils, signals are compared with the other Mirnov set located in the opposite site of the tokamak, which was constructed and implemented by author in [22].

Although amplitude may differ between the compared coils due to plasma trajectory,

tendency shape should remain the same. Figure 4.9 shows the plot between integrated signal from the previously constructed Mirnov set in red and from the new set in blue. The difference between amplitudes of both signals is 0.00138 T.

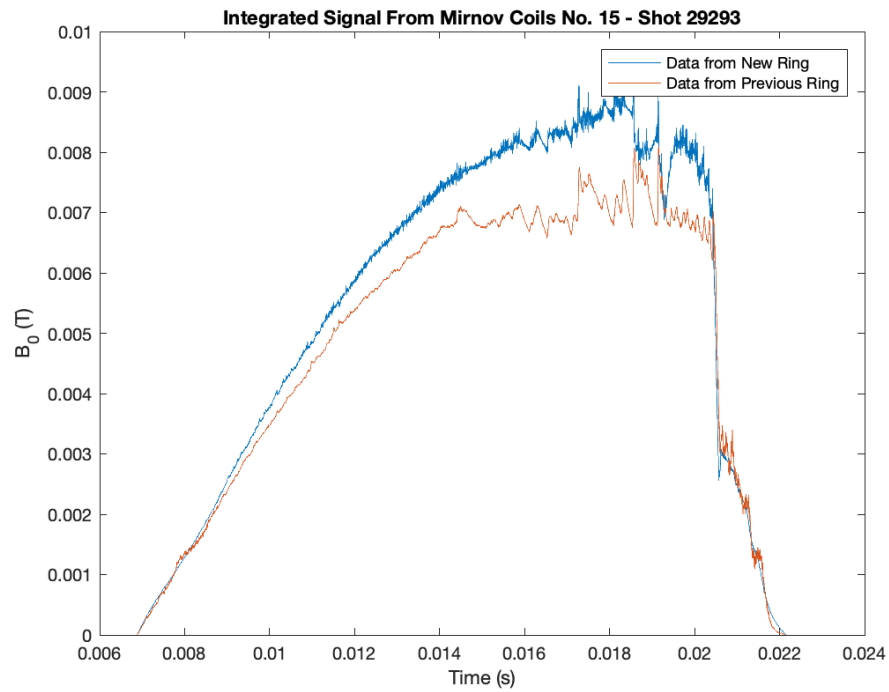


Figure 4.9: Signal integration comparison for coil 15 during shot No. 29293.

Chapter 5

Conclusions and Recommendations

5.1 Conclusions

By the end of this project, a complete mechatronics system of magnetic diagnostics for the MEDUSA-CR spherical tokamak is designed. Furthermore, a set of 16 Mirnov coils, which can be operated remotely, is constructed, calibrated and implemented in GOLEM tokamak at the Czech Technical University.

1. The mechanical system of the magnetic diagnostics is designed based on structural constraints of MEDUSA-CR, see figure 3.2. Chosen materials, specified in the attached blueprints, see A.6, are capable of high temperature and vacuum operation. Furthermore, electromechanical parts, as coils core and shielding, are designed to reduce stray fields presence and improve measurements precision.
2. The electronic system of the magnetic diagnostics is designed based on plasma measuring parameters. Response frequency f_{res} is the major constraint for the Mirnov coils and the diamagnetic loop electronic design. On the other hand, the critical aspect to take into consideration for Rogowski electronic system is the mechanical constraints. Design parameters for Mirnov coils, diamagnetic loop and Rogowski coil are shown in tables 3.1, 3.4 and 3.10 respectively.
3. A digital model of the diagnostics mechanical systems is created for stress analysis, as it is seen in figure 3.21. The study of finite elements, discussed in section 4.1, is applied to the parts of the Diagnostics Fixing Structure, which is the critical system. Values in table 4.4 show that the designed elements present low displacement under maximum stress situations and a minimum safety factor of 6.56.
4. A data acquisition system for MEDUSA-CR is selected based on the ATCA specifications. A general schematic is shown in figure 3.53 for a system with a sampling frequency $f_{sampling}$ of 1 MHz. Additionally, PICMG 3.x requirements are listed for future developments on the data acquisition system.

5. A set of 16 Mirnov coils, designed for GOLEM tokamak, is constructed, calibrated and implemented. A description of the construction and calibration procedures is discussed in sections 3.5.1 and 3.5.2 respectively. Additionally, the relationship between U_{sig} and B for coils Type A, which match with dimensions designed for MEDUSA-CR, is shown in table 4.9.

5.2 Recommendations

Wiring: Coils wiring is recommended to be protected from contact with any other mechanical part of the machine and from plasma. For this, KaptonTMtape can be used to fix the connecting cables to the diagnostics assembly, however an additional stainless steel thin pipe can be welded to the structure for the same purpose.

Winding: Winding process is critical for the optimal performance of the coils. So, it is highly recommended to buy or construct a mechanical drill, see figures 3.26 or 3.36, with a turn counter for this task. In case of the diamagnetic loop, an additional fixing structure must be adapted for a bigger core diameter.

Connection: Port feedthroughs are necessary to carry the coils signal out of the vessel. As it is mentioned in section 2.3, MEDUSA-CR has 26 CF ports to choose for this purpose. In total, the Mirnov coils, the diamagnetic loop and the Rogowski coil need 24 connection pins. To select the correct feedthroughs for MEDUSA-CR, the following questions must be answered:

1. On which ports will the feedthroughs be installed (CF standard)?
2. How many pins per feedthrough will be used?
3. What communication protocol will be required (eg. RS232, Ethernet, etc.)?

Provider in [6] offers a broad range of vacuum feedthroughs to select.

High frequency measurements: For future measurements in high frequency, is important to include a noise reduction system. Additionally, for the diagnostics system, it is recommended to include a low-pass filter and optocouplers for U_{sig} .

Bibliography

- [1] *PICMG*. Open Modular Computer Standards. URL <http://www.picmg.org/>.
- [2] *Tokamak GOLEM - Shot Database*. Czech Technical University. URL <http://golem.fjfi.cvut.cz/shots/29293//>.
- [3] *Golem opens to the world*. FJFI, Czech Technical University, 2012. URL <https://jaderka.fjfi.cvut.cz/blog/tokamak-golem-se-vydava-do-sveta>.
- [4] *Compass Tokamak*. Institute of Plasma Physics of CAS, 2018. URL http://www.ipp.cas.cz/vedecká_struktura_ufp/tokamak/tokamak_compass/.
- [5] F. Chen. *Introduction to Plasma Physics and Controlled Fusion*. Springer, New York, USA, second edition, 2006.
- [6] Kurt J. Lesker Company. *Kapton Isulated Wire*. URL https://www.lesker.com/newweb/feedthroughs/wire_kapton.cfm?pgid=0.
- [7] I. da Silva. *Real-time control for long ohmic alternate current discharges, Doctoral Dissertation*. Instituto Superior Tecnico de Lisboa, 2013.
- [8] P. Dhyani. *Personal Interview, Czech Technical University*. November, 2018.
- [9] A.S. Elahi. *Simultaneous Simple Measurements of Tokamak Plasma Parameters Especially Based on Plasma Diamagnetic Effect*. Journal of Nuclear and Particle Physics 2011, 2011.
- [10] E. J. Strait et al. *Magnetic Diagnostics*. Fusion Science and technology, vol. 53, 2008.
- [11] J. Mora et al. *First engineering stage of the Spherical Tokamak MEDUSA-CR*. 16th Latin American Workshop on Plasma Physics (LAWPP 2017), September, 2017.
- [12] J. Mora et al. *Implementation of the Spherical Tokamak MEDUSA-CR: stage 1*. 27th IAEA Fusion Energy Conference (FEC 2018), October, 2018.
- [13] J. Wesson et al. *Tokamaks*. Oxford University Press, Oxford, UK, fourth edition, 2011.
- [14] K. Lackner et al. *Fusion Physics*. International Atomic Energy Agency, Vienna, Austria, 2012.

- [15] L.L. Lao et al. *Reconstruction of current profile parameters and plasma shapes in tokamaks*. Nuclear Fusion, Vol. 25, Num. 11, 1985.
- [16] Utrilla et al. *Diseño Concurrente*. Universidad Autónoma del Estado de México. URL <http://ri.uaemex.mx/bitstream/handle/20.500.11799/31293/secme-15986.pdf?sequence=1>.
- [17] J. Freidberg. *Plasma Physics and Fusion Energy*. Cambridge, New York, USA, 2007.
- [18] J.P. Freidberg. *Ideal Magnetohydrodynamics*. Plenum Press, New York, USA, 1987.
- [19] G.D. Garstka. *Start up and Stability of a Small Spherical Tokamak, Doctoral Dissertation*. University of Wisconsin-Madison, 1997.
- [20] I.H. Hutchinson. *Principles of Plasma Diagnostics*. Cambridge University Press, New York, USA, second edition, 2002.
- [21] J. Mora I. Vargas. Diagnóstico del tokamak esférico medusa-cr, 2017. URL <https://repositoriotec.tec.ac.cr/bitstream/handle/2238/9329/actividad-diagnostico-medusa-cr.pdf?sequence=1&isAllowed=y>.
- [22] T. Markovic. *Measurement of Magnetic Fields on GOLEM Tokamak, Engineering Diploma Thesis*. Czech Technical University, 2012.
- [23] Y-K.M. Peng and D.J. Strickler. *Features of Spherical Torus Plasmas*. IAEA Nuclear Fusion, Oak Ridge, USA, 1986.
- [24] R.S. Popovic. *Hall Effect Devices*. Taylor Francis Group, Florida, USA, second edition, 2003.
- [25] Accuglass Products. *Vacuum Insulated Wire*. URL <https://www.accuglassproducts.com/>.
- [26] J. Nisbett R. Budynas. *Shigley's Mechanical Engineering Design*. McGraw-Hill, New York, USA, ninth edition, 2012.
- [27] P. Rutherford R. Goldston. *Introduction to Plasma Physics*. Taylor and Francis Group, Florida, USA, 1995.
- [28] V. Svoboda. *Personal Interview, Czech Technical University*. December, 2018.
- [29] A. Torres. *Personal Interview, Czech Institute of Plasma Physics*. December, 2018.
- [30] S. Tumanski. *Induction coil sensors — a review*. Meas. Sci. Technol., vol. 18, 2007.
- [31] H. Zijlstra. *Experimental Methods in Magnetism*. Amsterdam, 1967.

Appendix A

Matlab Programs

A.1 Mirnov Coils Parameter Calculation

```
1 %Author: Juan Ignacio Monge Colepicolo
2 %Date: 10/2018
3 %Instituto Tecnologico de Costa Rica
4
5 %Mirnov Calculations:
6
7 clc;
8
9 clear all;
10
11 %Mirnov Coils constants:
12
13 l=8*10(-3); %m (coil length)
14
15 d=0.1*10(-3); %m (wire diameter)
16
17 Di=8*10(-3); %m (core diameter)
18
19 Do=8.4*10(-3); %m (winding diameter)
20
21 D=8.4*10(-3); %m (8mm + 0.1mm x 4)
22
23 D2=(Di+Do)/2; %m (average diameter of the coil)
24
25 Nl=2; %Number of layers
26
27 m0=4*pi*10(-7); %permeability constant (free space)
28
29 ro=1.68*10(-8); %copper resistivity
30
31 %-----Inductance-----
32
33 %L=Nl*k*((pi*D2*l)/(pi*d2));
```

```

34
35 L=Nl*m0*((pi*(D2^2)*l)/(4*d^2)); %For thin wire coils
36
37 %-----Resistivity-----
38
39 R=Nl*ro*((4*D2*l)/(d^3));
40
41 %-----Effective Area-----
42
43 A=Nl*(((pi*l*(D^2))/(4*d)));
44
45 %-----Resonant Frequency-----
46
47 C=500*10^(-12); %pF (Capacitance for a 5m wire)
48
49 fres=1/(2*pi*sqrt(L*C));
50
51 f=R/L;
52
53 %-----K Relationship-----
54
55 K=l/Di;
56
57 syms L2
58
59 eqn = 75000 == 1/(2*pi*sqrt(L2*500*10^(-12)));
60
61 solveL = solve(eqn, L2);
62
63 Usig = Nl*(pi^(2)*D^(3)*0.8*fres)/(2*d);

```

Listing A.1: Source: MirnovCalc.m

A.2 Diamagnetic Loop Parameter Calculation

```

1 %Author: Juan Ignacio Monge Colepicolo
2 %Date: 10/2018
3 %Instituto Tecnológico de Costa Rica
4
5 %Diamagnetic Loop Calculations:
6
7 clc;
8
9 clear all;
10
11 %DL constants:
12
13 l=50*10^(-3); %m (coil length)
14
15 d=0.25*10^(-3); %m (wire diameter)
16

```

```

17 Di=250*10(-3); %m (core diameter)
18
19 Do=255*10(-3); %m (winding diameter)
20
21 D=255.6*10(-3); %mm (8mm + 0.1mm x 4)
22
23 D2=(Di+Do)/2; %m (average diameter of the coil)
24
25 Nl=2; %Number of layers
26
27 m0=4*pi*10(-7); %permeability constant (free space)
28
29 ro=1.68*10(-8); %copper resistivity
30
31 %-----Inductance-----
32
33 %L=Nl*k*((pi*D2*l)/(pi*d2));
34
35 L=Nl*m0*((pi*(D22)*l)/(4*d2)); %For thin wire coils
36
37 %-----Resistivity-----
38
39 R=Nl*ro*((4*D*l)/(d3));
40
41 %-----Effective Area-----
42
43 A=Nl*(((pi*l*(D2))/(4*d)));
44
45 %-----Resonant Frecuency-----
46
47 C=1000*10(-12); %pF (Capacitance for a 10m wire)
48
49 fres=1/(2*pi*sqrt(L*C));
50
51 f=R/L;
52
53 K=l/Di;
54
55 n=l/d;
56
57 Usig = Nl*(pi(2)*D(3)*0.8*fres)/(2*d);

```

Listing A.2: Source: DLCalc.m

A.3 Rogowski Coil Parameter Calculation

```

1 %Author: Juan Ignacio Monge Colepicolo
2 %Date: 10/2018
3 %Instituto Tecnologico de Costa Rica
4
5 %Rogowski Calculations:

```

```

6
7 clc;
8
9 clear all;
10
11 %Rogowski Coils constants:
12
13 l=1.2; %m (coil length)
14
15 d=0.22*10(-3); %m (thin wire diameter)
16
17 Di=7.73*10(-3); %m (core diameter)
18
19 Do=d*2+Di; %m (winding diameter)
20
21 D=250*10(-3); %mm (8mm + 0.1mm x 4)
22
23 D2=(Di+Do)/2; %m (average diameter of the coil)
24
25 Nl=1; %Number of layers
26
27 m0=4*pi*10(-7); %permeability constant (free space)
28
29 ro=1.68*10(-8); %copper resistivity
30
31 %-----Inductance-----
32
33 %L=Nl*k*((pi*D2*l)/(pi*d2));
34
35 L=Nl*m0*((pi*(D22)*l)/(4*d2)); %For thin wire coils
36
37 %-----Resistivity-----
38
39 R=Nl*ro*((4*D2*l)/(d3));
40
41 %-----Effective Area-----
42
43 A=Nl*(((pi*l*(D2))/(4*d)));
44
45 %-----Resonant Frecuency-----
46
47 C=500*10(-12); %pF (Capacitance for a 5m wire)
48
49 fres=1/(2*pi*sqrt(L*C));
50
51 f=R/L;
52
53 %-----K Relationship-----
54
55 K=1/Di;
56
57 syms L2

```

```

58
59 eqn = 75000 == 1/(2*pi*sqrt(L2*500*10^(-12)));
60
61 solveL = solve(eqn, L2);
62
63 Usig = Nl*(pi^(2)*D^(3)*0.8*fres)/(2*d);

```

Listing A.3: Source: RogowskiCalc.m

A.4 Mirnov Coils Calibration

```

1 %Author: Juan Ignacio Monge Colepicolo
2 %Date: 10/2018
3 %Instituto Tecnologico de Costa Rica
4
5 %#####
6
7 clear all;
8 clc;
9
10 %#####
11
12 %-----Calibration to relate the current (I) and signal (V)-----
13
14 %#####
15
16 %-----Current data analysis-----
17
18 Mc = csvread('320a.csv',18,0);
19
20 %The columns of the .csv file are separated:
21
22 A1c=Mc(:,2);
23 A2c=Mc(:,end);
24 tmc=Mc(:,1);
25
26 %Filtering of the signal
27
28 Mcav=(A1c+A2c)/2;
29 McavAmp0=100*Mcav;
30
31 %Comparison of both original signals:
32
33 tmc0=tmc(150:300);
34 Mcav0=Mcav(150:300);
35
36 %Amplification due to current signal strength:
37
38 McavAmp=100*Mcav0;
39
40 %Low pass filter due to the noise present in the current signal:

```

```
41
42 d1 = designfilt('lowpassiir','FilterOrder',12,'HalfPowerFrequency',0.15,'
    DesignMethod','butter');
43 McavFil = filtfilt(d1,McavAmp);
44
45 %Calibration of signals:
46
47 tmc1=tmc(189:209);
48 Mcav1=McavFil(39:59);
49
50
51 %—————Coil Signal data analysis—————
52
53 Ms = csvread('320b.csv',18,0);
54
55 A1s=Ms(:,2);
56 A2s=Ms(:,end);
57 tms=Ms(:,1);
58
59 %Filtering of the signal
60
61 Msav=(A1s+A2s)/2;
62
63 %Comparison of both original signals:
64
65 tms0=tms(150:300);
66 Msav0=Msav(150:300);
67
68 %Phase displacement correction
69
70 tms2=tms0+0.11*10(-4);
71
72 %Calibration of signals:
73
74 tms1=tms(208:228);
75 Msav1=Msav(208:228);
76
77 %—————Plot of the obtained signals—————
78
79 %Plot of the original signals:
80
81 figure
82 plot(tms0, Msav0, tmc0, Mcav0);
83 title('Original Signals Without Amplification')
84 xlabel('Time (s)')
85 ylabel('Voltage (V)')
86
87 %Plot of the original signals with amplified Current:
88
89 figure
90 plot(tms0, Msav0, tmc0, McavAmp);
91 title('Original Signals With Amplification')
```

```
92 xlabel('Time (s)')
93 ylabel('Voltage (V)')
94
95 %Plot of the original signals with amplified Current:
96
97 figure
98 plot(tms0, Msav0, tmc0, McavFil);
99 title('Original Signals With Amplification')
100 xlabel('Time (s)')
101 ylabel('Voltage (V)')
102
103 %Plot of signals with time displacement:
104
105 figure
106 plot(tms2, Msav0, tmc0, McavFil);
107 title('Original Signals With Phase Correction')
108 xlabel('Time (s)')
109 ylabel('Voltage (V)')
110
111 %Plot of corrected V signal:
112
113 figure
114 plot(Msav1);
115 title('Coil Signal Plot in Analysis Range')
116 xlabel('Data Plot (n)')
117 ylabel('Voltage (V)')
118
119 %Plot of corrected I signal:
120
121 figure
122 plot(Mcav1*(1/5));
123 title('Current Signal Plot in Analysis Range')
124 xlabel('Data Plot (n)')
125 ylabel('Current (A)')
126
127 %Plot of both signals for the tendency line:
128
129 figure
130 scatter(Mcav1*(1/5),Msav1, 'filled');
131 title('Voltage vs. Current Plot')
132 xlabel('Current (A)')
133 ylabel('Coil Signal (V)')
```

Listing A.4: Source: Data320Hz01.m

A.5 Mirnov Coil No.11 Signal Integration

```
1 %Author: Juan Ignacio Monge Colepicolo
2 %Date: 10/2018
3 %Instituto Tecnológico de Costa Rica
4
```



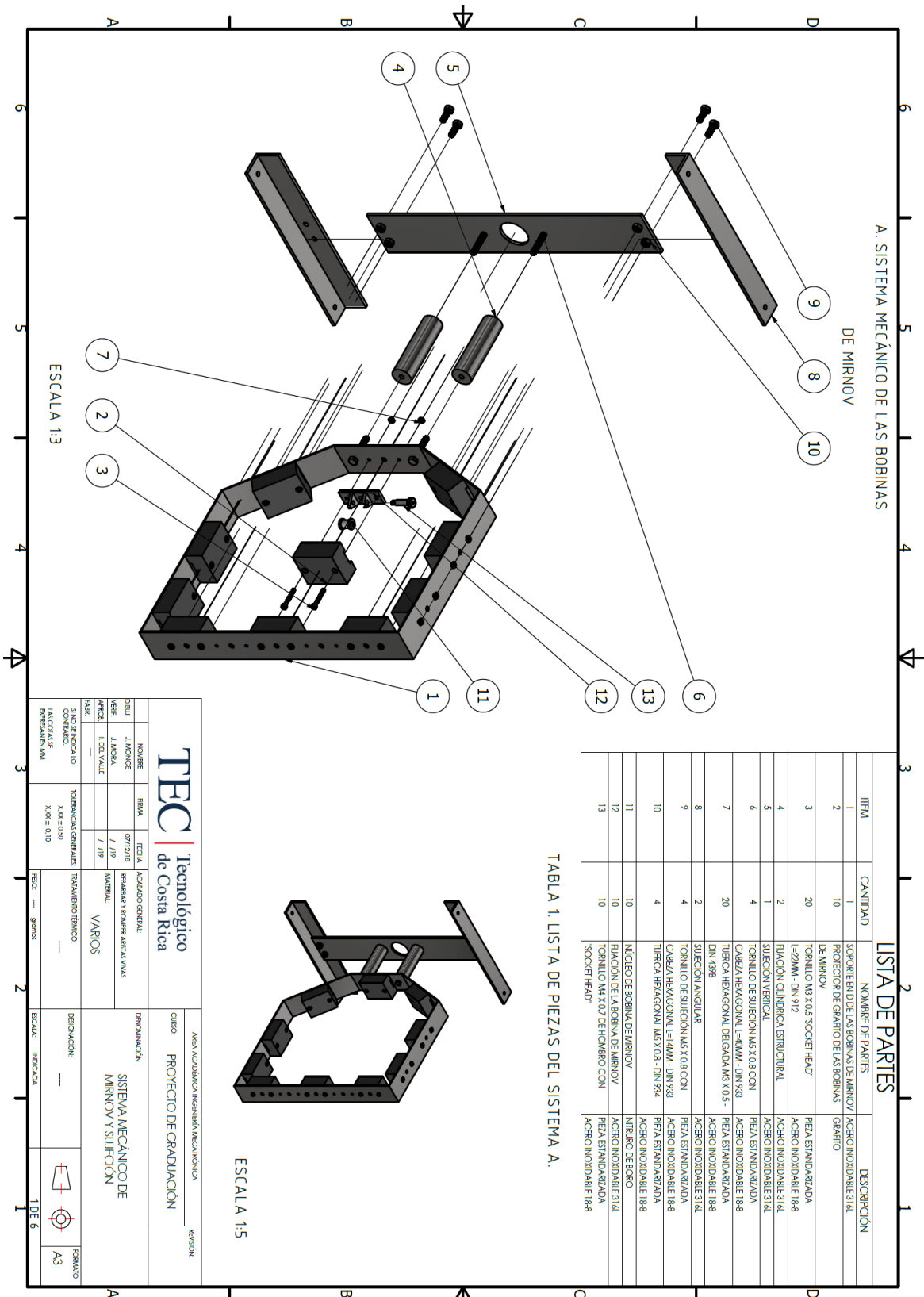
```

5
6 %#####
7
8 clear all;
9 clc;
10
11 %#####
12
13 %-----Integration of the Mirnov coil No. 11 data, Shot 29293
14
15 %#####
16
17 %-----Integration data analysis-----
18
19 Mc = csvread('j11.csv');
20 A2c=Mc(:,end);
21 t=Mc(:,1);
22
23
24 %Cutting data in presence of plasma:
25 coil=A2c(6883:22150);
26
27 %Substracting the drift:
28 Mcoil=mean(coil);
29 Dcoil=coil-Mcoil;
30
31 %Data Integration:
32 intCoil=cumsum(Dcoil);
33
34 %Dividing Integrated Data by the Coefficient:
35 coeff = 32.3*1000;
36 Fint=intCoil/(coeff);
37
38 %Time Lapse is Also cut in the Same Range:
39 tp=t(6883:22150);
40
41 figure
42 plot(t,A2c);
43 title('Raw Signal From Mirnov Coil No. 11 - Shot 29293')
44 xlabel('Time (s)')
45 ylabel('U_{sig} (V)')
46 legend('Data')
47
48 figure
49 plot(tp,Fint);
50 title('Integrated Signal From Mirnov Coil No. 11 - Shot 29293')
51 xlabel('Time (s)')
52 ylabel('B_{0} (T)')

```

Listing A.5: Source: IntegrationM11.m

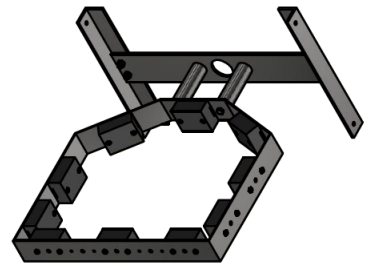
A.6 Mechanical Blueprints of the Magnetic Diagnostics



TEC | Tecnológico de Costa Rica

NOBRE	FINA	FECHA	ACADIAO ENERJIA MECANICA	REVISION
J. MONSE	07/7/18			
VERE	J. MONSE	7/18	BOBINAS Y COVER ASIST. VIVA	
AFOR	L. DEL VALLE	7/18	VARIOS	
FILE				
SIN ENCAJO	TOLERANCIA ENERJIA	TAMBIEN ENERJIA	DESIGNACION	ESCALA
LACONATE	XXX ± 0.50	XXX ± 0.10		
DESNAN EN MM	XXX ± 0.10			

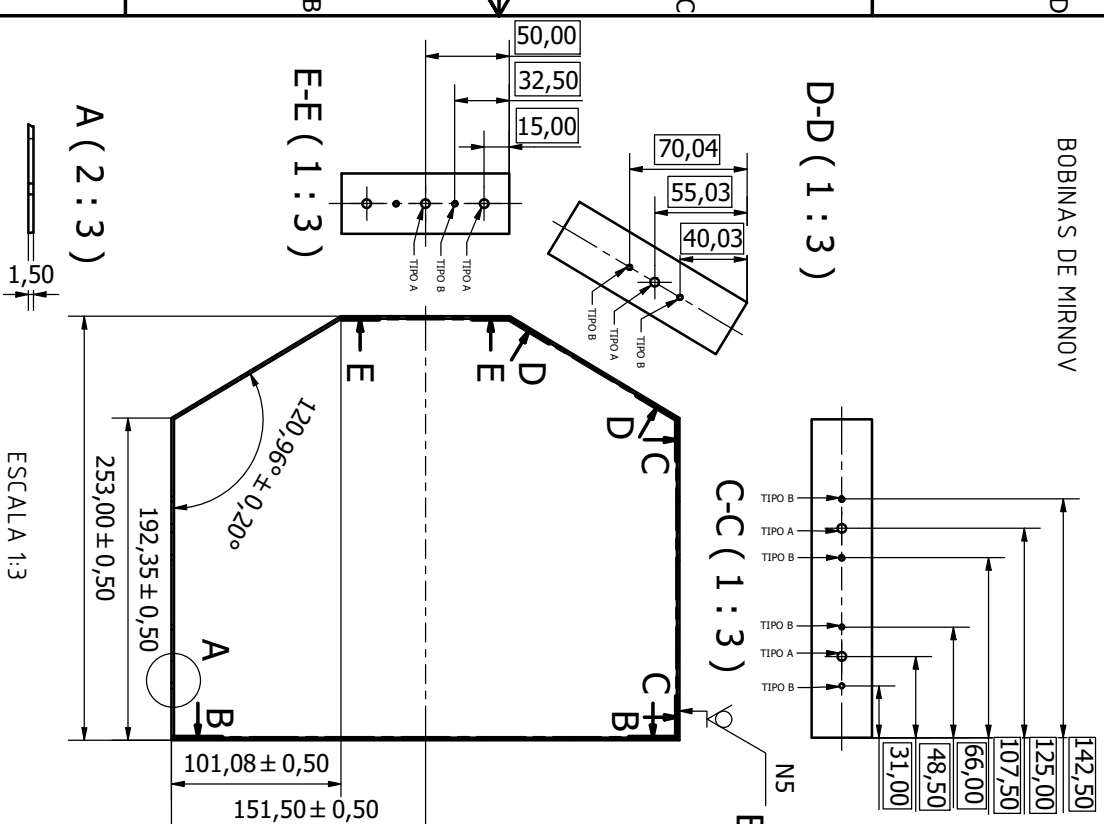
ESCALA 1:3



ESCALA 1:5

TABLA 1. LISTA DE PIEZAS DEL SISTEMA A.

1. SOPORTE EN D DE LAS BOBINAS DE MIRNOV



D-D (1:3)

C-C (1:3)

B-B (1:3)

F (2:3)

G (2:3)

ESCALA 1:3

ESCALA 1:5

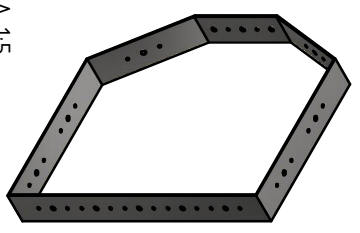
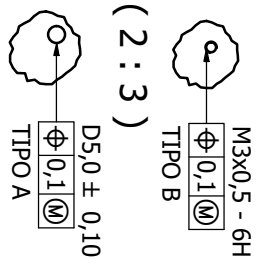


TABLA DE REVISIÓN				
ZONA	NUM. REVISIÓN	DESCRIPCIÓN	FECHA	APROBADO POR
	1			
	2			
	3			
	4			
	5			
	6			
	7			

TABLA 2. TABLA DE REVISIÓN PIEZA 1.

NOTAS:

1. INTERPRETACIÓN SEGÚN NORMA ISO.
2. TODAS LAS DIMENSIONES EN MM.
3. MATERIAL INDICADO EN LA TABLA 1 DEL SISTEMA.
4. FILLOS NO INDICADOS: BISEL ± 0,1.
5. TOLERANCIAS GENERALES EN CAJETÍN.

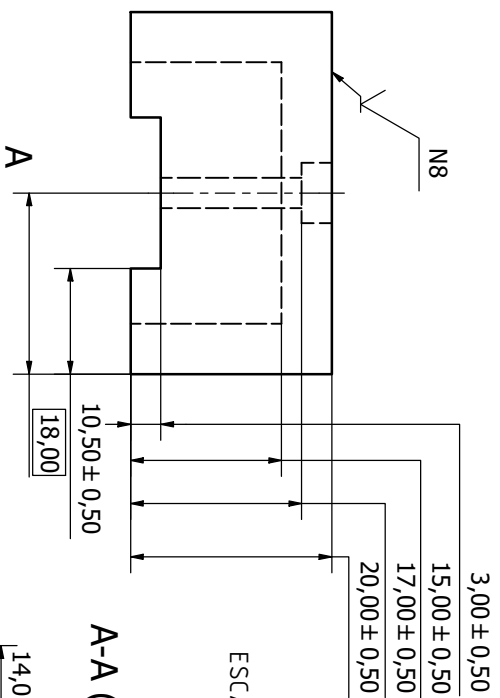


<p>Tecnológico de Costa Rica</p>		<p>ÁREA ACADÉMICA INGENIERÍA MECATRÓNICA</p>	
<p>NOBRE: J. MONSE</p> <p>VERIF.: J. MORRA</p> <p>APROB.: L. DEL VALLE</p> <p>FEABE: ----</p>	<p>RIMA: ----</p> <p>FECHA: 07/12/18</p> <p>REVISAR Y ROYVER ABSTAS VIAS</p> <p>MATERIAL: VARIOS</p>	<p>DESIGNACIÓN: ----</p> <p>ESCALA: INDICADA</p>	<p>REVISIÓN: ----</p> <p>CURSO: PROYECTO DE GRADUACIÓN</p> <p>DESIGNACIÓN: SISTEMA MECÁNICO DE MIRNOV Y SUJECIÓN</p>
<p>SINO SE INDICA LO CONTRARIO: XXX ± 0,50</p> <p>EXRESAN EN MM XXX ± 0,10</p>	<p>TOLERANCIAS GENERALES: TRATAMIENTO TÉRMICO: ----</p> <p>FINO: ---- gramos</p>	<p>2 DE 6</p>	<p>FORMATO A3</p>

TABLA DE REVISIÓN				
ZONA	NUM. REVISIÓN	DESCRIPCIÓN	FECHA	APROBADO POR
	1			
	2			
	3			
	4			
	5			
	6			
	7			

2. PROTECTOR DE GRAFITO
DE LAS BOBINAS DE MIRNOV

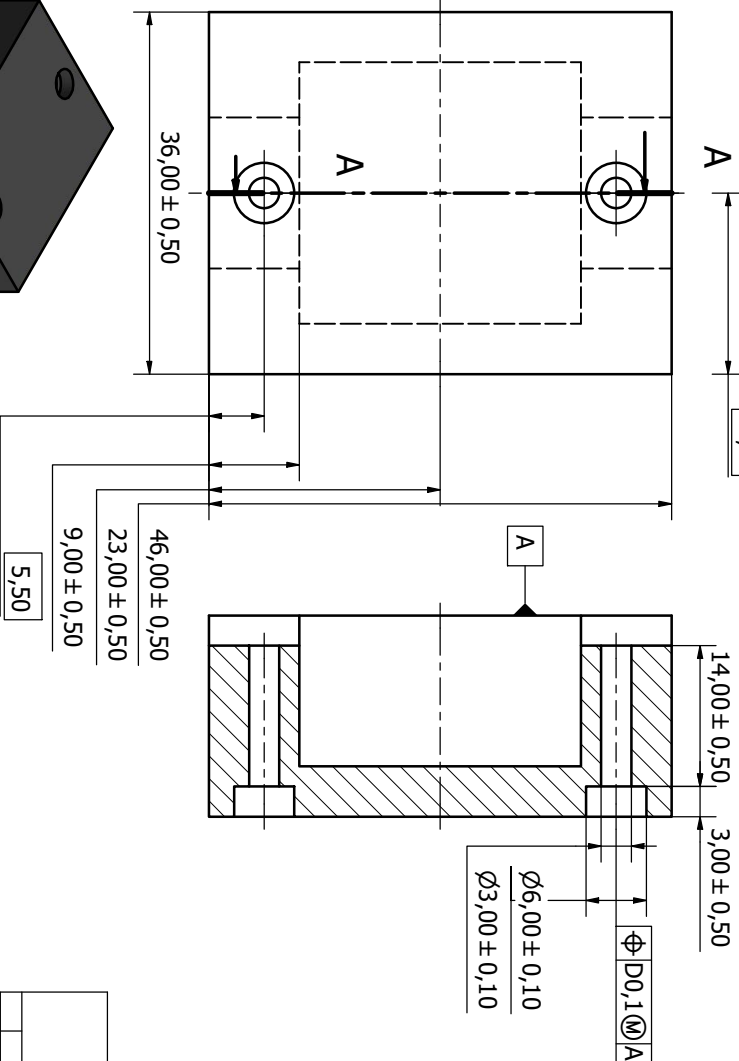
ESCALA 2:1



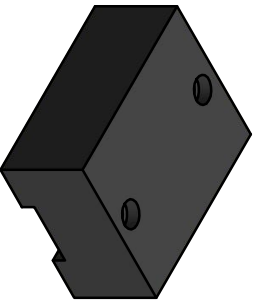
A-A (2 : 1)

NOTAS:

1. INTERPRETACIÓN SEGÚN NORMA ISO.
2. TODAS LAS DIMENSIONES EN MM.
3. MATERIAL INDICADO EN LA TABLA 1 DEL SISTEMA.
4. FILDS NO INDICADOS: BISEL ± 0.1 .
5. TOLERANCIAS GENERALES EN CAJETÍN.



ESCALA 1:1



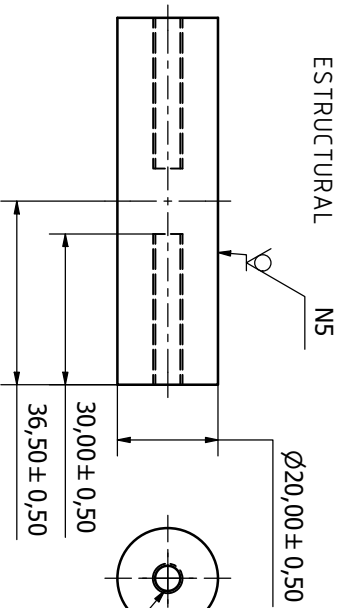
TEC Tecnológico
de Costa Rica

ÁREA ACADÉMICA INGENIERÍA MECATRÓNICA			REVISIÓN:	
CURSO: PROYECTO DE GRADUACIÓN				
NOBRE:	RMVA	FECHA:		
DEBUI:	J. MONCE	FECHA:		
VERIF.:	J. MOBA	FECHA:		
APROB.:	L. DEL VALLE	FECHA:		
FABR:	---	FECHA:		
SINO SE INDICA LO CONTRARIO:		TOLERANCIAS GENERALES:		
LAS CONASSE		XXX ± 0,50		
EXPRESE EN MM		XXX ± 0,10		
TRATAMIENTO TÉRMICO:				

FINO: --- gramos				
DESIGNACIÓN:				

Escala: INDICADA				
3 DE 6				
FORMATO				
A3				

4. FIJACIÓN CILÍNDRICA



ESCALA 1:1

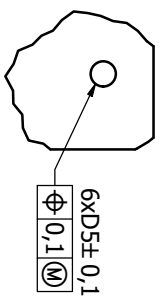
TABLA DE REVISIÓN				
ZONA	NUM. REVISIÓN	DESCRIPCIÓN	FECHA	APROBADO POR
1				
2				
3				
4				
5				
6				
7				

TABLA 4. TABLA DE REVISIÓN PIEZA 4 Y 5.

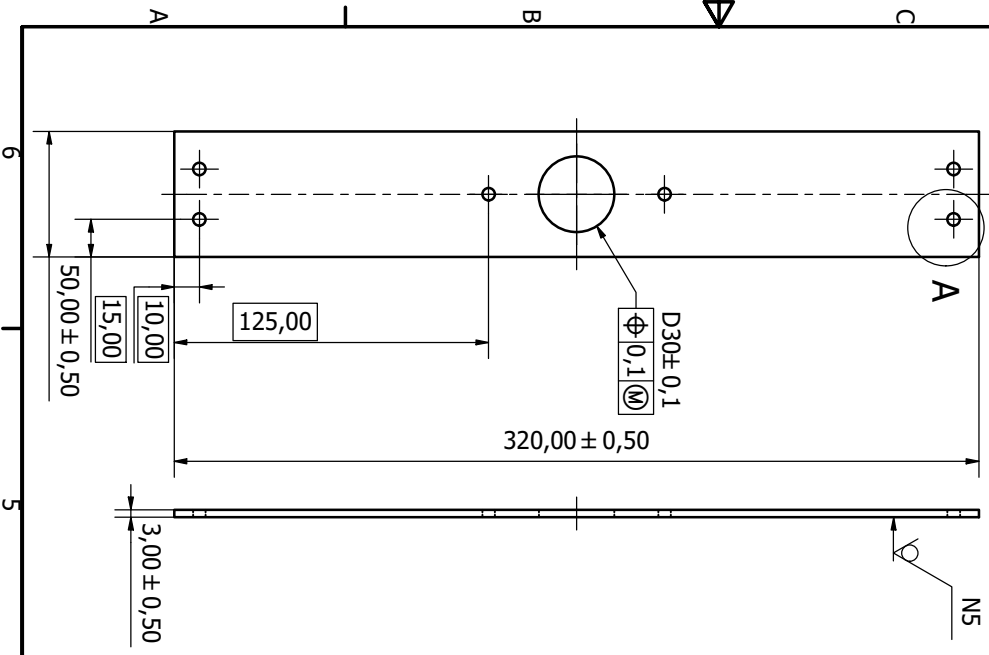
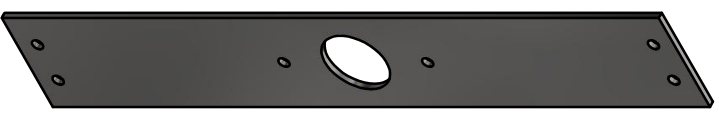
NOTAS:

1. INTERPRETACIÓN SEGÚN NORMA ISO.
2. TODAS LAS DIMENSIONES EN MM.
3. MATERIAL INDICADO EN LA TABLA 1 DEL SISTEMA.
4. FILLOS NO INDICADOS: BISEL $\pm 0,1$.
5. TOLERANCIAS GENERALES EN CAJETÍN.
6. EL AGUJERO ROSCADO CON M5X0,8 - 6H SE PERFORA EN LAS DOS CARAS OPUESTAS DE LA PIEZA 4.

A (1:1)



5. SUJECIÓN VERTICAL



ESCALA 1:2

<p>Tecnológico de Costa Rica</p>		ÁREA ACADÉMICA INGENIERÍA MECATRÓNICA		REVISIÓN:			
		CURSO: PROYECTO DE GRADUACIÓN					
DIBUJ.: J. MONTE VERIF.: J. MONTE APROB.: L. DEL VALLE FABR:	FECHA: 07/12/18 / 1/19 / 1/19	ACABADO GENERAL: REBARBAR Y ROQUEAR ABRAS VIVAS	MATERIAL: VARIOS	TRATAMIENTO TÉRMICO: ---	DESIGNACIÓN: ---	ESCALA: INDICADA	4 DE 6
SIN SE INDICAR LO CONTRARIO: LAS COMASE EXPRESAN EN MM		TOLERANCIAS GENERALES: XXX \pm 0,50 XXX \pm 0,10		SINO SE INDICAR LO CONTRARIO: LAS COMASE EXPRESAN EN MM			



FORMATO A3

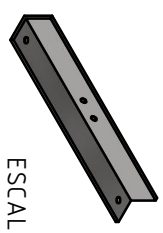
TABLA DE REVISIÓN				
ZONA	NUM. REVISIÓN	DESCRIPCIÓN	FECHA	APROBADO POR
1				
2				
3				
4				
5				
6				
7				

TABLA 5. TABLA DE REVISIÓN PIEZA 8, 11 Y 12.

NOTAS:

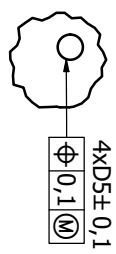
1. INTERPRETACIÓN SEGÚN NORMA ISO.
2. TODAS LAS DIMENSIONES EN MM.
3. MATERIAL INDICADO EN LA TABLA 1 DEL SISTEMA.
4. FILLOS NO INDICADOS: BISEL $\pm 0,1$.
5. TOLERANCIAS GENERALES EN CAJETÍN.
6. EL ESPESOR DE LA PIEZA 8 ES DE 3 MM EN SU TOTALIDAD.

8. SUJECIÓN ANGULAR

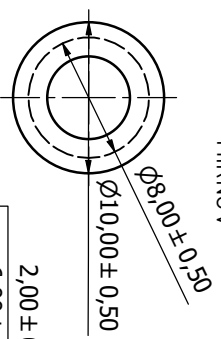


ESCALA 1:4

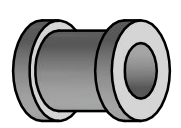
C (1:1)



11. NÚCLEO DE LA BOBINA DE MIRNOV

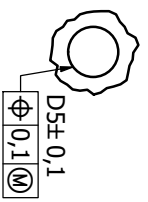


ESCALA 3:1

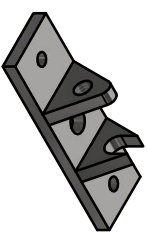


ESCALA 2:1

D (2:1)

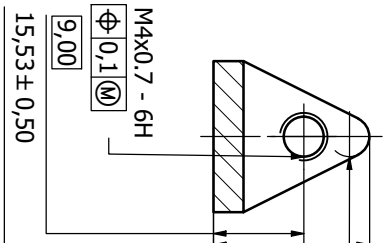


12. FIJACIÓN DE LA BOBINA DE MIRNOV

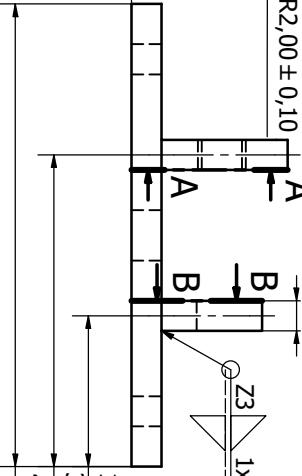


ESCALA 1:1

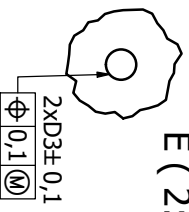
A-A (2:1)



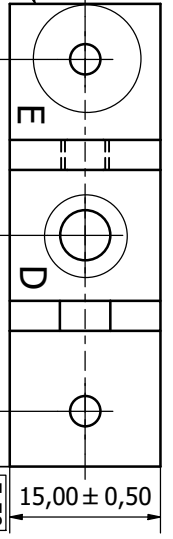
B-B (2:1)



E (2:1)



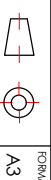
ESCALA 2:1



TEC Tecnológico de Costa Rica

ÁREA ACADÉMICA INGENIERÍA MECATRÓNICA			REVISIÓN:	
CURSO: PROYECTO DE GRADUACIÓN				
NOBRE:	RIWA	FECHA:		
DEBUI:	J. MONTE	07/12/18		
VERIF:	J. MORRA	/ / 19		
APROB:	L. DEL VALLE	/ / 19		
FABR:				
SINÓ SE INDICALO CONTRARIO: XXX±0,50			TOLERANCIAS GENERALES: TRATAMIENTO TÉRMICO: ---	
LAS COMASE XXX±0,10			FIBO: --- gramos	
ERRERAN EN MM			ESCALA: INDICADA	
			5 DE 6	

DESIGNACIÓN: SISTEMA MECÁNICO DE MIRNOV Y SUJECIÓN



FORMATO A3

D. SISTEMA DE SUJECIÓN CON LAS BOBINAS PRINCIPALES

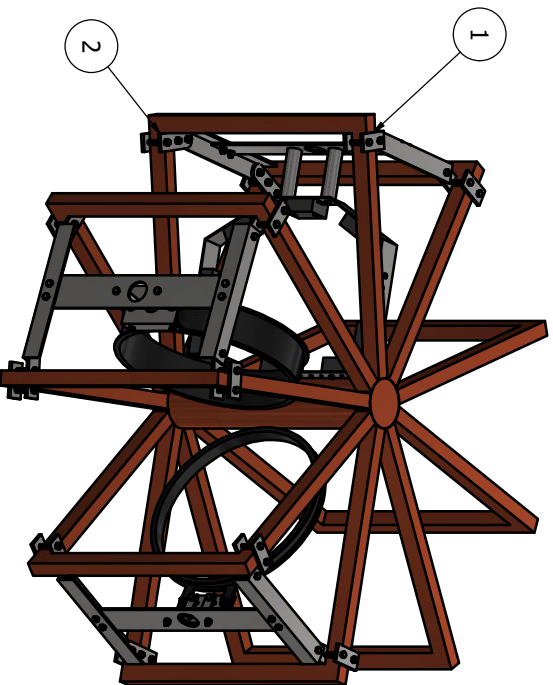
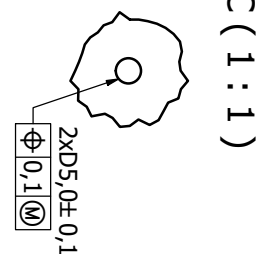
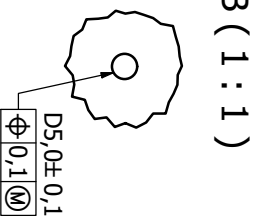
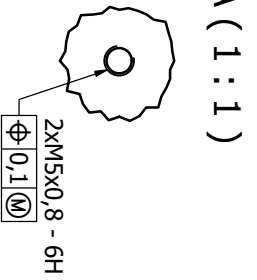
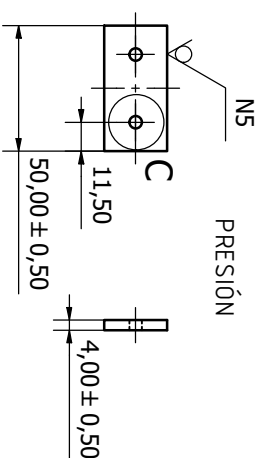
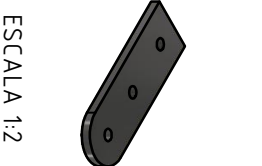
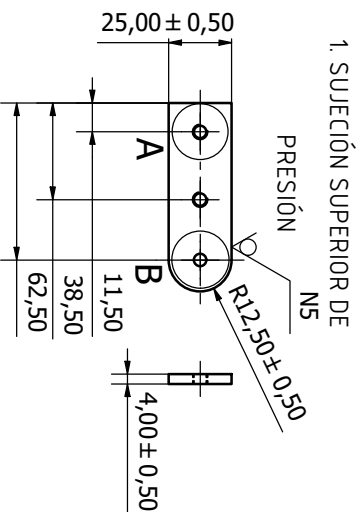


TABLA DE REVISIÓN				
ZONA	NUM. REVISIÓN	DESCRIPCIÓN	FECHA	APROBADO POR
	1			
	2			
	3			
	4			
	5			
	6			
	7			

TABLA 5. TABLA DE REVISIÓN PIEZA 1 Y 2.

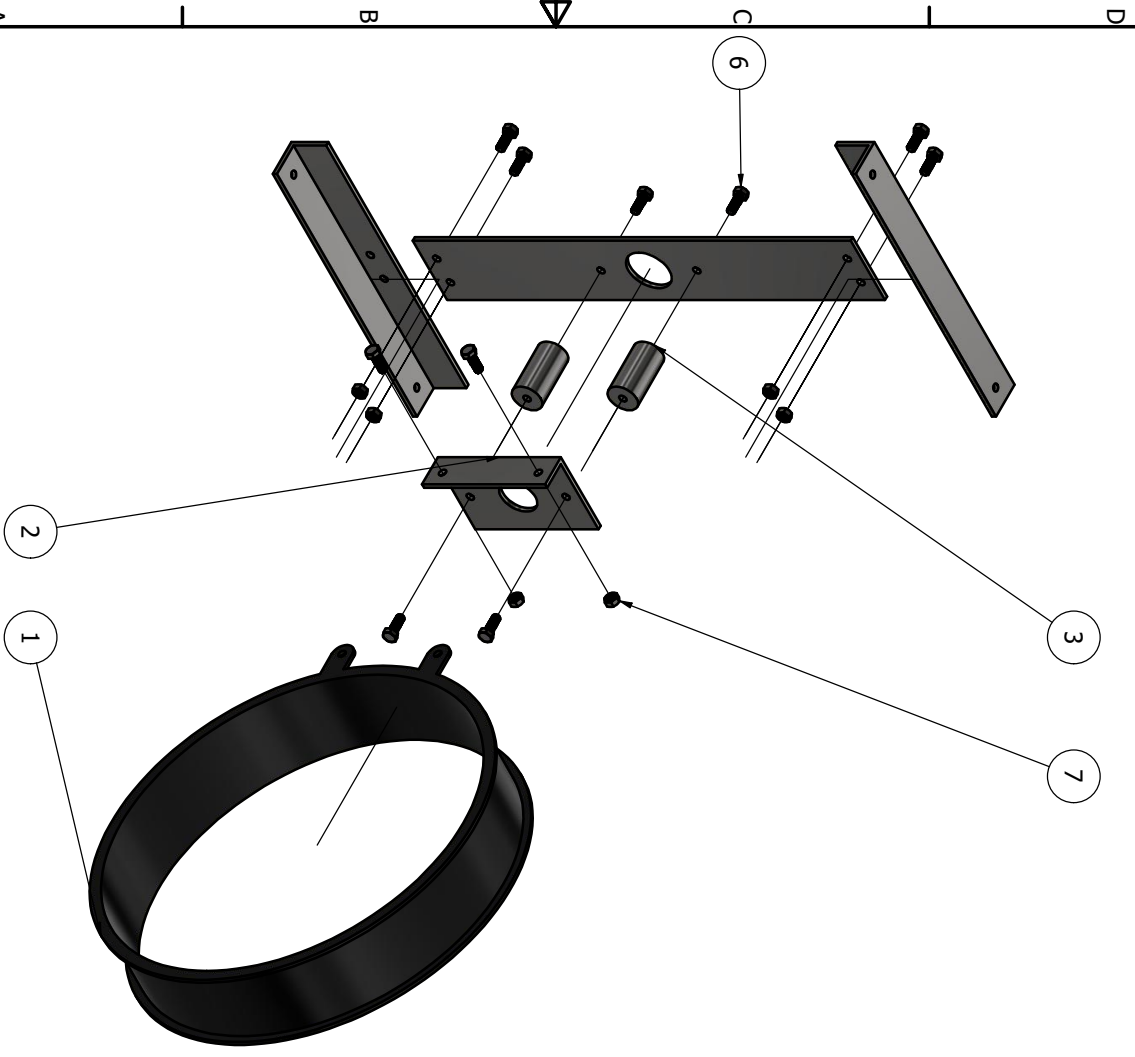
NOTAS:

1. INTERPRETACIÓN SEGÚN NORMA ISO.
2. TODAS LAS DIMENSIONES EN MM.
3. MATERIAL: ACERO INOXIDABLE 316L.
4. FILLOS NO INDICADOS: BISEL $\pm 0,1$.
5. TOLERANCIAS GENERALES EN CAJETÍN.
6. CANTIDAD TOTAL PIEZAS 1 Y 2: 12



Tecnológico de Costa Rica			AREA ACADÉMICA INGENIERÍA MECATRÓNICA REVISOR:		
NOMBRE: J. MONCE VERIF.: J. MORRA APROB.: L. DEL VALLE FABR:	FIRMA:	FECHA: 07/12/18 / 1/19	ACABADO GENERAL: REBARBAR Y ROVER ARISTAS VIVAS MATERIAL: VARIOS TRATAMIENTO TÉRMICO:	DESIGNACIÓN:	ESCALA: INDICADA
SIN SE INDICARLO CONTRARIAMENTE: LAS CONJUNTES DEBERÁN ENVIAR			TOLERANCIAS GENERALES: XXX ± 0,50 / XXX ± 0,10	6 DE 6	FORMATO A3

B. SISTEMA MECÁNICO DEL DIAMAGNETIC LOOP



ESCALA 1:3

LISTA DE PARTES			
ITEM	CANTIDAD	NOMBRE DE PARTE	DESCRIPCIÓN
1	1	NÚCLEO DE BOBINA DEL DIAMAGNETIC LOOP	GRAFITO
2	1	SOPORTE ANGULAR DEL DIAMAGNETIC LOOP	ACERO INOXIDABLE 316L
3	2	FIJACIÓN CILÍNDRICA ESTRUCTURAL DEL DIAMAGNETIC LOOP	ACERO INOXIDABLE 316L
4	1	SUJECCIÓN VERTICAL	ACERO INOXIDABLE 316L
5	2	SUJECCIÓN ANGULAR	ACERO INOXIDABLE 316L
6	10	TORNILLO DE SUJECCIÓN M5 X 0,8 CON CABEZA HEXAGONAL L=14MM - DIN 933	PIEZA ESTANDARIZADA ACERO INOXIDABLE 18-8
7	6	TUBERCA HEXAGONAL M5 X 0,8 - DIN 934	PIEZA ESTANDARIZADA ACERO INOXIDABLE 18-8

TABLA 1. LISTA DE PIEZAS DEL SISTEMA B.

NOTAS:

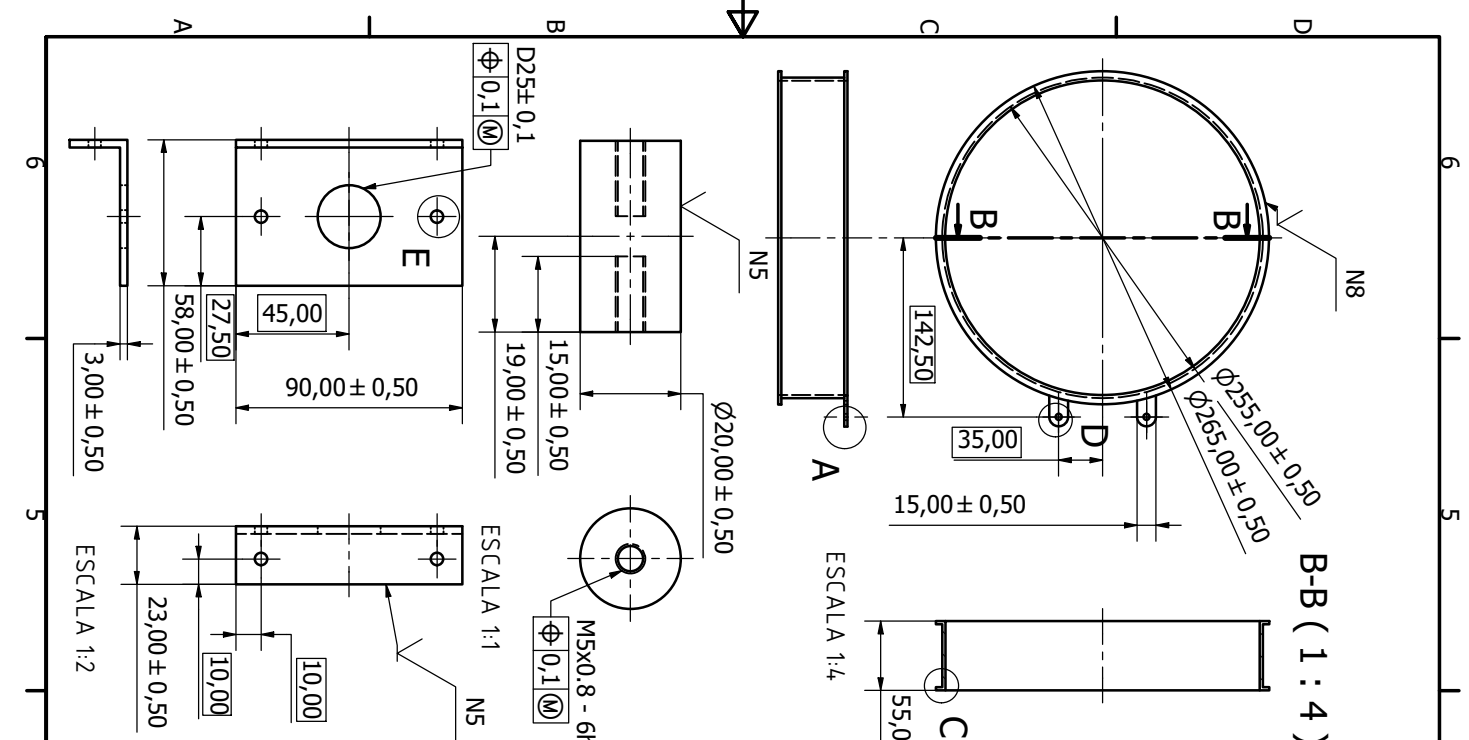
1. LAS PIEZAS 4, Y 5 DE ESTE SISTEMA SON ACOTADAS EN LOS PLANOS DEL A. SISTEMA MECÁNICO DE MIRNOV.



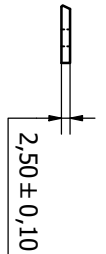
ESCALA 1:5

		AREA ACADÉMICA INGENIERÍA MECATRÓNICA REVISOR:	
NOMBRE: RMMA FECHA: 07/12/18 DIBUJ: J. MONCE VERIF: J. MORRA APROB: I. DEL VALLE FABR: ---		ACABADO GENERAL: REBARBAR Y ROOPER ARISTAS VIVAS MATERIAL: VARIOS TRATAMIENTO TÉRMICO: --- TOLERANCIAS GENERALES: XXX ± 0,50 LAS COMASE: XXX ± 0,10 BRISAAN EN MM	
CURSO: PROYECTO DE GRADUACIÓN		DISEÑO: SISTEMA MECÁNICO DE DIAMAGNETIC LOOP DISEÑO: --- BOCAL: INDICADA	
ESCALA: --- gramos		BOCAL: INDICADA	
SIN SE INDICA LO CONTRARIO:		FORMATO: A3	

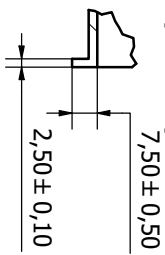
1. NÚCLEO DE LA BOBINA
DEL DIAMAGNETIC LOOP



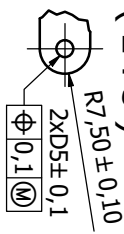
A (2 : 3)



C (2 : 3)



D (2 : 3)



ESCALA 1:6

TABLA DE REVISIÓN				
ZONA	NÚM. DE REVISIÓN	DESCRIPCIÓN	FECHA	APROBADO POR
	1			
	2			
	3			
	4			
	5			
	6			
	7			

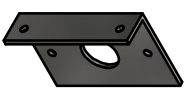
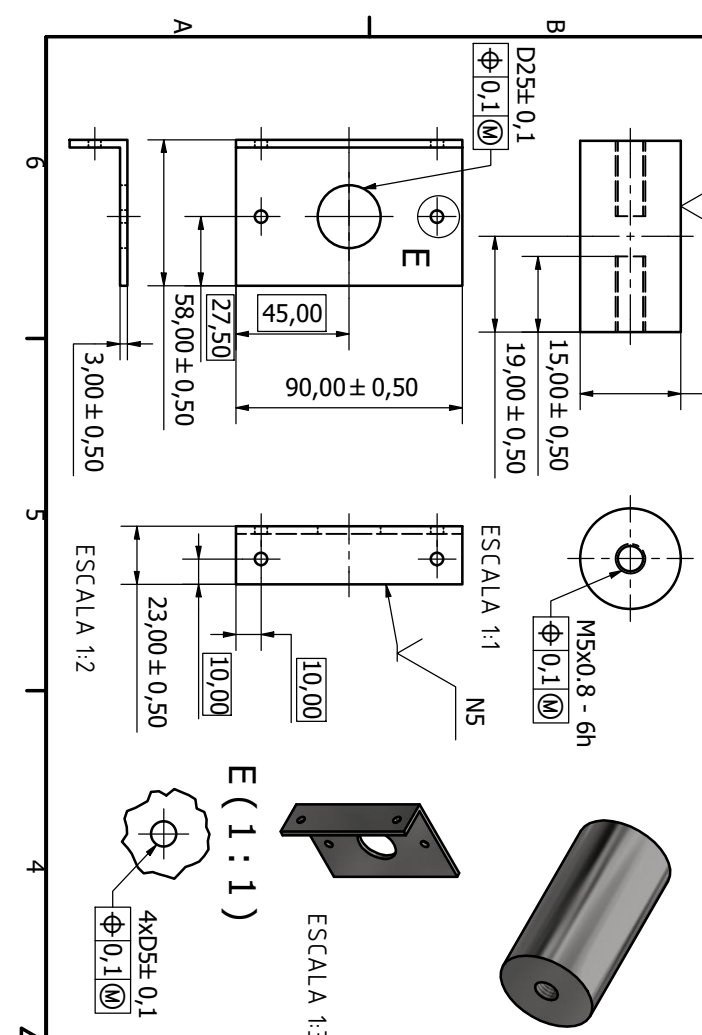
TABLA 2. TABLA DE REVISIÓN DE LAS
PIEZAS 1, 2 Y 3.

NOTAS:

1. INTERPRETACIÓN SEGÚN NORMA ISO.
2. TODAS LAS DIMENSIONES EN MM.
3. MATERIAL INDICADO EN LA TABLA 1 DEL SISTEMA.
4. FILLOS NO INDICADOS: BISEL ± 0.1.
5. TOLERANCIAS GENERALES EN CAJETÍN.
6. EL AGUJERO ROSCADO CON M5X0.8 -

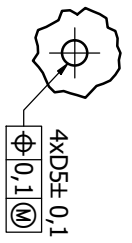
3. FIJACIÓN CILÍNDRICA ESTRUCTURAL DEL DIAMAGNETIC LOOP
2. SOPORTE ANGULAR DEL DIAMAGNETIC LOOP
6. EL AGUJERO ROSCADO CON M5X0.8 - OPUESTAS DE LA PIEZA 3.

2. SOPORTE ANGULAR DEL
DIAMAGNETIC LOOP



ESCALA 1:3

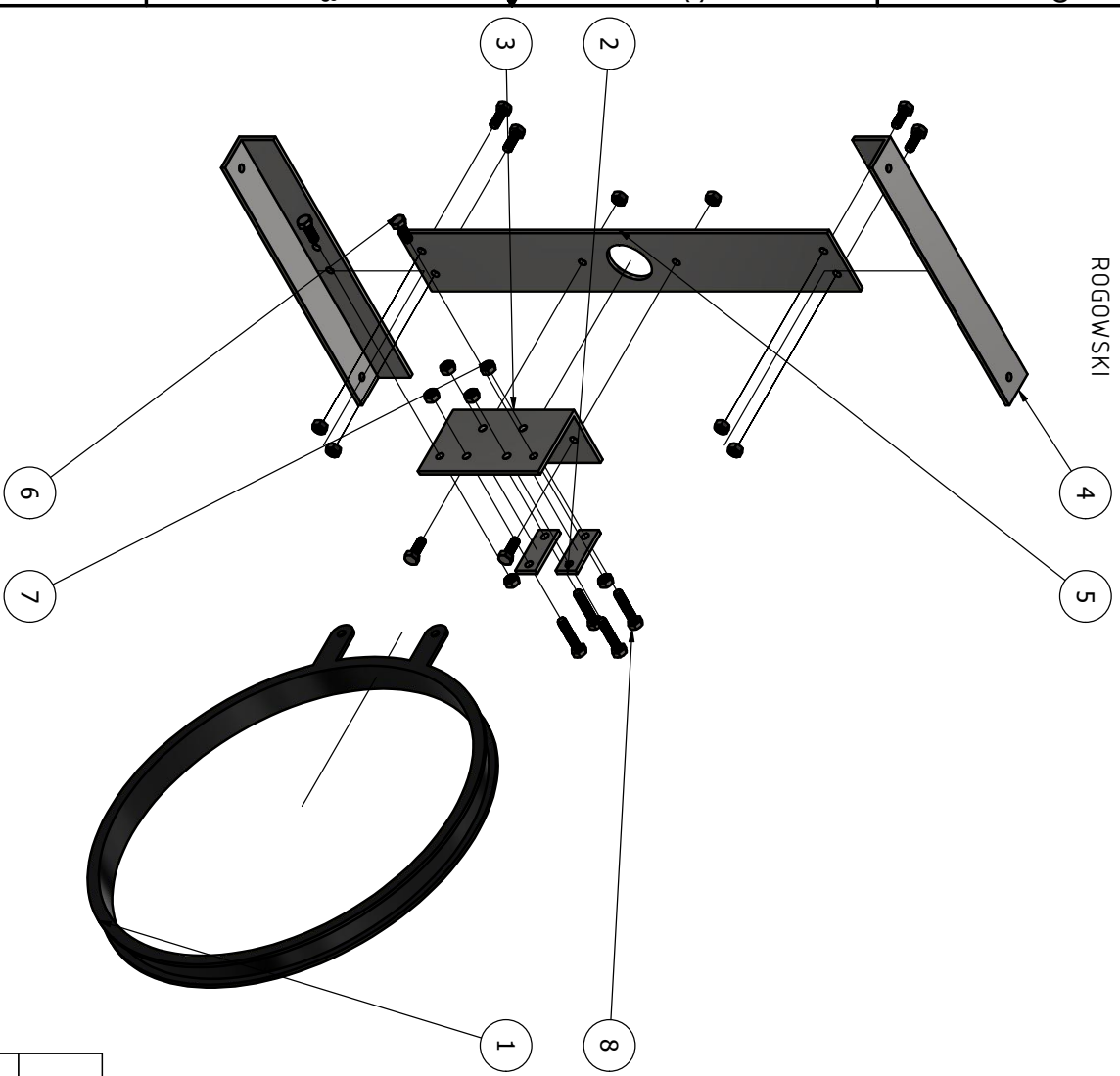
E (1 : 1)



		ÁREA ACADÉMICA INGENIERÍA MECATRÓNICA		REVISIÓN:	
		CURSO: PROYECTO DE GRADUACIÓN			
NOBRE: J. MONTE	RIMA:	FECHA: 07/12/18	ACABADO GENERAL:	DESIGNACIÓN:	
VERIF. J. MONTE		/ / 19	REBARBAR Y ROQUEAR ABRAS VIVAS	SISTEMA MECÁNICO DE DIAMAGNETIC LOOP	
APROB. I. DEL VALLE		/ / 19	MATERIA: VARIOS	DESIGNACIÓN:	FORMATO: A3
FEAB					
SI NO SE INDICA LO CONTRARIO: LAS CONFORMES EXPRESAN EN MM		TOLERANCIAS GENERALES: XXX ± 0.50 XXX ± 0.10		TRATAMIENTO TÉRMICO: ---	
		PESO: --- gramos		ESCALA: INDICADA	

C. SISTEMA MECÁNICO DE LA BOBINA DE

ROGOWSKI



ESCALA 1:3

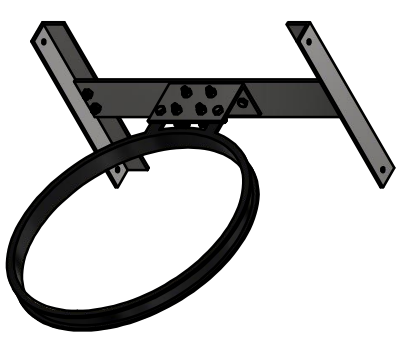
LISTA DE PARTES

ITEM	CANTIDAD	NOMBRE DE PARTE	DESCRIPCIÓN
1	1	SOPORTE PRINCIPAL DE LA BOBINA DE ROGOWSKI	GRAFIJO
2	2	FLUJACIÓN DE CABLE DE LA BOBINA DE ROGOWSKI	ACERO INOXIDABLE 316L
3	1	SOPORTE ANGULAR DE LA BOBINA DE ROGOWSKI	ACERO INOXIDABLE 316L
4	2	SUJECCIÓN ANGULAR	ACERO INOXIDABLE 316L
5	1	SUJECCIÓN VERTICAL	ACERO INOXIDABLE 316L
6	8	TORNILLO DE SUJECCIÓN M5 X 0,8 CON CABEZA HEXAGONAL L=14MM - DIN 933	PIEZA ESTANDARIZADA
7	12	TUBERCA HEXAGONAL M5 X 0,8 - DIN 934	ACERO INOXIDABLE 18-8
8	4	TORNILLO DE SUJECCIÓN M5 X 0,8 CON CABEZA HEXAGONAL L=25MM - DIN 933	PIEZA ESTANDARIZADA ACERO INOXIDABLE 18-8

TABLA 1. LISTA DE PIEZAS DEL SISTEMA C.

NOTAS:

1. LAS PIEZAS 4, Y 5 DE ESTE SISTEMA SON ACOTADAS EN LOS PLANOS DEL A. SISTEMA MECÁNICO DE MIRNOV.

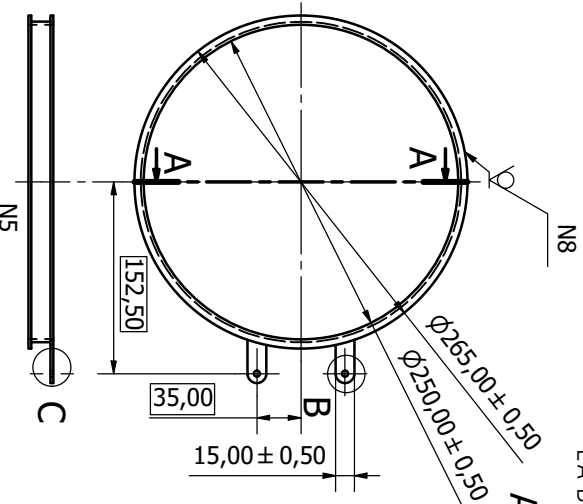


ESCALA 1:5

<p>Tecnológico de Costa Rica</p>		ÁREA ACADÉMICA INGENIERÍA MECATRÓNICA		REPÚBLICA:																					
		CURSO: PROYECTO DE GRADUACIÓN																							
<table border="1"> <tr> <td>NOMBRE:</td> <td>RMMA</td> <td>FECHA:</td> <td>07/12/18</td> </tr> <tr> <td>DEBUI:</td> <td>J. MONCE</td> <td>REVISAR Y ROQUEAR:</td> <td>ABASTAS VIVAS</td> </tr> <tr> <td>VERIF.:</td> <td>J. MOYA</td> <td>MATERIAL:</td> <td>VARIOS</td> </tr> <tr> <td>APROB.:</td> <td>L. DEL VALLE</td> <td></td> <td></td> </tr> <tr> <td>FABR.:</td> <td>---</td> <td></td> <td></td> </tr> </table>	NOMBRE:	RMMA	FECHA:	07/12/18	DEBUI:	J. MONCE	REVISAR Y ROQUEAR:	ABASTAS VIVAS	VERIF.:	J. MOYA	MATERIAL:	VARIOS	APROB.:	L. DEL VALLE			FABR.:	---			TOLERANCIAS GENERALES: XXX ± 0.50 XXX ± 0.10	TRATAMIENTO TÉRMICO: ---	DESIGNACIÓN: ---	BOCAL: INDICADA	1 DE 2
NOMBRE:	RMMA	FECHA:	07/12/18																						
DEBUI:	J. MONCE	REVISAR Y ROQUEAR:	ABASTAS VIVAS																						
VERIF.:	J. MOYA	MATERIAL:	VARIOS																						
APROB.:	L. DEL VALLE																								
FABR.:	---																								
SIN SE INDICARLO CONTRARIAMENTE: LAS COMASE DEBESAN EN MM					FORMATO A3																				

ESCALA 1:4

1. SOPORTE PRINCIPAL DE LA BOBINA DE ROGOWSKI



A-A (1:4) B (1:2)

C (1:2)

D (1:2)

ESCALA 1:6



TABLA 2. TABLA DE REVISIÓN DE LAS PIEZAS 1, 2 Y 3.

TABLA DE REVISIÓN				
ZONA	NÚM. DE REVISIÓN	DESCRIPCIÓN	FECHA	APROBADO
	1			
	2			
	3			
	4			
	5			
	6			
	7			

NOTAS:

- INTERPRETACIÓN SEGÚN NORMA ISO.
- TODAS LAS DIMENSIONES EN MM.
- MATERIAL INDICADO EN LA TABLA 1 DEL SISTEMA.
- FILDS NO INDICADOS: BISEL ± 0.1 .
- TOLERANCIAS GENERALES EN CAJETÍN.

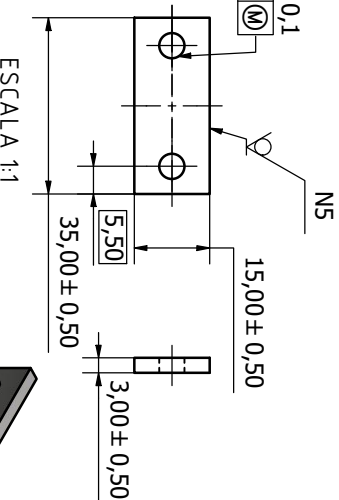
E (2:3)

ESCALA 1:3

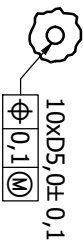
2. FIJACIÓN DE CABLE DE LA BOBINA DE ROGOWSKI



ESCALA 1:1

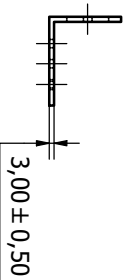


ESCALA 1:1



3. SOPORTE ANGULAR DE LA BOBINA DE ROGOWSKI

ESCALA 1:3



			AREA ACADÉMICA INGENIERÍA MECATRÓNICA REPÚBLICA	
CURSO: PROYECTO DE GRADUACIÓN			DISEÑO: SISTEMA MECÁNICO DE ROGOWSKI	
NOMBRE: J. MONSE VERDE J. MORRA APROB. I. DEL VALLE FECH. ---	FECHA: 07/12/18 MATERIAL: VARIOS	TOLERANCIAS GENERALES: XXX ± 0.50 XXX ± 0.10	TRATAMIENTO TÉRMICO: --- PESO: --- gramos	BOCAL: INDICADA 2 DE 2
SIN SE INDICARLO CONTRARIO: LAS COMAS SE ENTENDEN EN MM			FORMATO: A3	